Precise Calibrations of Few-Body Physics in Potassium-39: Experiment and Theory

by

Xin Xie

B.S., Physics, Fudan University, Shanghai 2013

M.S., Physics, University of Colorado, Boulder 2016

A thesis submitted to the

Faculty of the Graduate School of the

University of Colorado in partial fulfillment

of the requirements for the degree of

Doctor of Philosophy

Department of Physics

2020

This thesis entitled:

Precise Calibrations of Few-Body Physics in Potassium-39:
Experiment and Theory

written by

Xin Xie

has been approved for the ○ masters ◉ doctoral degree program in:

Physics

DocuSigned by:
Eric Cornell
58A5DA1820AD4F6...
5/4/2020

Eric Cornell

Committee Chair Name

DocuSigned by:
Jun Ye
FC8ACA0876154BB...
5/4/2020

Jun Ye

Committee Member Name

The final copy of this thesis has been examined by the signatories, and we find that both the content and the form meet acceptable presentation standards of scholarly work in the above mentioned discipline.

Student ID number	102616589
IRB protocol #	
IACUC protocol #	

Xie, Xin (Ph.D., Physics)

Precise Calibrations of Few-Body Physics in Potassium-39: Experiment and Theory

Thesis directed by Prof. Eric A. Cornell

Ultracold atoms provide a versatile toolbox for the study of diverse quantum phenomena. The minimal platform to present quantum mechanics is at single particle level. Two-particle interference effects such as Hanbury Brown-Twiss are a consequence of the particle statistics. Exotic quantum effects in which statistics and interactions are combined appear in three-particle systems as elucidated by e.g. Efimov in the early 1970s. Efimov's work can be further extended to four- or five-particle systems and applied to general dilute quantum gases in the weakly interacting regime. In the many-body context, it may also assist the analysis of quench dynamics in unitary gasses where perturbation theory breaks down.

A systematic study of few-body physics is made possible by the use of magnetic Feshbach resonances. One can greatly benefit from the improved experimental precision when comparing the observables to generic few-body models. In this thesis, I begin by describing the efforts we spent on achieving overall robustness and accuracy on our potassium-39 quantum gas machine, including the hardware upgrades we made for future scientific projects. Then following a brief review on the realization of Efimov physics in cold atoms, I expand on a series of scattering experiments we performed to understand few-body physics with effectively repulsive inter-particle interactions, as a complement to our previous investigations of the attractive-interaction regime. At the end, I combine our knowledge from both regimes together to discuss the global picture of Efimov physics in homonuclear systems at a beyond proof-of-principle level.

Dedication

" Blind to all fault, destiny can be ruthless at one's slightest distraction. "

— Jorge Luis Borges, *Ficciones*

To my family, for your unconditional support.

To my friends, for your company and tolerance.

To healthcare workers, for protecting my loved ones.

Acknowledgements

There are many people I would like to express my gratitude to in this thesis. My late advisor Deborah Jin taught me various expertise in the lab. As time passed by those knowledge inevitably started to fade out. What lingers in my memory about her is the short walk that we took together along the cliff when we were at a conference at Rhode Island. I could see the Atlantic Ocean, and smell the seaweed. Everything is still vivid when I close my eyes.

My other advisor Eric Cornell has been the most important person throughout my graduate school study. His infinite patience and playful personality make him the greatest teacher and friend. Eric is the smartest, most considerate and financially supportive advisor. The statistical probability is extremely low to find all these amazing qualities in a single person who needs also be good with one-handed softball and Mandarin Chinese.

Since 2016, Eric and Jun Ye have been co-advising our project on potassium-39. Jun introduces to us his hard-core, single-minded, second-to-none instrumentation techniques. He influenced me with his strong attitude toward numerous things such as error bars and theoretical models. When facing technical difficulties, Jun is usually the only one who keeps the faith even everyone else loses it. And this is because he has programmed himself to do so.

I cannot finish my thesis without the help from JILA personnel. I began my first machining project under the training of Kim Hagen. I am grateful for all the crafty and friendly instrument shop staff especially Todd Asnicar, Hans Green, and James Urich. Research can be frustrating, but machining is always full of fun. I would like to say thank you to the electronic staff Terry Brown, James Fung-A-Fat, and Carl Sauer. Thank all of you for chatting with me and sharing

your magic tricks. Time really flies when the solder iron is in hand (and Jan Hall takes the next seat at the counter). I appreciate all the computer rescue provided by J. R. Raith, Corey Keasling and Jim McKown, who have been frequently dragged down to the lab after hours. I appreciate the administrative work done by Krista Beck, Amy Allison, Cynthia Torres and Agnieszka Lynch. Your warmhearted assistance is essential to me accomplishing my degree. I would also like to thank Brian Lynch for tracking my purchases, and Jason Ketcherside for building maintenance. Your help is super important and allows me to focus on my research.

My labmates are those who I spent the longest time with in the past seven years. I have gained endless power from their encouragement. Cathy Klauss is the senior graduate student who introduced me to many fundamental skill sets in AMO experiment. We spent tremendous efforts on repairing our old rubidium-85 machine. And eventually we were able to make the biggest rubidium-85 BEC worldwide and studied strongly interacting dynamics with it. Cathy is gifted with stunning presentation and writing skills. I later work with graduate students Roman Chapurin and Michael Van de Graaff (a.k.a. Vandy) on the potassium-39 experiment. We converted this new generation fermi gas machine into a bose gas machine in 2016-2017. Roman is highly motivated and productive. We went through the optimization of every single step in the whole cooling process of potassium. This became the most valuable experience for my independent research later on. Vandy and I took lots of data on the scattering experiment for repulsive inter-particle interactions. Vandy is a master of optics. He is meticulous about details and full of creativity. I believe he will discover a lot of interesting physics in the days to come. I miss the time I spent with graduate students Philip Makotyn, Rabin Paudel, Noah Schlossberger, undergraduate students David Goldberger, Carlos Lopez-Abadia, Joshua Giles, Jared Popowski, Bjorn Sumner. It was the most peaceful memory that one day in the afternoon everyone in the lab was so immersed in the work on their hands. Hours of time elapsed in this quietness before anyone realized it. In addition, I will always remember the relaxing and informative conversations with the folks from the EDM, KRb, strontium, cavity, tweezer, cold molecule, and membrane labs.

I am often impressed by how startlingly well theory and experiment agree with each other in

the field of cold atom scattering and interactions. I feel really fortunate to be acquainted with a number of brilliant theorists in the past years. Paul Julienne (a.k.a. "the wizard") has repeatedly amazed me with his encyclopedic knowledge on the scattering properties of any atomic species. He explains physics in the most precise language and always points to the right literature for me in the blink of an eye. José D'Incao is our expert on three-body physics. His numerical models are the most powerful theoretical toolbox that we have. Besides, I appreciate all the enlightening discussions I had with John Bohn, Doerte Blume, Bo Gao, and many others who I exchanged e-mails with but have not had a chance to meet in person.

Lastly, I would like to thank my parents for always encouraging me to pursue my dreams. With your guidance, I am able to enjoy my hobbies and choose the career that I love. I would also like to thank Sudi Chen and Ruqi Yi, for helping me develop confidence as well as an independent personality, and for being there for me on the rainy days.

Contents

Chapter

Tables

Table

Figures

Figure

Chapter 1

Introduction

1.1 What is Universality and Why is it Important?

The concept of *universality* has been broadly discussed in the context of *critical phenomena* in condensed matter. Physics systems with completely different properties at the atomic level obey universal power-law thermodynamics when they undergo *phase transitions* such as liquid/gas transition, paramagnetic/ferromagnetic transition and so on so forth. In the critical regions which can be defined by the correlation length l much longer than the intrinsic length scale r_0, different systems can be divided into a small number of classes based on the same *critical exponent* of the power laws [1]. Deeply rooted in these universal phenomena is the so-called *renormalization group* (RG) theory by Kenneth Wilson [2]. By integrating out the ultraviolet degrees of freedom (or performing a renormalization group transformation) in the space of coupling constants, people obtain the quantity called *RG flow* which leads in the infrared limit to interesting scaling-invariant physics described only by long-distance degrees of freedom such as temperature and pressure. The above mentioned *continuous scaling invariance* in phase transitions represents the simplest topology of the RG flow that is termed a *fixed point*. The next complicated structure is a *limit cycle* which heralds *discrete scaling invariant* behaviors at the macroscopic level.

Universal physics in neutral atoms with large scattering length can be derived in the same framework yet exhibit richer meanings of multiple layers. This is explained from a general dimensional argument in this Introduction section and illustrated with more microscopic details in Ch. 3.

Neutral atoms interact with each other through van der Waals (vdW) force at long distance whose range is usually parametrized by r_{vdW}. When atoms stay in their electronic ground state, r_{vdW} is only s few nanometers. In the low-collision-energy limit, the characteristic length scale of scattering processes is the s-wave scattering length a. Intuitively this is because the scattering wavefunction is so delocalized at low temperatures that the majority of it lies outside the interaction potential thus simply follows a free-particle-like sinusoid. The tiny fraction of the wavefunction that overlaps with the interaction potential effectively sets the short-range phase of the sinusoid which turns into an offset from the origin in the center-of-mass frame. This offset is the so-called scattering length a. When looking from long distances, the two particles are repulsive when there is a positive offset and attractive when there is a negative offset regardless of the sign of the underlying interaction potential [3]. Sometimes the scattering length a can acquire a much larger absolute value compared to r_{vdW} either due to some fine tuning of interaction potential or the use of a *Feshbach resonance*. It then becomes the only relevant length scale that people need to understand the scattering- and bound-state observables in two-body problems. For instance, the binding energy E_b of *Feshbach molecules* depends only on a in the large a limit: $E_b = \hbar^2/ma^2$. This is the first layer of universality that may be called the "scattering-length universality" [4]. Low-energy two-body observables display continuous scaling invariance under the transformation on scattering length a, the coordinate $\mathbf{r}$, and the time t by a positive number ζ

$$a \longrightarrow \zeta a, \qquad \mathbf{r} \longrightarrow \zeta \mathbf{r}, \qquad t \longrightarrow \zeta^{-2} t. \tag{1.1}$$

Violations of this universality are suppressed by powers of $r_{\mathrm{vdW}}/|a|$. In this regime, a also determines some macroscopic properties in mean-field problems for a collection of particles.

If we crank up the scattering length with the help of a Feshbach resonance, eventually we can reach the limit of $|a_0| \to \infty$ which is called the *unitary limit*; for two particles colliding with momenta $\pm\hbar\mathbf{k}$ in the center-of-mass frame, the s-wave contribution to the scattering cross section saturates to $\sigma_{(a\to\pm\infty)} = 4\pi/k^2$ (the phase shift $\delta_{l=0}(k)$ modulo π approaches $\pi/2$), which is the largest it can be consistent with the constraint that the scattering S-matrix is unitary as a result

of conservation of probability. The relevant length scale in this case is played by $1/k$ which can be related to the de Broglie wavelength λ for bulk gases. This can be understood by the fact that the interaction between neutral atoms is short-range in nature no matter how large a is — it can only take place when the interacting entities are in contact with each other. $|a_0| \to \infty$ is also called the *resonant limit* and it has been a breeding ground for new physics. A well-known example is that different strongly interacting spin-$\frac{1}{2}$ fermions share a universal expression for the chemical potential μ that is purely set by the number density n

$$\mu = \xi \frac{\hbar^2}{2m}(6\pi^2 n)^{2/3}, \tag{1.2}$$

where ξ is the *Bertsch parameter* that has been determined both theoretically and experimentally [5]. Similarly, in the two-body sector of strongly interacting degenerate bosons or *Bose-Einstein condensates* (BECs), the divergent λ gets replaced by the inter-particle spacing d which scales as $n^{-1/3}$ and sets the energy and time scales for the development of quantum dynamics [6, 7, 8].

The third layer of unversality is unique to the three-body sector and only applies to bosons and heteronuclear fermions in the absence of Pauli blocking effect. In addition to the aforementioned two-body length scales, low-energy observables may also have dependence on another scale which is sometimes named the *three-body parameter* (3BP). Vitaly Efimov first discovered that in the resonant limit there are an infinite number of arbitrarily-shallow three-body bound states (named trimers) subject to a binding energy spectrum of the form

$$E_T^{(n)} \longrightarrow (e^{-2\pi/s_0})^{n-n_0} \frac{\hbar^2 \kappa_0^2}{m} \qquad (n, n_0 \in \mathbb{Z}), \tag{1.3}$$

where $s_0 = 1.00624$ for three identical bosons [9]. In this expression, a wave number κ_0 acts as the 3BP and fixes the absolute locations of the trimer states. This spectrum displays discrete scaling invariance under the transformation

$$\kappa_0 \longrightarrow \kappa_0, \qquad \mathbf{r} \longrightarrow \zeta_0^n \mathbf{r}, \qquad t \longrightarrow \zeta_0^{-2n} t, \tag{1.4}$$

where $\zeta_0 = e^{\pi/s_0}$. Efimov trimers are peculiar in that their spatial extents can be infinitely large as $n \to +\infty$. Stepping away from the resonant limit, the above symmetry also holds at finite a under

the discrete transformation

$$\kappa_0 \longrightarrow \kappa_0, \qquad a \longrightarrow \zeta_0^n a, \qquad \mathbf{r} \longrightarrow \zeta_0^n \mathbf{r}, \qquad t \longrightarrow \zeta_0^{-2n} t. \tag{1.5}$$

This result gives rise to the famous Efimov's three-body bound state spectrum in two-dimension space as functions of $E^{1/2}$ and $1/a$, which is regarded as a remarkable example of self-similarity. The original derivation of Efimov's spectrum is based on a zero-range (δ function) two-body interaction potential, which is approximately satisfied in real atomic systems at finite a when $|a| \gg r_0$. This approach brings up another powerful concept of the *zero-range limit* which has been frequently used in analytic methods by introducing 3BP as a boundary condition at $\mathbf{r} \to 0$.

Last but not least, the recent discovery of a modern unversality has really brought the study of few-body physics with ultacold atoms into focus. This is the well-known *van der Waals universality*. As discussed above, people use zero-range theory to predict the geometry and scaling of trimer spectrum, then fix the absolute values of three-body observables with the help of a three-body parameter (3BP). The necessity of introducing a 3BP has to do with a shortcoming of the two-body zero-range potential, namely that it leads to an effective three-body potential that can support an infinite number of trimer states with infinitely small size and infinitely high energy (as $n \to -\infty$). This unbounded-from-below spectrum is referred to as *Thomas collapse* or *fall of the particles to the center* [10]. One would expect this behavior to break down below a distance comparable with the range of real potentials such as r_{vdW}. The function of 3BP is to encapsulate the effect of two-body and possibly three-body interactions at short distances hence pins down the true ground trimer state. It can take the form of a wave number, a length, an energy or a phase depending on the formalism used. Strictly speaking, only in the large n limit does it represent the true 3BP since the universal scaling factor only approximately holds for the low-lying trimer states in real systems. Given that to access the excited states with $n \geq 1$ in practice requires extremely low temperature, trimer branches with $n = 0, 1$ have been serving as the 3BP as compromise. A convenient quantity frequently measured is where the ground trimer state intersects the free-atom threshold in the $a < 0$ region, denoted as $a_-^{(n=0)}$. In the early days this empirical 3BP

was not anticipated to be known *a priori* due to its sensitivity to the detailed form of the short-range forces [11]. As people collected extensive experimental evidences on various atomic species, they discovered a universal position of $a_{-}^{(n=0)}$ which is roughly ten times r_{vdW} [12]. This rather unexpected result has later been traced back to an origin related to the $1/r^6$ form of the van der Waals potential between two neutral atoms [13, 14, 15, 16]. This original version of van der Waals universality assumes a virtually pure spin configuration during the collision processes (sometimes termed *single-channel model*) and applies to the broadest Feshbach resonances in species like ^{133}Cs. It has later on been generalized to two-, three- and even more scattering channels to emulate more complicated spin configurations [17, 18]. Notably the remarkable predicting power of this multi-channel van der Waals theory suggests that additive pair-wise interaction (specifically van der Waals) plays the dominant role in the three-body problem while short-range forces that explicitly involve three particles at the same time (e.g. Axilrod-Teller) are somehow always negligible [19].

Much of contents in this thesis is along the line of this last kind of universality to explore the "imperfections" of the 3BPs associated with the low-lying trimer branches.

1.2 Thesis Contents

There are two major technical challenges in the cooling processes of ^{39}K. One is the small hyperfine splitting energy of the electronic excited state $^2\mathrm{P}_{3/2}$ on D_2 transition that is normally exploited for laser cooling alkali metals [20, 21]. Such small energy level splittings are comparable to the natural linewidth of the excited states therefore spoil closed optical transitions. The second challenge is the small elastic scattering cross section between atoms at hundreds of microKelvin and zero magnetic field due to the presence of a *Ramsauer-Townsend minimum* [22, 23]. This suppresses the efficiency of evaporative cooling thus necessitates the use of an all-optical trapping scheme combined with a magnetic-field-tunable scattering length.

In Chapter 2, I first introduce the apparatus that we use to perform all few-body physics experiments. In order to repeatedly produce ^{39}K gas samples in a well-controlled quantum state including temperature, number density, and spin state, we start off with a laser cooling stage that

consists of Magneto-Optical Trap (MOT) collection, compressed-MOT, and sub-Doppler cooling with Λ-enhanced gray molasses. We then move on to evaporative cooling in a crossed-dipole trap with well-calibrated trapping frequencies. I describe an interferometric method we use to track the spectral linewidths e.g. of the laser that probes the atoms. Another thing to focus on is how we understand our absorption imaging process to obtain trustworthy number and spatial distribution measurements of the atoms. I also describe how we achieve stable magnetic-field control as well as its robustness against strong rf radiation. Next I detail the efforts we made to upgrade the hardware of our ^{39}K machine for future envisioned experiments. This includes the implementation of a high resolution imaging setup of numerical aperture about 0.4 and a fast magnetic-field control system that can be used to initiate quench dynamics on a BEC .

In Chapter 3, I begin with briefly introducing major previous experimental and theoretical results on Efimov physics to illustrate the evolution of understanding in this field. As to the global picture of Efimov's spectrum as a function of the coupling strength, I refer to a two-channel field theory [15, 24] which qualitatively predicts some interesting trends. When it comes to the absolute values of three-body observables, I emphasize the quantitative contributions from a numerical approach done in *hyperspherical coordinate* [25]. I then discuss the missing pieces of the puzzle and what makes ^{39}K a promising candidate in filling in the unexplored territory.

In Chapter 4 and 5, I expand on the main body of our few-body physics project. We measured a series of two- and three-body observables including the lifetime of Feshbach molecules, *d*-wave resonance at 63 G, atom-dimer reaction rate, dimer-dimer reaction rate, molecule-to-molecule transition by microwave coupling, and three-atom recombination rate. The study of each observable is divided into the following aspects: design of experimental sequence, data analysis, systematic analysis of experimental uncertainties, theoretical model or numerical simulation. In this thesis, I focus on the repulsive interaction region with the *s*-wave scattering length $a > 0$. This is a regime that people frequently encounter in all kinds of cold-atom experiments that involve collisions. Nevertheless the seemingly straightforward dynamics can sometimes lead to difficult-to-interpret results if certain details of the experiment are not properly handled.

In Chapter 6, I conclude the work presented in this thesis by discussing the connections between different three-body observables. In the end I briefly cover ongoing projects and future directions.

Chapter 2

Apparatus

2.1 Apparatus in Few-Body Physics Project

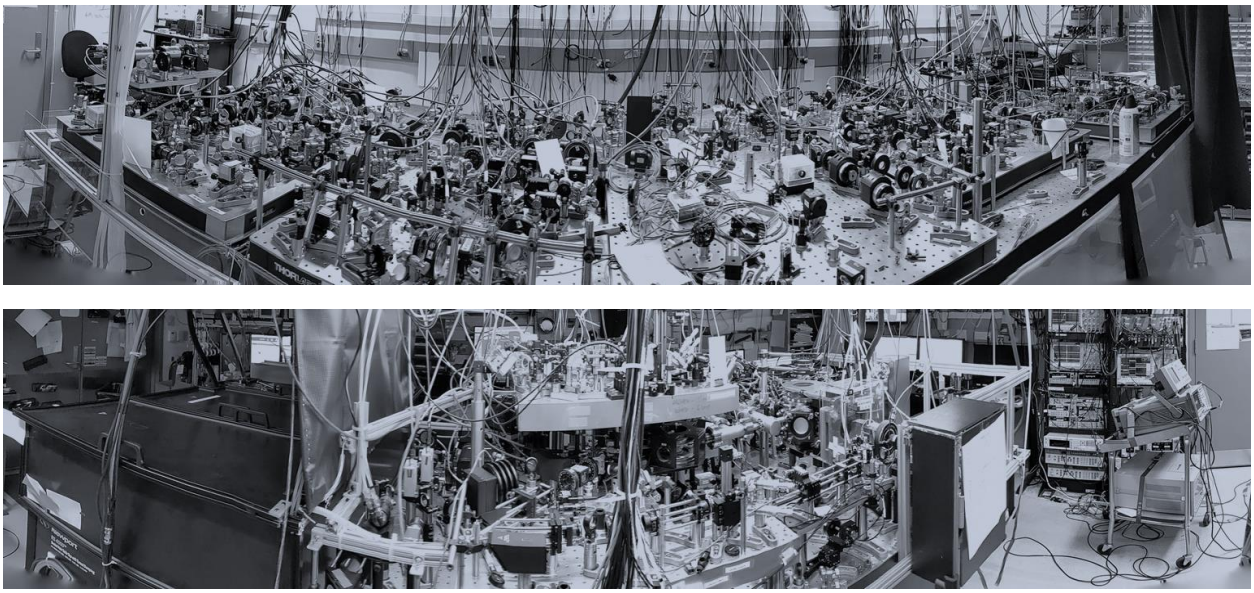

Figure 2.1: Photographs of the laboratory as of early 2020. Top panel: the laser table; bottom panel: the science table. Our lab is located in X1B30 in the basement of JILA X-wing. The lab temperature is stabilized at $20 \pm 0.5\,^{\circ}\mathrm{C}$. The lab humidity is controlled at $37 \pm 3\,\%$.

Although I was not involved in the basic infrastructure of the ^{40}K experiment dating back to around 2012, I participated in the entire second half of the construction process ca. 2016, with the goal of modifying it into a bose gas machine with large atom number and relatively fast repetition rate. Properties of ^{39}K and overviews of our quantum gas machine can also be found in Rabin

Paudel's and Roman Chapurin's these [26, 27] as complementary materials to this thesis.

2.1.1 Laser Cooling

Our experiment consists of three vacuum chambers (see the left panel in Fig. 2.2 for a top view of the whole setup), two for 3D-MOTs and one smaller glass cell for doing science. The first MOT acts as a source MOT where we collect and pre-cool the atoms from ambient gas. It is a Pyrex cell with 9 windows and six dispensers with potassium and rubidium sources in them (see Fig. 4.1 in [26] for a picture of the bare cell). It typically takes less than 15 minutes for the dispensers to saturate ^{39}K vapor on a daily-operation basis. The temperature of MOT1 is constantly maintained at around 65°C to prevent the vapor from depositing on the walls. To enhance the MOT1 loading rate (which is found to affect the MOT2 loading rate), we achieved our best performance at the maximal possible gradient of MOT1 at around 10 G/cm. The MOT1 cell has been equipped with three UVA LEDs for the purpose of light-induced atom absorption (LIAD), whose efficiency turns out to degrade over several months' time. So in practice we are not using this approach any more. The $1/e$ loading time constant of MOT1 is 1-2 seconds. The lifetime of the atoms in MOT1 is on the same scale.

The atoms are continuously pushed from the first MOT to the second MOT by a laser beam during the MOT load stage. The push efficiency appears to be the limiting factor in MOT2 loading rate whose $1/e$ time constant is about 10 seconds. The linearly-polarized push beam is picked up from the zeroth-order of an AOM in the repumper beam path on D_2 transition, and carefully focused down to its 1 mm waist offset to the side of MOT2 cloud to avoid blasting the atoms in MOT2 away. As the atoms travel from MOT1 to MOT2, they are further guided and supported against the gravity by a permanent hexapole magnetic field transverse to the transfer tube. The 5.5 mm inner radius and 47 cm length of the transfer tube require a sensitive alignment of the push beam. We pulse on the push beam repeatedly when walking the mirrors and optimize the fluorescence signal from the MOT2 cloud on the fly.

MOT2 is a stainless steel chamber with 7 viewports. Its quadrupole field is provided by the

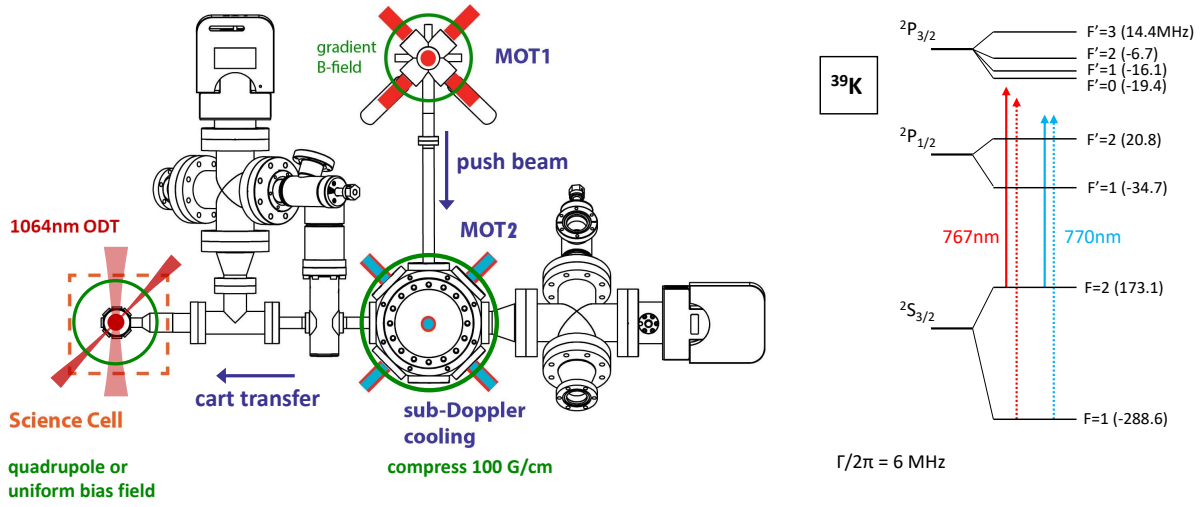

Figure 2.2: The vacuum system and optical transitions of ^{39}K. Left panel: top view of the vacuum system and the functions of individual components. Right panel: optical transitions of the D_1-line (red) and D_2-line (cyan) of ^{39}K.

water-cooled coils mounted on a moving cart. These coils confine the atoms as they are transferred from MOT2 to the science cell. We purposely use low quadrupole gradient 6 G/cm (in the strong-confinement direction) to increase the MOT2 capacity at the price of slow filling rate. We employ both D_2- and D_1 transitions to perform Doppler cooling and sub-Doppler cooling stages in MOT2. The timeline for the entire laser cooling sequence is summarized in Fig. 2.3. Information on the layouts of MOT lasers, part numbers of the optics and frequency stabilization systems can be found in [27]. MOT2 collection (or Doppler cooling process) is optimized iteratively since the push beam detuning, the magnetic field gradient, and MOT D_2 laser detunings are all more or less coupled. We have the conventional three orthogonal retro-reflecting beam configuration. We suspect that the retro-reflecting beams may limit the MOT number due to the dark shadows created by the dense cloud on the retro-reflected beams. We operate the MOT D_2 lasers at high I/I_{sat} to have sufficient optical pumping while being able to stay far-red-detuned at the same time. The MOT2 cloud is relatively hot and puffy due to the strong re-absorption of photons. We implement a short end-MOT stage (equivalent to D_2 compressed-MOT) by further red-detuning the laser frequencies in order to reduce the cloud size for the purpose of fluorescence imaging. It is not completely trivial to calculate atom number directly from the measured fluorescence intensity due to the complicated energy levels (a detailed six-level analysis on ^{40}K MOT can be found in [26]). Therefore, the MOT2 numbers quoted in this thesis are estimated based on the transfer efficiencies between successive stages plus the final atom number measured in science quadrupole trap using the more reliable absorption imaging method.

To further lower the temperature of the cloud, we borrowed the idea of an unconventional D_2 and D_1 combined compressed-MOT from [28, 29]. D_2 repump beam and D_1 trap beam work together to cool down the atoms to about 200 μK with a number transfer efficiency of 80 % from the MOT. We then load the atoms to the Λ-enhanced gray molasses stage [30, 28, 31] with an efficiency of over 90 %. This cooling scheme employs the D_1 transitions $|F = 2\rangle \rightarrow |F' = 2\rangle$ ("trap" laser) and phase-coherent $|F = 1\rangle \rightarrow |F' = 2\rangle$ ("repump" laser) to form a Λ-type configuration (see Fig. 2.4 (a)). At the two-photon resonance condition $\delta = 0$, a velocity-selective dark state can be

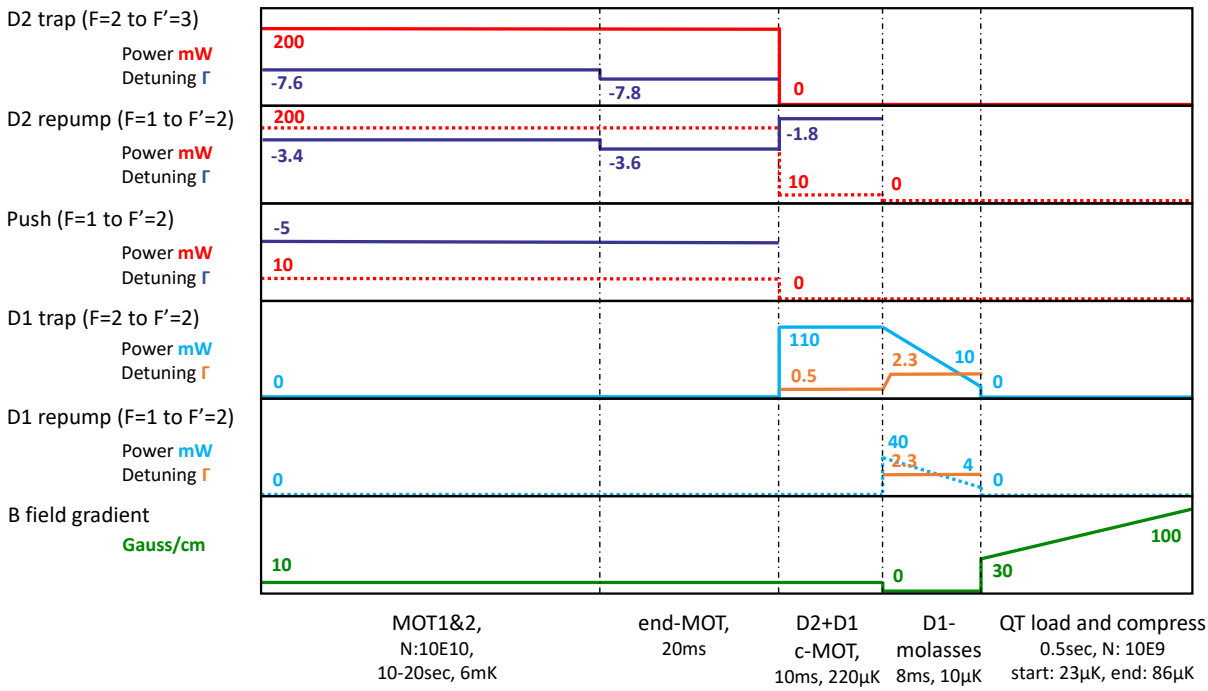

Figure 2.3: Typical timeline of laser cooling for ^{39}K. MOT laser powers, detunings and magnetic field gradient are shown for each stage. Note that the time intervals for different stages are not true to scale, and the numbers can vary a bit every time we re-optimize the sequence. The $1/e^2$ beam waist of MOT1 lasers is about 1.4 cm, the $1/e^2$ beam waist of MOT2 lasers is about 1.4 cm. The push beam waist is about 1 mm.

created (sometimes called velocity-selective coherent population trapping (VSCPT) in literature). Benefiting from the narrow spectral width of this dark state, a temperature much lower than with the regular polarization-gradient cooling (PGC) can be achieved. We ramp down the powers of both lasers to 1/10 of the initial value over 8 ms to gradually reduce the capture velocity. We are able to constantly reach below 10 μK at the end of the gray molasses. The duration of molasses is kept as short as possible to minimize the diffusion of the cloud. Our trap laser is locked to ^{39}K saturated-absorption spectroscopy via a modified Pound-Drever-Hall (PDH) lock [27]. We use a double-pass AOM to bridge the frequency gap and also to adjust the global detuning Δ. The repump laser is locked to the trap laser via a heterodyne beat note lock (see Fig. 2.4 (b)(c) for its spectrum). The two lasers are combined on a 70:30 non-polarizing beam splitter to inject a 1W Tapered-Amplifier (TA). A home-built optical cavity is used to monitor the power ratio of the two tones. Note that as the Distributed Bragg Reflector (DBR) lasers age over a few years' time, the contrast of phase lock peak will slowly decay. However, this does not impact the overall performance of our laser cooling process because even without the Λ-enhanced cooling power we still have low enough temperature in molasses to load the atoms into the quadrupole trap.

Following the laser cooling sequence, we suddenly turn on (in less than 0.5 ms) the quadrupole trap (QT) at about 30 G/cm in the strong-confinement direction. About 1/3 of the atoms, those in the low-field-seeking spin state $|\mathrm{F} = 1, m_\mathrm{F} = -1\rangle$, are loaded into the QT. In principle, doing optical pumping (OP) prior to the QT load could greatly improve this efficiency. However due to the high density of our cloud, we could not perform an efficient OP without significantly heating up the cloud. Following the QT load, we adiabatically ramp up the cart magnetic field gradient to 100 G/cm in 100 ms. This step is to reduce the size of the cloud as initially loaded from the molasses so that it can travel through the half-meter-long transfer tube that is only 1.5 cm in inner diameter. About 90 % of the atoms can successfully arrive at the science cell in 3.5 seconds with a position accuracy of a few microns. We then ramp down (up) the cart (science) QT simultaneously to prepare for optical trap load. The science QT is further ramped up to 193 G/cm as the cart moves away from the science cell back to its MOT2 position. We consistently have 3×10^8 atoms

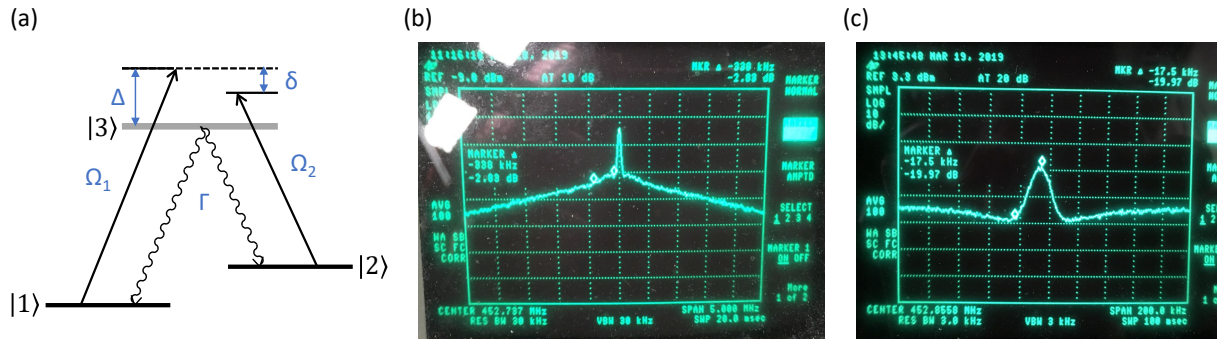

Figure 2.4: Λ-type configuration for gray molasses and phase lock signal. (a) The three-level Λ-type configuration for gray molasses cooling. A strong standing wave with Rabi frequency Ω_2 and a weaker standing wave with Rabi frequency Ω_1 illuminate the atoms at the same time. The global detuning Δ is blue-detuned from the D_1 transition. The single-photon transition linewidth $\Gamma = 6\,\mathrm{MHz}$. The narrower two-photon transition linewidth leads to enhanced cooling efficiency that lies within $0.5\,\Gamma$ near the Raman detuning $\delta \approx 0$ (see Fig. 2.26 in [27]). (b) The beat note signal measured with a photo detector is monitored on a spectrum analyzer. The 3dB point represents approximately twice the laser linewidth which reads 300 kHz in this case. (c) Zoom in on the phase lock peak whose contrast is on the order of 20dB. The span of the phase lock peak between the markers is about 17 kHz which is limited by the jittering of the VCO box.

at 180 μK in science QT.

Our science cell is a fused-silica octagon with seven 0.625" windows on the side and two 1.7" windows on top and bottom (see Fig. 4.3 in [26] for a picture of the bare cell). Characterizations of the transmissions can be found in [26] and [32]. We stock additional sample windows for the purpose of off-line test on our imaging systems.

2.1.2 Evaporative Cooling

Unlike species such as ^{87}Rb, it is difficult to directly evaporate ^{39}K in a quadrupole trap due to its small elastic collision rate at low magnetic field. One solution is to perform sympathetic cooling with species like ^{41}K or ^{87}Rb [33, 34]. In order to reduce the number of lasers used in the experiment thus improve its overall stability and reliability, we decided to take the advantage of high-power infrared fiber amplifier technique and do evaporation in a optical dipole trap (ODT). An ODT helps us tightly confine the atoms and allow for a uniform DC magnetic field that can be used to adjust the elastic scattering cross-section of the atoms freely. We use a 500mW CW 1064 nm single-frequency Nd:YAG laser (Coherent, Mephisto 500NE) to seed a 50W fiber amplifier (Coherent, NUA-1064-PC-0050-D0) with a customized output beam size of 1 mm. A 25W $28 \times 28\,\mu$m waist ODT beam (named "H1 beam") is shone onto the atoms for 8 seconds as they are being held in science QT. The trap depth is calculated to be 2.7 mK. An H-bridge consisting of four mechanical relays switches the polarity of one of the QT coils to switch from the original anti-Helmholtz configuration into Helmholtz configuration during the ODT load. Within the 200 ms switching time, a shim field that is perpendicular to the bias field is temporarily turned on to maintain the quantization axis for the spin-polarized gas. Omitting this crucial step will lead to spin impurities. The timeline of QT/ODT load sequence is summarized in Fig. 2.5. Working with a high power laser comes with challenges involving long-term mechanical and thermal stability from month to month (see [27] for part numbers of the optics, detailed layouts and how we handled numerous technical issues). Due to the relatively low atomic density of $10^{10}\,\mathrm{cm}^{-3}$ and small collision rate about 1.3 Hz in the QT, we end up with 6×10^6 (up to 1×10^7) atoms at $300 - 400\,\mu$K being transferred to ODT. To improve

this loading efficiency, one idea might be to recycle the H1 beam to form a crossed-ODT [34] in order to gain in the trap depth; another idea could be to borrow the idea of in-trap (sub-)Doppler cooling from the optical-lattice- or optical-tweezer-based experiments [35, 36, 37]).

We ramp down the power of H1 beam over about 3 seconds time for the stage-1 evaporation. Meanwhile the atoms are gradually caught by our science crossed-ODT (x-ODT). The science x-ODT is up to 10 μK deep and formed by a sheet beam ("H2") along the horizontal direction (roughly 45° to the H1 beam) plus a cylindrical beam ("V") along the vertical direction. The trap center of x-ODT lies spatially below the H1 trap center due to the different gravity sags. The stage-2 evaporation is done in this weakly-confined x-ODT for the purpose of generating low density clouds in the end. Five orders of magnitude increase in the phase space density (PSD) can be achieved with this two-stage evaporation scheme. The temperature of the cloud is mainly set by the trap depth of H2 beam, – fast atoms are leaked out primarily from the bottom of the sheet trap under gravity; the density of the cloud can be adjusted by changing the power on the V beam which provides confinement along two horizontal directions. The evaporation steps inside the magenta box of Fig. 2.5 are empirically fine-tuned to prepare the samples at desired initial temperature and atom number. In equilibrium condition, the temperature, $k_{\mathrm{B}}T$ of our cloud is found to be about 1/8 of the calculated values of the trap depth. Upon finishing the evaporation, we adiabatially ramp up the trap depth to be about 10 times the final temperature of the cloud in order to prepare redundancies for any heating effects when measuring the lifetimes of the atoms. Omitting this step will lead to extra number loss due to ongoing evaporation.

2.1.3 Crossed-Dipole Trap Calibrations

Huge amount of effort is spent on suppressing the mechanical, thermal, electronic noise on the ODT system. Fig. 2.6 presents a systematic characterization of the lifetime and heating rate for different initial conditions. We are able to achieve very low heating rate on the order of nK/s. The background lifetime (50 - 100 seconds) of the atoms is limited by the vacuum quality rather than the off-resonance scattering from the ODT photons.

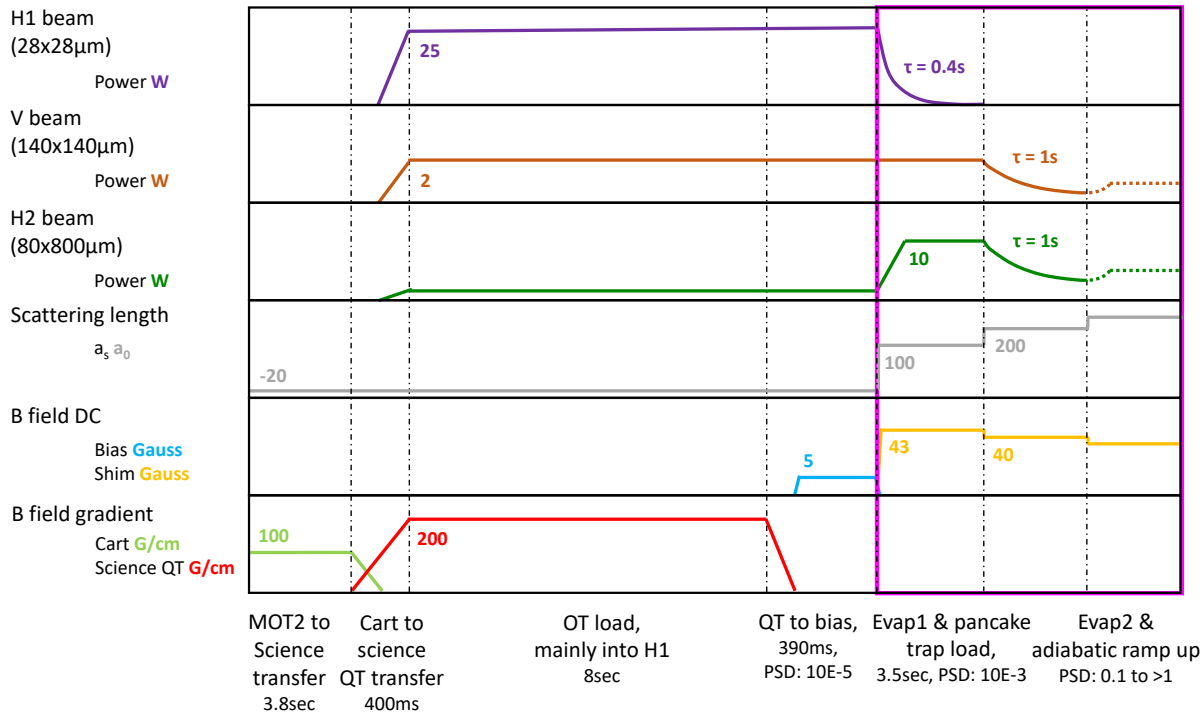

Figure 2.5: Typical timeline of transferring the atoms from cart quadruple trap (QT) into science QT, optical dipole trap (ODT) load and evaporative cooling. Shim field is orthogonal to bias field and provides a transient quantization field when bias coils switch from anti-Helmholtz to Helmholtz configuration. Note that the steps inside magenta box are to be adjusted in order to obtain a target initial condition (e.g. temperature, number density). The time intervals for different stages are not shown to scale.

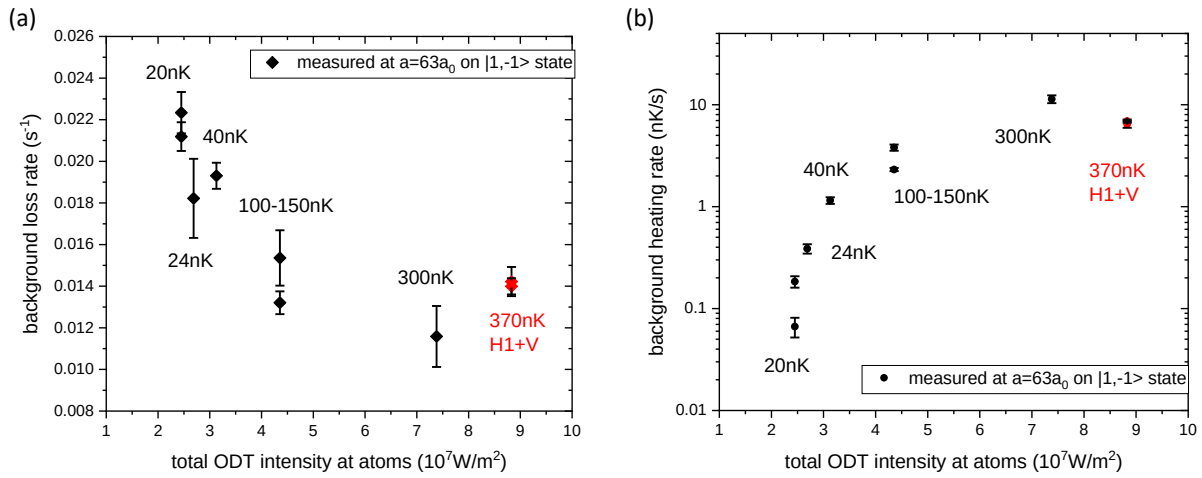

Figure 2.6: Background loss (a) and heating (b) rates measured at small positive positive scattering length for H2+V dipole trap except for the red circles which are for H1+V trap. The initial temperatures of individual data points are labeled on the plots.

Another important calibration of ODT is the trapping frequencies. We measure the trapping frequencies by using the slosh motion of the atoms which is initialized either with a short gravity pull or a side kick from a small magnetic field gradient. The parameters for these steps are carefully adjusted to give a small slosh amplitude compared to the cloud sizes. The initial condition of the clouds are chosen to give relatively long slosh time without significant dephasing. In the presence of the decay of oscillation contrast, we fit the slosh motion $y(t)$ into a damped sine curve with frequency f, damping time constant τ, time offset t_0 as below

$$y(t) = y_0 + Ae^{-t/\tau}\sin[2\pi f(t - t_0)], \tag{2.1}$$

and derive the natural frequency $f_0 = \left(f^2 + (1/\tau)^2\right)^{1/2}$ of the oscillation according to [38]. The trapping frequencies are compared to the calculated values based on measured beam waists and beam powers. Our trap model and calibrations are summarized in Fig. 2.7.

2.1.4 Laser Linewidth Measurements

We employ a self-heterodyne interferometer to detect the spectral linewidths of our Distributed Bragg Reflector (DBR) lasers which we use to inject Tapered-Amplifiers (TAs) for cooling and probing the atoms. The setup is shown in the schematic in Fig. 2.8. Our DBR laser diodes are fabricated by Photodigm (PH767DBR080T8, PH770DBR080T8). By virtue of the very short cavities, DBR lasers are highly robust against vibrations and can stay locked for weeks or even months. The drawback is that their linewidths are relatively broad, usually $150 - 600\,\mathrm{kHz}$. Along with other imperfections in the imaging system (e.g. non-perfect polarization), this can broaden the probe lineshape and lead to underestimated number density. These systematic effects usually are not an issue since the D_2-lines of alkali metals are as wide as $5 - 10\,\mathrm{MHz}$. But from time to time they do compromise the precision of bulk gas experiments. In particular, for the three-body recombination rate measurement (ref, chap4), $10\,\%$ uncertainty on atomic density calibration will cause the recombination rate coefficient to be off by $20\,\%$. Therefore it is necessary to run diagnostics on a regularly basis.

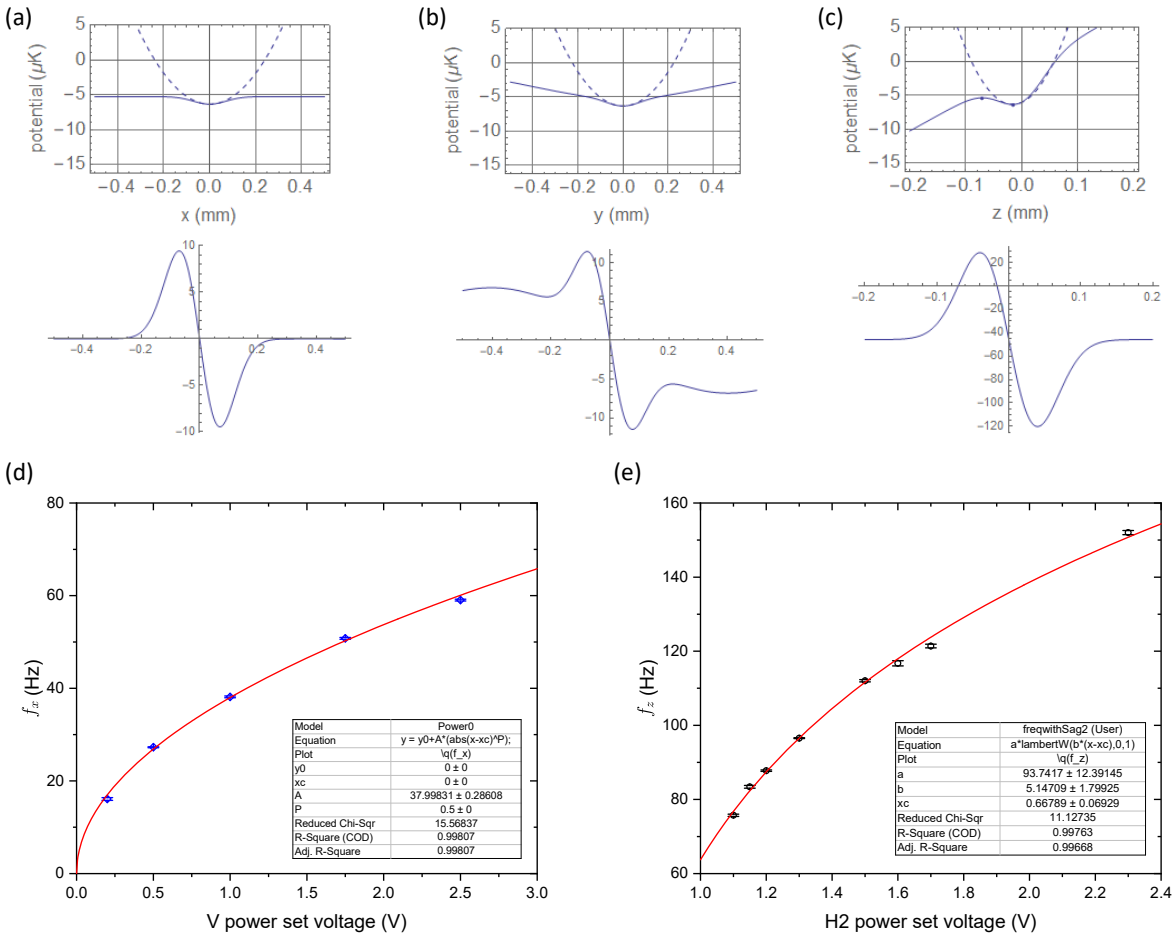

Figure 2.7: Calibrations of trapping frequencies for optical dipole trap. (a)(b)(c) Top panels: representative ODT potentials (solid curves) and parabolic approximation (dashed curves) at the trap center along three spatial dimensions; bottom panels: corresponding first derivatives, e.g. restoring forces along three dimensions. (d)(e) Calibrations of horizontal and vertical trapping frequencies with the slosh motion of the cloud. Fitting uncertainties are within 0.5 %. Red curves represent fitting functions as shown in the inset tables. Gravity sag is accounted for in the fitting function for vertical ($\hat{z}$) direction.

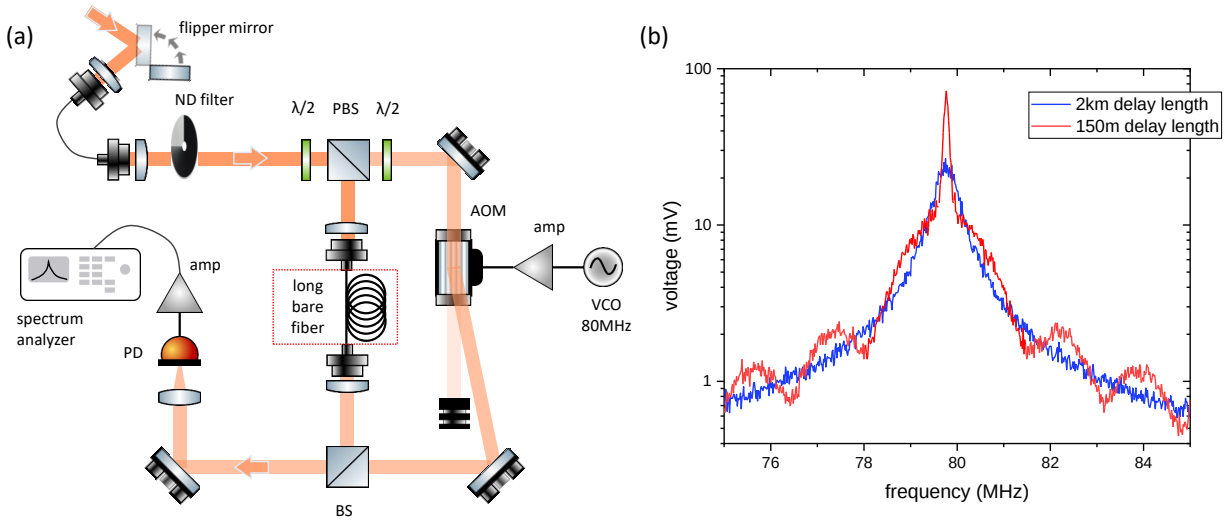

Figure 2.8: Self-heterodyne interferometer optical layout and beat note spectrum. (a) Schematic optical arrangement for the self-heterodyne interferometer. The fiber component inside the red dashed-line box that acts as the delay length can be swapped out. (b) Typical spectra downloaded from the spectrum analyzer. Two different delay lengths (blue and red lines) are plotted.

When there is no access to a high-finesse optical cavity or a reference laser as the local oscillator, self-heterodyne provides a convenient method to characterize a diode laser's linewidth. The basic idea of this technique is to convert the phase or frequency noise of the laser into the fluctuations of the light intensity via a Mach-Zehnder type interferometer [39, 40]. Specifically, the optical field to be calibrated is mixed with a delayed replica of itself (usually by an optical fiber) and then the AC component of the resulting beat note signal is detected on a fast photodiode (PD). One question people frequently ask is that how long the delay length needs to be to meet the requirement of being much longer than the coherence length of the laser. We tested the viability of this interferometric method by doing a systematic study on the delay fiber length. Low-cost fiber rings of various lengths (Fiber XP, singlemode FC-FC 9 μm) are used in the setup. In the ideal case, the phase dynamics of the interfering optical fields are completely uncorrelated on the PD. This leads to an easy-to-interpret power spectrum which consists of a broadband Lorentzian pedestal (coming from the white noise) and a small Gaussian portion (associated with the $1/f$ "pink" noise) near the peak (as depicted by the blue line in Fig. 2.8 (b)). For short delay lengths on the order of the coherence length of the laser, the phase dynamics of the interfering fields are partially correlated. This gives rise to a narrow δ-function peak sitting on top of a "scalloped-Lorentzian" (as depicted by the red line in Fig. 2.8 (b)) and complicates the analysis of the measured spectrum.

Generically the beat note signal on PD is associated with the Fourier transform of the intensity correlation function. By assuming a white noise spectrum on the laser frequency, we can explicitly write down the beat note signal as the following [39],

$$V(f) = V_1 V_2, \tag{2.2}$$

where

$$V_1(f) = \frac{A^4 \Delta_f}{\Delta f^2 + (f - f_0)^2},$$
$$V_2(f) = 1 - e^{-2\pi\Delta_f \tau_d}\left(\cos\left(2\pi\left(f - f_0\right)\tau_d\right) + \frac{\Delta_f \sin\left(2\pi\left(f - f_0\right)\tau_d\right)}{f - f_0}\right) + V_{\text{offset}}.$$

Here the delay time $\tau_d = L/c$, L is the difference in two beam path lengths which is approximately

equal to the length of the delay fiber, and c is the speed of light. Δ_f represents the laser linewidth. Note that the δ-function part is omitted for it introduces instability in the fitting process. When we use the above Eqn. 2.2 to fit our beat note signal, the delay length is a free parameter that is extracted from the period of the scallops (a good sanity check). In the limit of $\Delta_f \tau_d \gg 1$, Eqn. 2.2 reduces to a Lorentzian shape. As a comparison, we also fit the data with a Lorentzian function. Note that the laser linewidth equals one half of the full-width-half-maximum (FWHM) of the power spectrum in the case of a Lorentzian lineshape. The two fitting functions are presented in Fig. 2.9 (a) and (b) respectively.

As shown in Fig. 2.9 panel (c), the two functional forms give essentially the same result for delay lengths over 1km. For short delay lengths, Lorentzian function is no longer valid; however the full equation of the power spectrum can still predict a more or less correct linewidth. This simple study justifies the empirical criterion that the laser phases of the two arms can be considered uncorrelated so long as the delay length is at least 6-7 times the coherence length. We notice that the contrast of the scallops predicted by this white noise model is slightly off. By accounting for both white and pink noise [41, 40] in the frequency noise spectrum, one will be able to get a better fit over a larger dynamic range.

2.1.5 Absorption Imaging Analysis

We rely on absorption imaging method to obtain information of the temperature and number of the atoms. In the few-body physics studies, we typically work in the low-probe-intensity regime to adapt to the clouds' low density. Detailed explanation on the side-imaging setup, calibrations of the imaging resolution and the camera can be found in [27]. In this thesis I focus on the calibrations of the saturation intensity especially how we account for the Doppler shift induced by the atomic recoil momentum.

Absorption imaging detects the shadow cast by an atom cloud in a probe laser beam that illuminates the atoms. The atoms interact with the laser field and scatter photons into the vacuum modes. We use the cycling transition $|2, -2\rangle \rightarrow |3, -3\rangle$ to probe the atoms, which is a good two-level

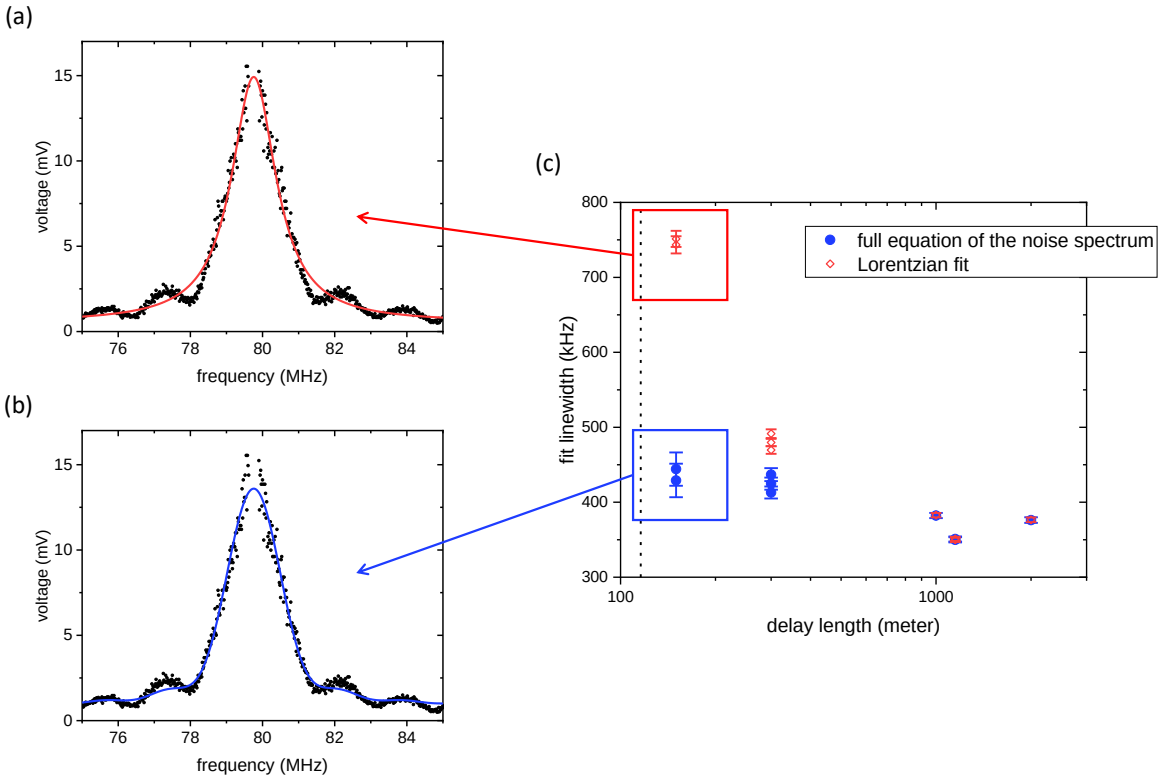

Figure 2.9: Comparison of the self-heterodyne beat note spectrum (black dots in panel (a)(b)) fit with Lorenztian (red line in (a), red open diamond in (c)) and Eqn. 2.2 (blue line in (b), blue solid circles in (c)). The vertical dotted line in panel (c) indicates the coherence length of the laser extracted from the fitting result in the long-delay-length limit, which is consistent with the value given by Photodigm.

approximation. The scattering rate of photons is [21]

$$\Gamma_{\rm sc} = \frac{\Gamma}{2}\frac{\tilde{I}}{1+4\tilde{\delta}^2+\tilde{I}}, \tag{2.3}$$

where $\tilde{I} = I/I_{\rm sat}$ is probe intensity in unit of the saturation intensity, $\tilde{\delta} = \delta/\Gamma$ is the probe frequency detuning in unit of the natural linewidth Γ. According to the modified Beer-Lambert law [42], the column density of the atoms $\rho = \int n(z)dz$ along the imaging line of sight $\hat{z}$ is

$$\sigma_0\rho = -\left(1+4\tilde{\delta}^2\right)\ln\left(I_f/I_i\right) + \tilde{I}_i - \tilde{I}_f, \tag{2.4}$$

where $\sigma_0 = 3\lambda^2/(2\pi)$ is the resonant scattering cross section for optical wavelength λ. In the limit of low saturation intensity $\tilde{I}_i \ll 1$ and at zero detuning, the right-hand-side of the above equation reduces to the optical depth expression that people normally use to obtain the atomic column density $\sigma_0\rho \approx {\rm OD} \equiv -\ln\left(I_f/I_i\right)$, with I_i and I_f being the light intensities in "light" (initial) and "shadow" (final) frames. In this case, OD is independent of probe intensity and probe duration. In practice, the signal detected on a camera is the total number of photons (or fluence, usually called "light counts") that arrive at the CCD within a certain probe duration which is gated by an AOM. A third fame taken with the camera shutter closed (called "dark" frame) is always subtracted out from the light and shadow frames so that the CCD offset is removed.

In the cases of light-weight atom species or a long imaging time, the atoms can be easily accelerated during the imaging process. An atom absorbs momentum kick of $\hbar k_{\rm r} = h/\lambda$ in $\hat{z}$ direction from scattering a single photon. The associated recoil velocity is $v_{\rm r} = \hbar k_r/m$ for atomic mass m. In addition to gaining a net momentum $\boldsymbol{p}_z$ in the longitudinal direction, the atoms also spread diffusively in the transverse directions due to a non-zero variance of $\boldsymbol{p}_z$. Note that the probe intensity's effect on $\boldsymbol{p}_z$ implicitly depends on the displacement $\hat{z}$ as the light field decays when traveling through the cloud. We implement a numerical model to simulate the longitudinal velocity and displacement of the atoms in coarse-grained space-time. The basic idea of the method is shown in Fig. 2.10. For practical imaging times of tens of μs, the atoms have gained velocity but not moved appreciably compared to the size of the cloud. Therefore the atoms can be presumed to be stationary during the imaging process.

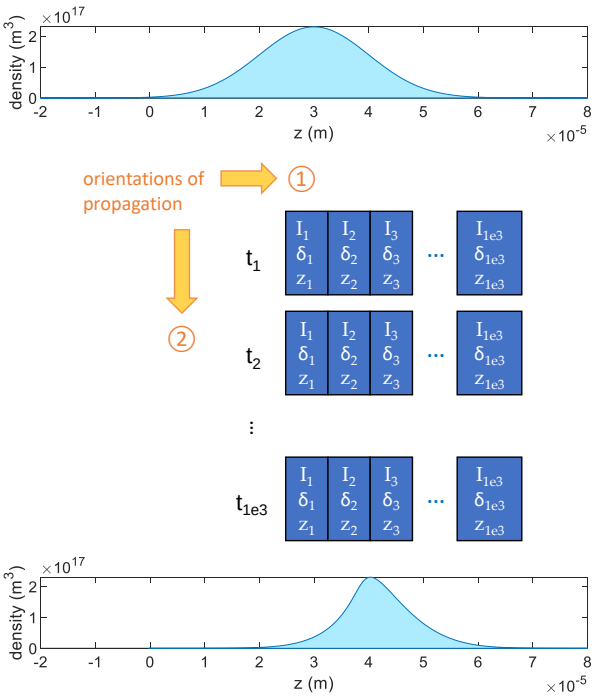

Figure 2.10: Coarse-grained method for absorption imaging simulation. The probe duration is 60 µs, $I/I_{\text{sat}} = 0.1$. The imaging time of an atomic cloud with density $n(z)$ is coarse-grained into a $10^3 \times 10^3$ grid. The absorption process of the probe light is propagated first along z then along t. The cross-section of the atomic density distribution along z is plotted before (top panel) and after (bottom panel) the imaging process. The initial distribution of the atoms is assumed to be Gaussian. See Appx. A for the algorithm of this model.

To visualize the effects of recoil momentum, we compare the predictions of OD vs. $I/I_{\rm sat}$ by Eqn. 2.4 and by the numerical model as presented in Fig. 2.11 panel (a). For short detection time of $10\,\mu$s, the modified Beer's law is a good approximation up to $I/I_{\rm sat} = 1$. For the detection time of 40 μs that we normally use on our side imaging, the two models start to deviate at $I/I_{\rm sat}$ as low as 0.1. Eqn. 2.4 overestimates the OD by assuming that the atoms scatter the light constantly at the maximal rate for detuning $\delta = 0$. As shown in Fig. 2.11 panel (b), the fictitious "sheets" of atoms at the front, middle and back of the cloud transport by different distances due to the different effective intensities seen by the atoms. For $I/I_{\rm sat} = 0.1$ and probe duration longer than $120\,\mu$s, the different atom sheets start to reorder. This will further complicate the dynamics and distort the original spatial distribution of the atomic density (i.e. Gaussian). Due to a limited depth of focus (DoF) of the imaging optics, this translation motion will also potentially compromise the imaging resolution.

A key parameter in absorption imaging technique is the saturation intensity $I_{\rm sat}$. The lack of a good knowledge of $I_{\rm sat}$ (in unit of light counts on a CCD camera) will introduce large systematic errors on the absolute values of atom number and density. This problem will become more serious when operating in the high-probe-intensity regime. One approach to measure $I_{\rm sat}$ is by directly calibrating the efficiency of the CCD camera (i.e. the product of quantum efficiency and analog-to-digital conversion gain), and translate the theoretical $I_{\rm sat}$ in unit of mW/cm^2 to camera counts. The accuracy of this method sometimes can be limited by not knowing the exact total transmission of the numerous optics in the imaging beam path (in particular in between the atoms and the CCD, including the science cell window, imaging optics, band-pass filters etc.). For instance, we found that some camera models in the lab have been installed an uncoated window for the CCD vacuum. For this reason we often choose to use atoms to calibrate $I_{\rm sat}$. We fix the probe duration in each scan and image the atoms with a wide range of probe intensities I. $I_{\rm i}$ and $I_{\rm f}$ are extracted by averaging the light counts within a small box at the center of the cloud where the column density is relatively homogeneous. We then fit the data of OD vs. $I_{\rm i}$ into the modified Beer's law and our numerical model respectively (see Fig. 2.12 panel (a)). Note that the fitting parameter $I_{\rm sat}$ is in

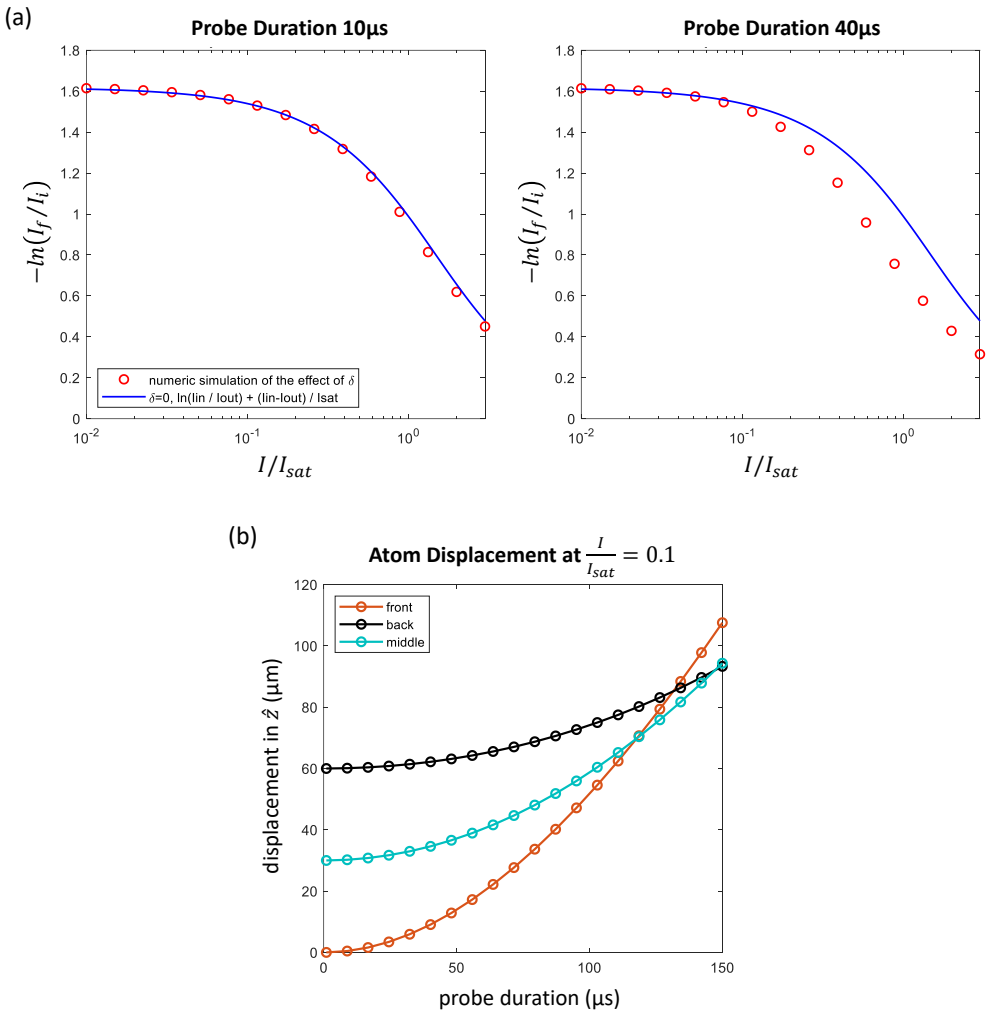

Figure 2.11: Absorption imaging simulation results. (a) Optical depth OD $= -\ln(I_f/I_i)$ as a function of the probe intensity I scaled by I_{sat}. Only in the limit of $I/I_{\text{sat}} \ll 1$ does OD/σ_0 represent the column density of the cloud ρ. Blue line: model using Eqn. 2.4; red open circles: our numerical simulation. (b) Displacements of atom sheets at the front, middle, and back of the cloud as a function of the probe duration. The simulation apparently breaks down when the different sheets of atoms start to reorder at around 120 μs.

fact the saturation intensity integrated over a certain probe duration.

As shown in Fig. 2.12 panel (b), fitting scheme using Eqn.2.4 yields an I_{sat} that depends on the probe duration in a non-linear fashion. On the contrary, our numerical model gives the expected linear behavior. This difference in I_{sat} qualitatively agrees with the observed difference in OD as discussed above (remember Fig. 2.11 (a)), – ignoring the recoil momentum leads to overestimated OD therefore a smaller I_{sat} value is needed to correct for the OD. As a sanity check, our I_{sat} for $40\,\mu$s probe duration is 3300(300) counts according to the numerical fitting model that includes the recoil effect. From an independent calibration of the CCD camera efficiency, I_{sat} turns out to be roughly 5008 counts for the same probe duration. The I_{sat} is only 1700(200) from the fitting function that uses the recoil-free model.

In the end, we apply our numerical model with calibrated I_{sat} to the raw images of the atomic cloud in a pixel-by-pixel manner. Fig. 2.13 panel (a) provides this conversion factor for certain probe durations in the standard low intensity regime of $I/I_{\mathrm{sat}} = 0.1$. Based on this conversion factor, we can estimate how large systematic error there will be if using Beer's law $\mathrm{OD} = -\ln\left(I_f/I_i\right)$ to approximate the column density of the cloud. For the lowest density clouds we have, this error is already on the order of 10 %. For imaging extremely low density clouds with relatively long probe pulses such as in [43], this correction factor can be even larger and becomes critical in obtaining the correct shape of the cloud.

2.1.6 Magnetic Field Control

Rf and microwave spectroscopy provides an essential component of the toolkit for quantum gas experiments especially in quantum state preparation and precision metrology. To achieve high accuracy with this technique, a stable control of the DC magnetic field plays is critical. The shot-to-shot magnetic field fluctuation in our experiment is determined to be $2-5\,$mG (standard deviation). And benefiting from the long-term stability of its absolute value, the uncertainty on the magnetic field can be averaged down to within 1 mG by taking only 20 shots. We calibrate our magnetic field noise by driving different hyperfine transitions on the atoms (i.e. $|1,-1\rangle \rightarrow |2,0\rangle$,

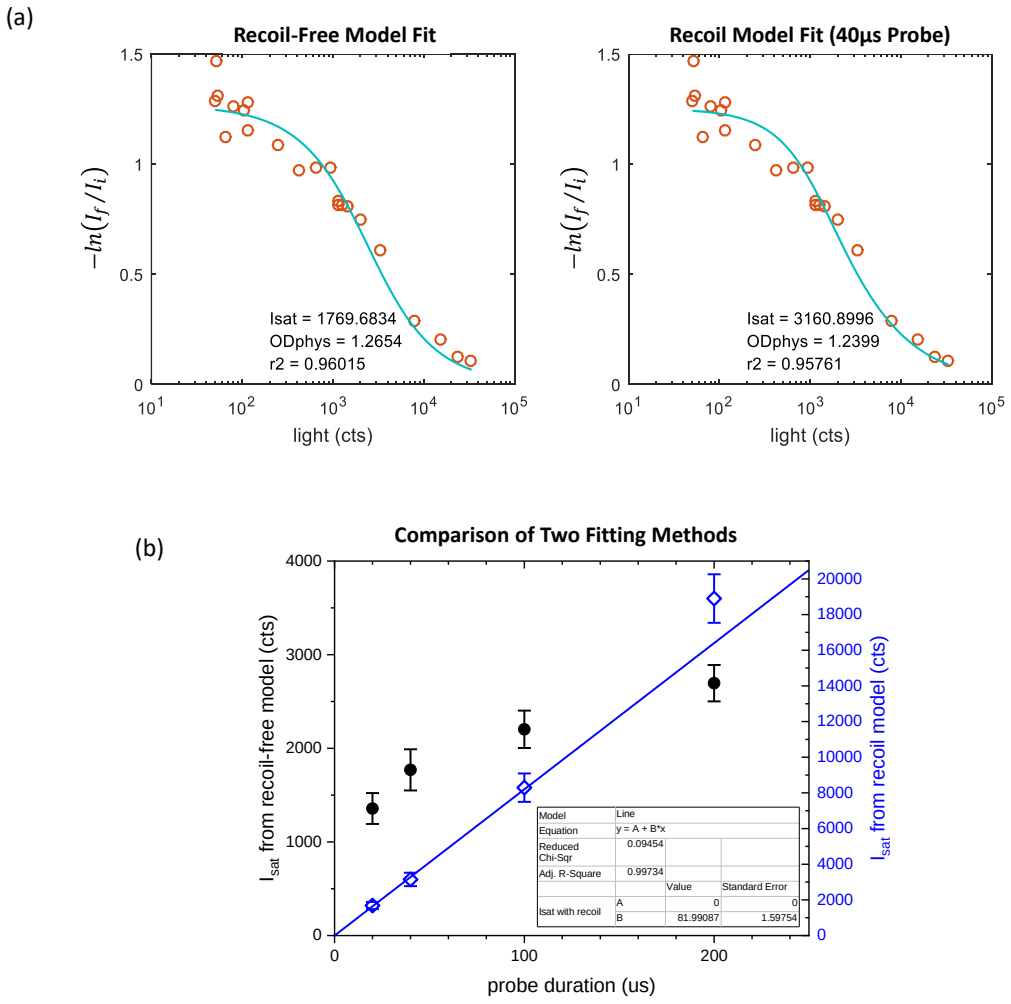

Figure 2.12: Comparison of two fitting models for I_{sat}. (a) Two fitting protocols using Eqn.2.4 (left panel) and our numerical model that takes into the recoil-momentum (right panel) respectively. The data is taken with 40 μs probe duration. (b) Comparison of the results from two fitting models (black circles: left y-axis; blue diamonds: right y-axis) as a function of probe duration. The solid blue line is a linear fit to the blue diamonds with fitting parameters listed in the inset table.

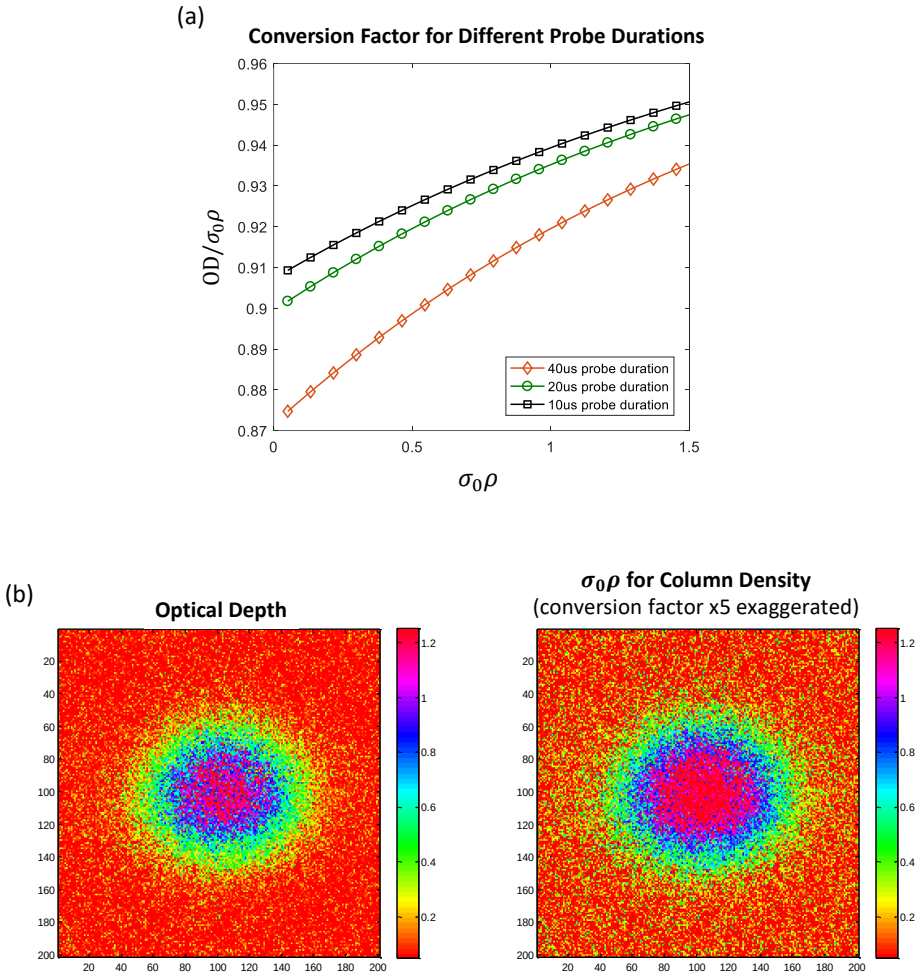

Figure 2.13: Application of the recoil model to the measured optical depth. (a) OD to column density conversion factor for different probe durations at $I/I_{\text{sat}} = 0.1$. (b) Application of the conversion factor to a raw image (left penal) pixel by pixel. The conversion factor is enhanced by 5 times to visualize its effect on the density distribution of the cloud (right panel).

$|1,-1\rangle \rightarrow |2,-2\rangle$, whose $\Delta\mu$ differ by a factor of 10) and measuring the variance of the transition fraction $P = N_{|2,x\rangle}/N_{|1,-1\rangle}$ $(x = 0, 1)$ at the microwave detuning where $P \approx 0.5$. The shot-to-shot atom number fluctuation is independently checked at zero detuning where $P = 1$ and turned out to be constantly below 2%.

We put a lot of efforts into improving the stability of the bias field control. The schematic diagram for our science coils control system can be found in Fig. 2.43 in [27]. This setup is built based on a JILA coil driver (JD013A2) designed by Brian Demarco. This PI feedback servo includes only a minimal number of op-amps hence suffers less from the internal noise. Two copies of this coil driver with different servo gains are combined at the servo output in order to broaden the dynamic range. High current up to over 300 A in science quadrupole trap and low current less than 15 A in bias field can be switched back and forth. An Insulated-Gate Bipolar Transistor (IGBT, Semikron) serves as the current actuator. Fluxgate transducers (Danisense for in-loop, LEM for out-of-loop) along with high stability sensing resistors (Vishay VPR221ZT) are implemented to monitor the current.

As to the rf and microwave sources, we employ a programmable frequency generator (versatile frequency generator, VFG-150) to produce fast pulses with the frequency, amplitude and phase edited in a step-by-step manner. It can output frequencies up to 150 MHz and features by a step switching time of 5 ns with approximately 1000 step number. We control the VFG via USB 2.0 which typically takes a couple of seconds to upload each sequence [1] . This data transport happens during MOT filling stage so as not to take extra experiment time. The signal from VFG is mixed up to half a GHz with two frequency synthesizers (from Keysight) to generate the hyperfine transition frequencies. To do so we picked a Mini-Circuits mixer (part number ZX05-10+) that has the weakest harmonics among various models. Analog frequency modulation has also been implemented on the synthesizers with external DAC for modulating slower pulses. The synthesizers are programmed via SCPI commands. Air-cooled amplifiers from Mini-Circuits (20W, $20 - 1000$ MHz, part number

[1] The hardware driver and Matlab scripts for VFG-150 are provided by Photonics Technologies Ltd and Department Physik, University of Siegen.

ZHL-20W-13+) are installed to broadcast the signal. Note that we use dedicated Topward power supplies and AC outlets for these big rf amplifiers because each one of them can draw huge amount of power from the wall transiently during the pulses and also that the rf signal can easily propagate backwards into our electronic network through any poorly-shielded connectors or cables.

We use home-made loop antennae to deliver the rf and microwave to the atoms. The atoms are in the near-field regime of the dipole radiation hence mainly sense the magnetic field that oscillates in the axial direction. Our science cell is currently equipped with 5 antennae as shown in Fig. 2.14 panel (a). A photograph of a one-loop antenna can be found in the inset of Fig. 2.14 panel (b). The head of our antennae are made of 16 gauge magnetic wire and semi-rigid co-ax. The co-ax supports the antenna in a robust way so that the antenna is not in contact with nearby dielectric materials and also its coupling to the environment is maintained at a constant level. All these help to keep a steady radiation efficiency and thus reproducible Rabi frequency from day to day. The downside of a co-ax is its relatively high capacitance of about 30pF/ft. This effective capacitance together with the number of loops determine the maximal frequency we can operate. The antenna head is mounted on a impedance matching box through non-magnetic SMA connectors. High-voltage trimmer capacitors up to 100 pF are used to tune the resonance frequency as well as to match the impedance. By carefully tuning the antenna after it is mounted in place, return loss is limited to be on the order of a few percent (see Fig. 2.15 for some reflection measurements).

After we installed the 105 MHz longitudinal antennae which are co-linear with the bias coils, we found that their radiated powers are strongly coupled into the bias coils and influence the bias field servo system. In the far field, this rf radiation mainly propagates in the horizontal plane. It can unlock all lasers in the lab if pulsed on for a few seconds at full power. RFI rectification happens when rf signal gets picked up by conductors at the inputs, outputs and power supply pins on op-amps or in-amps through capacitive, inductive or radiation coupling. We made a series of trials to screen out this spurious signal on our bias-field control system. For instance we implemented low-pass filters on the inputs of the bias servo, used shielded twisted-pair cable on the servo output, enclose all feedback components in a shielding box, and relocated the setpoint signal from an

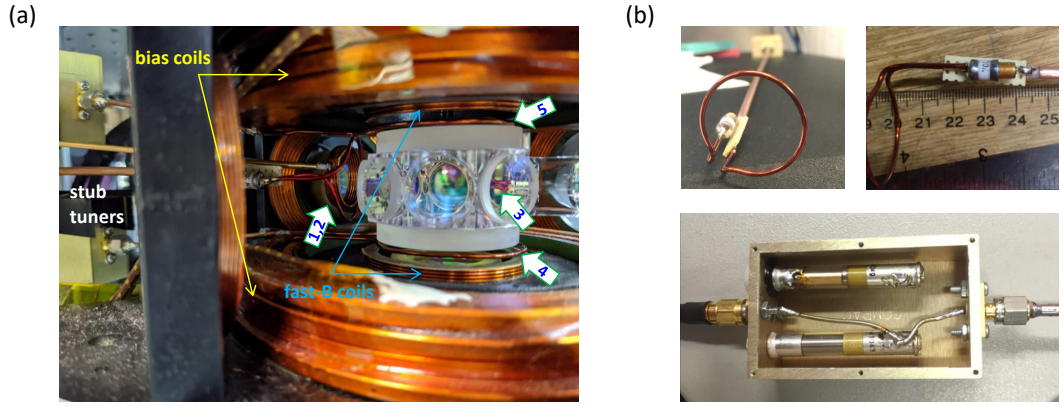

Figure 2.14: Photographs of rf/microwave antennae mounted surrounding the science cell and antenna components. (a) Five antennae surrounding the science cell can be seen on this photograph. They are mounted as close to the atoms as possible. We have three transverse antennae (labeled 1,2,3) that address spin-flip transitions and two longitudinal antennae (labeled 4,5) that address non-spin-flip transitions. The bias field along vertical direction is provided mainly by bias coils and sometimes by fast-B coils for fast switching time. (b) Top left: photograph of a single-loop antenna head. The diameter of the loop of about 2.5 cm is made to be slightly larger than the side windows on the science cell. Top right: small trimmer capacitor that we use for tuning the resonance frequency of the antenna. Bottom: big trimmer capacitor for impedance matching enclosed inside a rf-shielded enclosure.

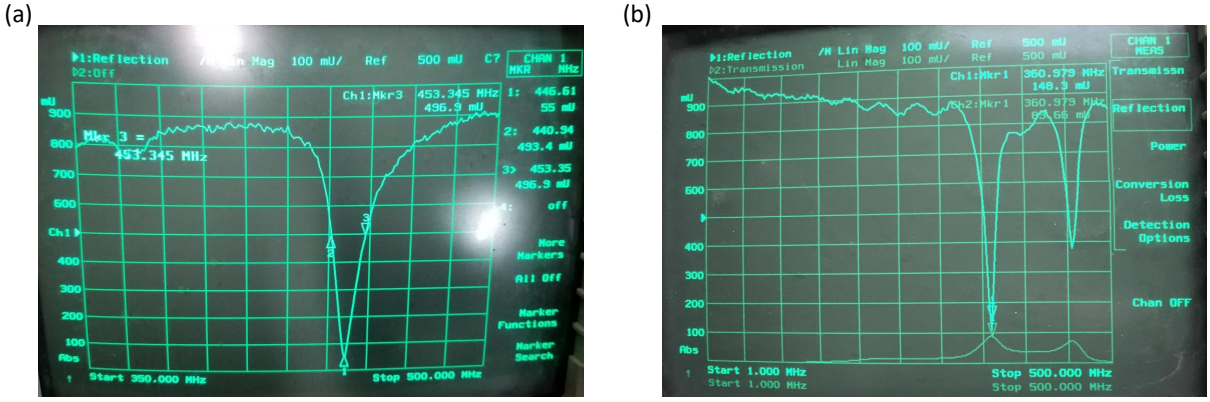

Figure 2.15: (a) Reflection (on linear scale) of a microwave antenna measured on a network analyzer as the in-place tuning of the antenna is finished. The Q-factor is about 100 in our case. (b) Reflection (top trace, channel 1) and transmission (bottom trace, channel 2) received by a pick-up coil. We always use a small-diameter (a few mm) pick-up antenna to detect the radiation as we do preliminary tunings. This is to ensure that the observed drop in reflection actually corresponds to a peak in power radiation. Sometimes there are electronic resonances that occur mainly within the tuning box (e.g. the signal to the right on the figure) usually lying at higher frequencies. These spurious signals are misleading since they can also be received by the pick-up antenna.

FPGA board in the control computer to an independent DAC board inside the shielding box that is controlled only through data and digital lines. We found that the rf radiation enters into our bias servo system mainly through the inputs (i.e. signal from the current transducer) and also gets picked up on the servo output to the gate of IGBT. We made some plug-in low-pass filters that can be easily installed (as shown in Fig. 2.16). Most rf noise can be rejected by these filter boxes. Doubling the number of these filter boxes on each port does not further suppress the noise. We also replaced the servo output cable with a short well-shielded twisted-pair cable (silver plated copper). These two remedies have already greatly improved the robustness of the bias field control system. We found that adding clamp-on ferrite chokes or Mini-Circuits in-line low-pass filters have very minor effects in our case.

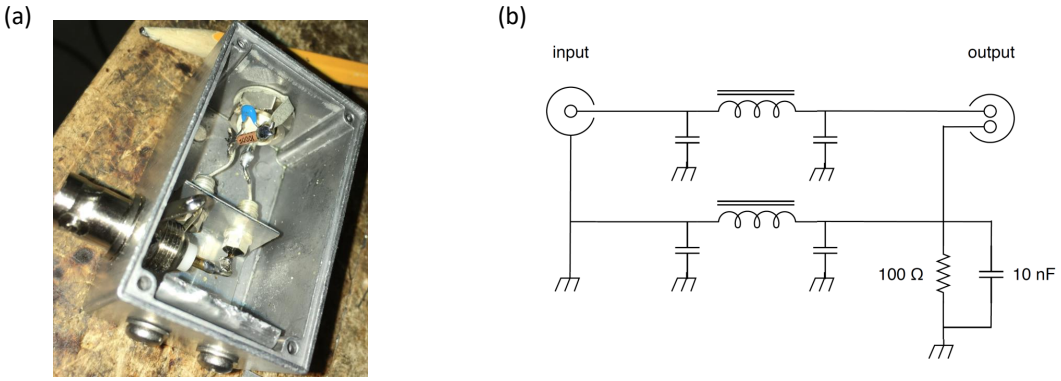

Figure 2.16: Photograph (a) and schematic (b) of the plug-in low-pass filter. We use bolt-in π-filters (5500 pF, cutoff frequency a few MHz) to shunt rf noise to the chassis.

We always use atoms as the ultimate caliper for rf rectification effects considering that magnetic field or current sensors potentially also suffer from the rf radiation and can shift their measurement in an unpredictable way. A 2 ms rf signal at about 105 MHz is pulsed on at its full power 20 W to perturb the bias servo system; meanwhile a second Gaussian π-pulse is sent to the atoms for field detection by driving a hyperfine transition. The Gaussian pulse peak power is only 0.1% that of the rf square pulse. As presented in Fig. 2.17 panel (a), with the original bias servo setup, the rf radiation can cause a 0.25 G/W shift on the DC level of the bias field. With the modified setup,

we are able to mitigate the shift down to 0.15 mG/W (150 ppm/W). This level of stability on the magnetic field plus the high power rf signal allow us to drive some molecule-to-molecule transitions at certain frequencies. However unfortunately due to the extremely small dipole moment of these transitions we ended up still being limited by the Rabi frequency. And adding more power to the antennae or shifting the resonance frequency to a few MHz lower value resulted in higher noise level on the bias field, causing us to to lose our precision on the spectroscopy.

2.2 High-Resolution Top Imaging

We take the advantage of the large optical access on the top and bottom windows on the science cell to do high-resolution *in situ* imaging of the density distributions of the atoms. This top imaging scheme is compatible with our pancake-shaped dipole trap and ideal for 2D or lattice-based cloud geometry.

2.2.1 Design of a Compact Imaging System of NA 0.4

The main idea of our high-resolution imaging system design is to achieve diffraction-limited performance with minimal pieces of optics in the objective lens so that we have enough clearance for our moving cart coils. We end up using a Thorlabs CNC-polished asphere (part number AL4532-B) as the main component that sets the numerical aperture (NA), together with a thin plano-convex (LA1978-B) to compensate for the optical aberrations induced by the cell window. The two pieces are mounted in an Ultem holder which is eddy-current-free. The structure of our objective lens is shown in Fig. 2.18. The specifications of the objective according to the design are listed as the following: effective focal length 31.03 mm; NA (defined as the acceptance cone) 0.384; exit pupil diameter (defined as the image of the stop) 26.15 mm; limiting aperture (limited by the spacer ring in between the two pieces) 22 mm; Airy disk radius at 767 nm 1.13 µm. The eyepiece we use is a 1500 mm plano-convex from CVI optics (PLCX-50.8-772.6-C). This combination of objective and eyepiece gives a paraxial magnification of 48.70. As a comparison, our side imaging that we mainly use for time-of-flight measurements has NA about 0.17 and Airy disk radius of 3.49 µm.

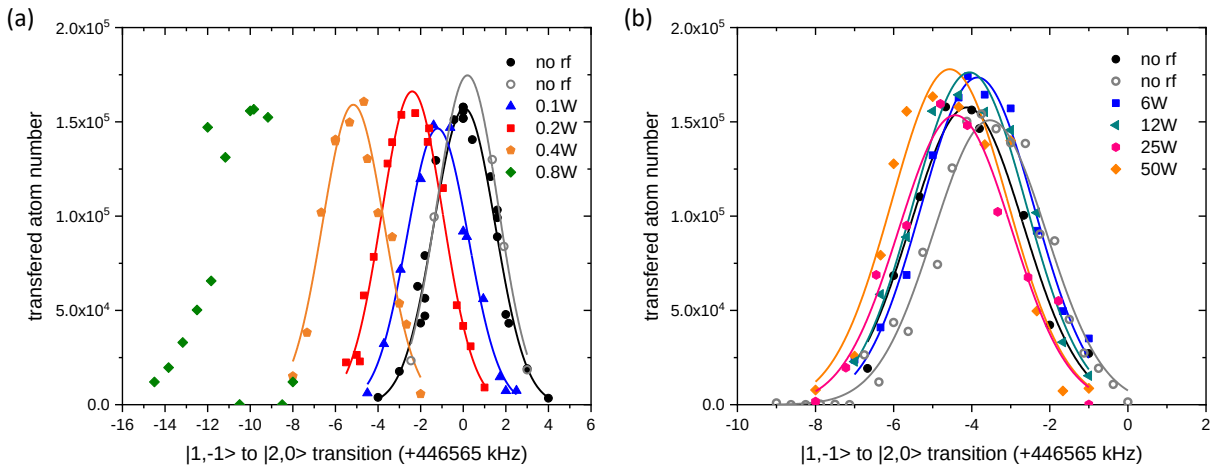

Figure 2.17: Rf spectra taken with various rf radiation power being present. The magnetic momentum of the hyperfine transition used here is about 0.15 kHz/mG. (a) Without good shielding in the servo system, the magnetic field is shifted significantly by the rf signal. (b) With proper shielding and filtering, the rf signal neither affects the center nor the width of the rf lineshapes. We took microwave spectra without rf radiation being present before and after all the scans in order to trace the background magnetic field fluctuation that takes place during the experiment. Solid lines are fitting curves with Fourier-limited Gaussian function.

Its magnification is only 6.7. The top imaging objective requires more delicate alignment than the side imaging lenses. In order to have all the degrees of freedom on the lens mount, we installed a linear translation stage from Newport for XYZ axes, a goniometer from Edmund (66-534) for pitch axis, and a rotary stage from Edmund (66-516) for roll axis.

The big asphere in our objective is trimmed down to fit in the small empty space encircled by our magnetic coils. As a quick assessment of the quality of this asphere, we generate an 1 inch diameter collimated beam with it and then use a lateral-shearing interferometer to check the wavefront errors qualitatively. We did this test on the two big aspheres that are cut by JILA shop and Thorlabs respectively. This method turned out to be limited by the imperfect point source that we make by focusing down a laser beam with a small molded asphere (8 mm focal length, NA 0.5, part number C240TME-B). As shown in Fig. 2.19, the distortions on the interference fringes for the two lenses are very alike. The fact that this distortion pattern is independent of the rotation angle of the big aspheres indicates that the aberrations are mostly from the molded asphere. In the end, we picked the shop-cut one that has relatively less distortions.

2.2.2 Bench Test Setup

To calibrate the resolution of the top imaging system, we built a testing setup with a small pinhole as the point source, and a sample window to emulate the cell window. The optics layout is presented in Fig. 2.20. The pinhole is mounted on an indexed repeatability mount (part number NX1NF) so that it can be swapped out easily without too serious misalignment. We also prepared larger-diameter pinholes (1 µm, 10 µm) for the purpose of preliminary alignment, – larger pinholes allow higher transmitted power therefore assist the concentricity and back-reflection alignments of the downstream optics. A photograph of the point source setup is shown in Fig. 2.21 panel (a). We purchased the pinholes from National Aperture. The smallest pinhole we have (part number 1-0.5+HS) is 0.5 µm in diameter and the tunnel is about 3 µm thick. An SEM image of the pinhole is shown in Fig. 2.21 panel (b). It could take many hours to locate the real pinhole among all the dust particles under the SEM microscope. We found it easier to look for the perforation structure

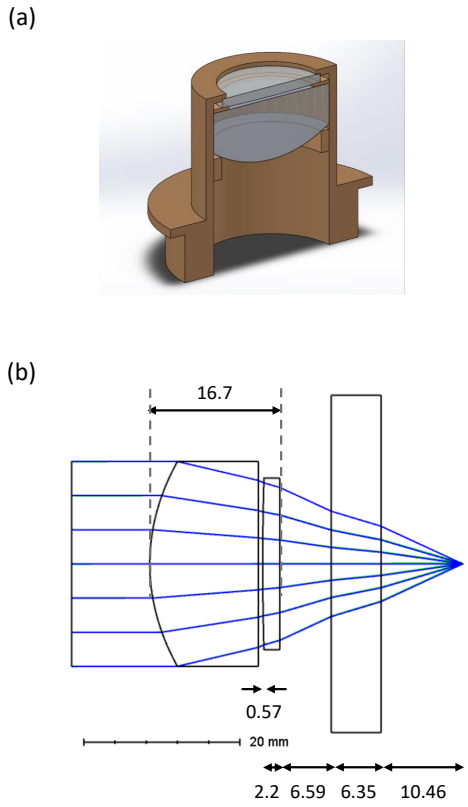

Figure 2.18: Design of our compact top imaging system in (a) Solidworks and (b) Zemax. The numbers in (b) are central thichnesses in unit of mm.

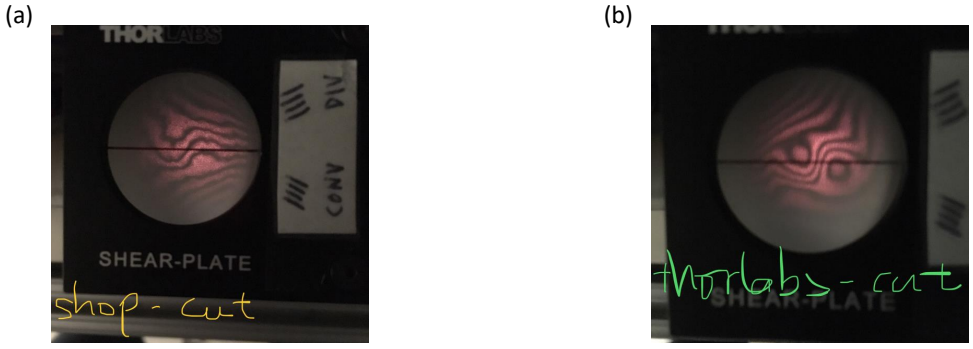

Figure 2.19: The JILA shop-cut (a) and Thorlabs customized (b) aspheres display similar fringes under a shearing interferometer. This pattern is actually associated with the 8 mm molded asphere that we use to generate the point source.

on the back of the substrate. A Vortex laser at 767 nm with about 5 mW output power serves as the light source. By focusing down the beam on the pinhole with a 30 mm achromatic doublet, we are able to get a sufficient amount of 100 nW light traveling through the pinhole.

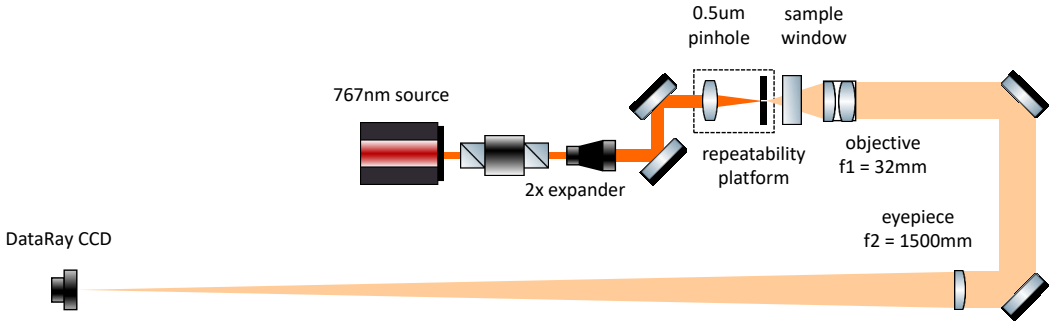

Figure 2.20: Optics layout for the top imaging bench test setup.

The image of a small pinhole is called the *point spread function* (PSF) of an imaging system. As been plotted in Fig. 2.22, the intensity of a pinhole image can be approximated by the Airy disk function

$$I(r) = \left(\frac{2J_1(r)}{r}\right)^2, \tag{2.5}$$

where J_1 is the Bessel function of the first kind of order one, r is the radial coordinate in the Fourier plane of the objective. We can relate r to the Cartesian coordinates in the image plane through $r = 2\pi(x^2 + y^2)^{1/2}/(M\lambda\text{N.A.})$, where x and y are in unit of pixels, λ is the wavelength of the light, M is the magnification of the imaging system, and N.A. stands for numerical aperture. By fitting the PSF with the Airy disk function, we obtain an NA of about 0.4, which meets our expectation. The Strehl ratio is estimated to be over 90%, well within the diffraction limit.

After finalizing the alignment, we study the relative sensitivity of each component in this setup. We found that the tilt degree of freedom on the objective is critical in attaining the smallest spot size. It is coupled to the translation degree of freedom so both of them need to be adjusted at the same time. We found that it is actually easier to see the tilt by purposely defocusing the

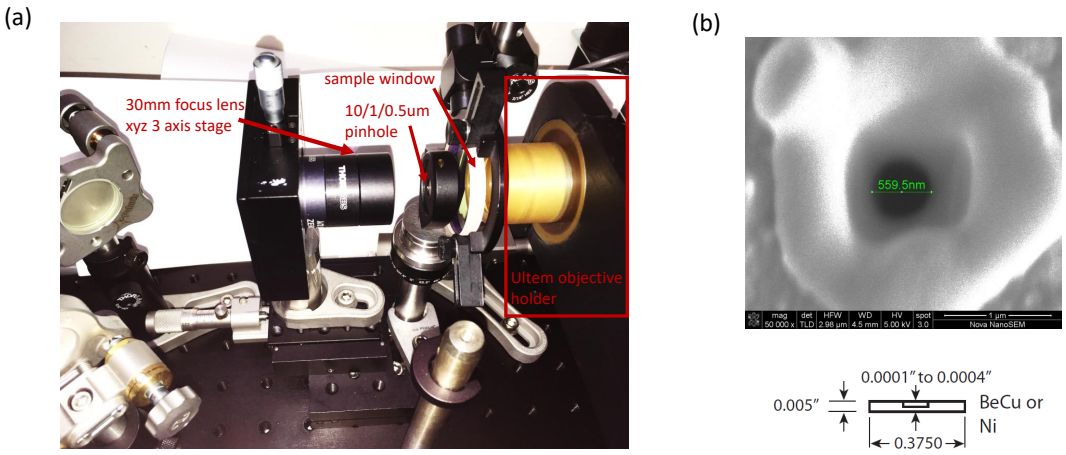

Figure 2.21: (a) A photograph of the point source setup with part numbers labeled on the picture. (b) An SEM image of the 0.5 µm pinhole (top) and dimensions of its substrate (bottom).

objective and using the higher order annular structure as a reference. We use micrometers on all five knobs on the objective lens mount including translations and rotations. The longitudinal translation knob consists of fine and coarse micrometers for easy focusing. The concentricity of the asphere and plane-convex is another crucial factor. Assembling the lenses is a meticulous job. Machining errors on the lens mount and the spacer ring can lead to extra aberrations especially anisotropic portions. We found that the tilt degrees of freedom on the sample window and eyepiece lens do not matter as much. Regular knobs on these two optics elements would suffice. The translation of the sample window is also insensitive for this kind of intermediate NA.

On the bench test setup, we use DataRay beam profiling cameras to image the PSF. The two models we use have pixel sizes of 3.2 µm and 4.4 µm. For such small pixels, discreteness of the sampling is not a concern. For our science camera, however, the pixel size is as large as 16 µm. We chose the magnification to be 48 so that our Airy disk radius is a couple of times larger than a single pixel. In general, the Nyquist criterion can be satisfied when the Abbe radius is at least twice as big as the pixel size [2] . To study how pixelation can affect the imaging resolution, we numerically bin the adjacent pixels into groups to mimic the effect of sampling with larger pixels. The borders of the groups are selected in a random fashion. As shown in Fig 2.23, larger binning numbers lead to an effectively larger spot size as well as a slightly wider spread in the spot sizes. Images taken with our science camera are equivalent to a binning number of 5 on this DataRay camera whose pixel size is 3.2 µm. We verified that for a 5×5 binning the resolution stays as good as the no binning case.

Finally we investigate the finite depth of focus (DoF) effect which is of practical importance to us due to the thickness of the cloud. The DoF is characterized by the Rayleigh length of a Gaussian beam and is inversely proportional to NA squared. In the test setup, we spatially translate the objective and observe the evolution of PSF as a function of the longitudinal displacement. As shown in Fig. 2.24 panel (a), the central peak of the PSF diminishes very quickly and also asymmetrically on different sides of the focal plane. This will lead to a complicated resolution function on the clouds

[2] The Abbe radius is defined as $r_{\mathrm{Abbe}} = \lambda/(2\mathrm{N.A.})$. See Section 2.2.3 for detailed analysis of the optical aberrations.

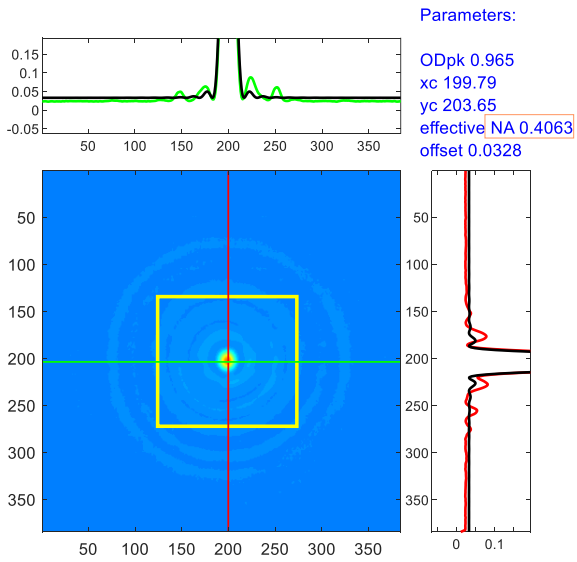

Figure 2.22: Point spread function (PSF) of the top imaging system generated from a 0.5 µm pinhole. The region inside the yellow square is fit into Airy disk function and the fitting parameters are shown in the top right corner. Slices of data cut through the center of the cloud along the vertical (red) and horizontal (green) lines are shown in the right and top panels respectively. The corresponding fitting functions are plotted as black lines in each panel. Both panels zoom in on the wiggles around the main peak.

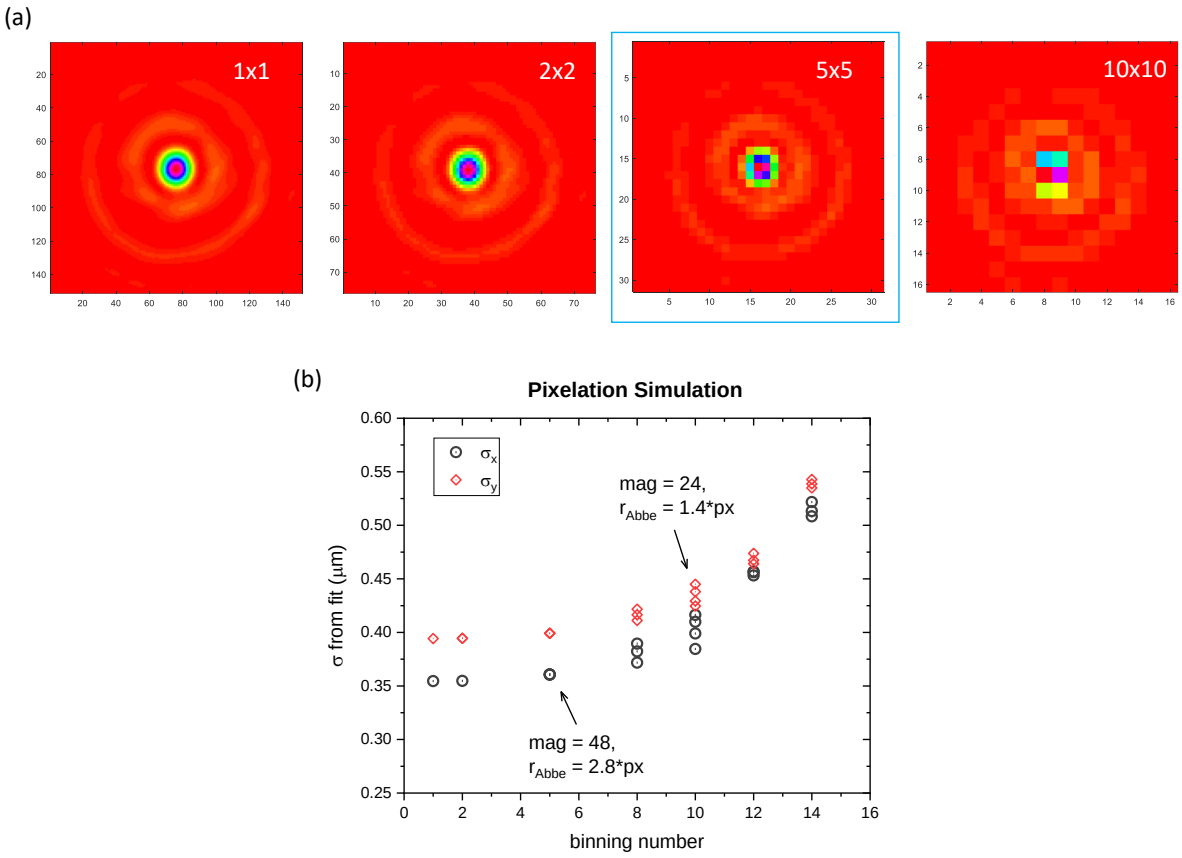

Figure 2.23: Study the pixelation effect by numerically binning the PSF. (a) Original image (left-most) and the original image binned by different numbers. The third image from the left (5×5 binning) is what the PSF would look like on our science camera. (b) By doing various binning numbers on the original image and fitting the binned images into a 2D Gaussian function, one can see how the artificial large pixels compromise the imaging resolution through undersampling. The Gaussian r.m.s. width σ is related to Airy disk radius through $\sigma \approx 0.4 r_{\mathrm{Airy}}$. The difference in σ_x and σ_y indicates anisotropic optical aberration terms.

that are thicker than 10 µm along the vertical direction. We machined two threaded apertures out of Ultem so as to iris down the objective to as small as half inch in its diameter. This gives an elongated DoF up to 26 µm as measured in Fig. 2.24 panel (b). The spot size at focus in this case is correspondingly twice as big as that of the full aperture.

2.2.3 Analysis of Optical Aberrations

As can be seen from the PSF fitting in Fig. 2.22, although the Airy function yields a reasonable value of NA, it does not describe the amplitudes of wiggles perfectly. This deviation is due to the presence of optical aberrations, i.e. the objective lens imprints a spatially dependent phase distortion on the wavefront of the light field in addition to its primary effect which is to cut off high spatial frequencies in the momentum space. We played with the measured PSF and determined the type of aberrations in terms of Zernike polynomials.

An optical imaging system transforms radiation sources into blurred pictures. The pictures can be mathematically expressed as a convolution of the original distributions of the radiation with the point response function of the imaging system, – this is where the PSF comes into play. The PSF in momentum space is named *modulation transfer function* (MTF) (or *optical transfer function* (OTF)) which is basically a low pass function that only allows information with spatial frequencies below the so-called *Abbe frequency* to be transmitted. Both PSF and MTF are related to the *exit pupil function*, which describes the physical process that actually happens when a radiation field passes through the objective lens. For an ideal lens, it is a box function with unity transmission. We now derive the PSF and MTF associated with an ideal pupil for fluorescence and absorption imaging respectively.

In an imaging process, the incident field E_0 is shone on an atom (a realistic point source) and scattered by the atom in the object plane. The scattered field in the image plane can be written as $\Delta E \propto E_0 e^{i\delta}\tilde{p}(\mathbf{k})$, where δ is phase shift due to probe laser detuning, $\tilde{p}(\mathbf{k})$ is Fourier transform of the exit pupil function $p(\mathbf{r})$. Here, $\mathbf{k} = 2\pi(\text{N.A.})\mathbf{r}/(\lambda r_a)$ relates the position $\mathbf{r}$ in the object plane to the position $\mathbf{R} = M\mathbf{r}$ in the image plane, where r_a is the radius of the pupil aperture and M is

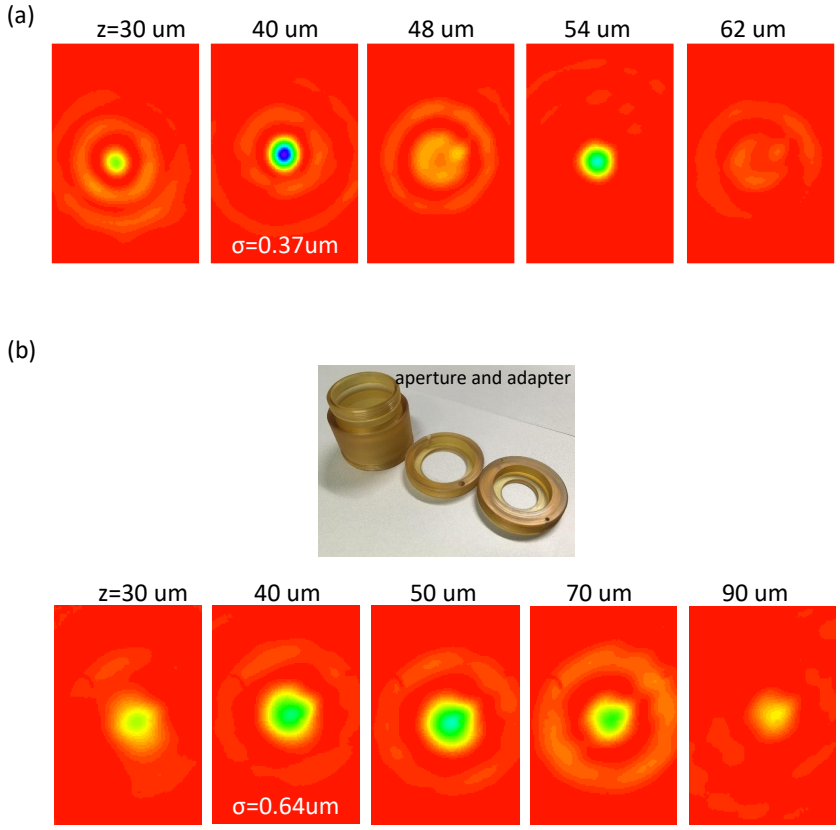

Figure 2.24: Explore the finite depth of focus of the PSF. (a) By translating the objective lens along longitudinal direction $\hat{z}$, the central peak on the PSF diminishes very quickly. This shows the sensitivity of the PSF to defocus for this full aperture of about 23 mm n diameter. The corresponding Rayleigh length is only 5.5 µm. (b) We made apertures in different diameters (three-quarter inch, half inch) to iris down the objective. As shown in the bottom row, an aperture of 12 mm in its diameter leads to a longer Rayleigh length of about 26 µm at the price of a twice bigger spot size at focus.

the magnification [44]. For fluorescence imaging, the intensity of the scattered light is collected on a camera. The PSF of this imaging process is therefore

$$P(\mathbf{r}) = |\Delta E|^2 \propto |e^{i\delta}\tilde{p}(\mathbf{k})|^2. \tag{2.6}$$

For absorption imaging, the image of an atom is instead formed by interfering the scattered field with the incident field. In the limit of a small scattering amplitude, the transmission of the incident beam is $t^2 = |E_0+\Delta E|^2/|E_0|^2 \approx 1+2\mathrm{Re}[\Delta E/E_0]$, where Re[.] refers to the real part [45]. Therefore the PSF in absorption imaging is

$$P(\mathbf{r}) \propto \mathrm{Re}[\Delta E/E_0] = \mathrm{Re}[e^{i\delta}\tilde{p}(\mathbf{k})]. \tag{2.7}$$

In both imaging schemes, the MTF is the Fourier transform of the PSF, i.e. $M(\mathbf{k}) \equiv |\tilde{P}(\mathbf{k})|$. In Fig. 2.25, the PSF and MTF for an ideal exit pupil are plotted in radial coordinate since both functions demonstrate azimuthal symmetry.

In practice, an optical lens can introduce spatially inhomogeneous transmission as well as phase distortions. This leads to a complex exit pupil function

$$p(r,\theta) = e^{i\Phi(r/r_a,\theta)}. \tag{2.8}$$

We assume a homogeneous unity transmission across the pupil here. By plugging Eqn. 2.8 into Eqn. 2.6 or Eqn. 2.7, we can obtain the resolution functions for fluorescence and absorption imagings in the presence of optical aberrations. In general, $\Phi(r/r_a,\theta)$ can be expanded in *Zernike polynomials*, among which the leading terms are known as tilts, astigmatism, defocus, trefoil, coma, spherical, etc. [46].

We fit our measured PSF from the pinhole test with the wavefront distortion that consists of the first eight terms of Zernike polynomials [3] . We expand the phase of the pupil function as the

[3] There are different conventions for the prefactors in these terms. We simply followed the basis functions from *Wikipedia*.

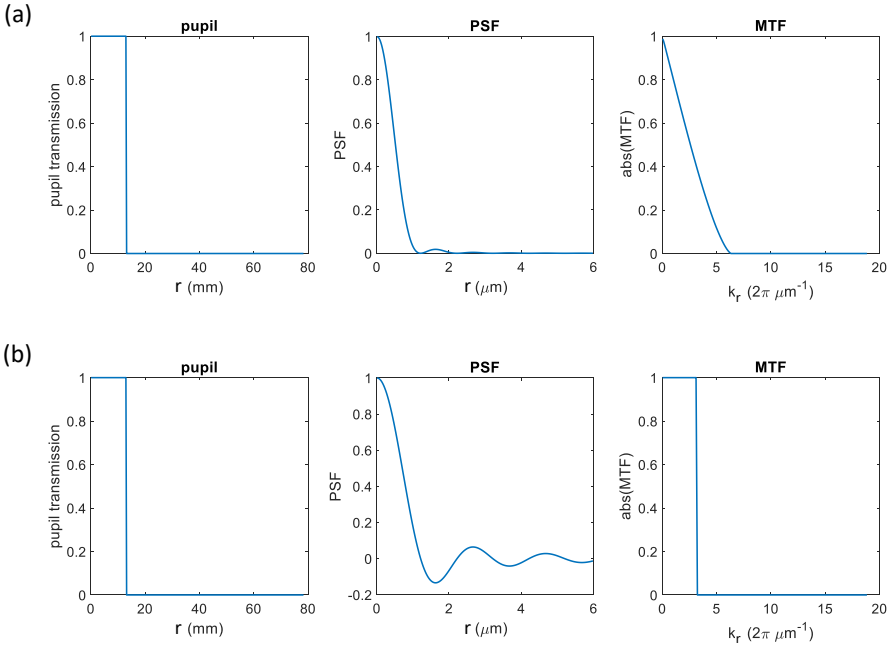

Figure 2.25: The PSF and MTF associated with an ideal pupil for fluorescence (a) and absorption imaging (b) as a function of radial coordinate. The NA and λ used here are the same as in our top imaging system.

following series

$$\begin{aligned}\frac{\Phi(r/r_a,\theta)}{2\pi} &= S_0\sqrt{5}\left(6\left(\frac{r}{r_a}\right)^4-6\left(\frac{r}{r_a}\right)^2+1\right)\\ &+\alpha_1\sqrt{6}\left(\frac{r}{r_a}\right)^2\cos 2\theta+\alpha_2\sqrt{6}\left(\frac{r}{r_a}\right)^2\sin 2\theta\\ &+\beta\sqrt{3}\left(2\left(\frac{r}{r_a}\right)^2-1\right)\\ &+\delta_1\sqrt{8}\left(3\left(\frac{r}{r_a}\right)^3-2\left(\frac{r}{r_a}\right)\right)\sin\theta+\delta_2\sqrt{8}\left(3\left(\frac{r}{r_a}\right)^3-2\left(\frac{r}{r_a}\right)\right)\cos\theta\\ &+\epsilon_1\sqrt{8}\left(\frac{r}{r_a}\right)^3\sin 3\theta+\epsilon_2\sqrt{8}\left(\frac{r}{r_a}\right)^3\cos 3\theta.\end{aligned}$$

The values of the polynomial coefficients in the above equation are found to be $S_0 = -0.0978$, $\alpha_1 = -0.0065$, $\alpha_2 = 0.0008$, $\beta = 0.0027$, $\delta_1 = 0.0053$, $\delta_2 = 0.0136$, $\epsilon_1 = -0.0021$, $\epsilon_2 = -0.0008$ for an NA of 0.384. The fitting results are summarized in Fig. 2.26. The dominant contribution comes from the spherical aberration. The fitting program can be found in Appx. B.

2.2.4 Top Imaging Calibration

We implemented this top imaging setup to our apparatus. The optics components and arrangement are shown in Fig. 2.27. Before the objective lens has been placed in the beam path, the probe laser beam is guaranteed to propagate rigorously along the holes on the optical table so that we can quickly estimate the total beam path length. The major challenge in the top imaging alignment comes from the large magnification. We could easily miss the image of our cloud on the camera if any one of the reflecting mirrors is not in the right angle. Plus we are not able to do the alignments on-the-fly due to the long duty cycle of the experiment. We did a step-by-step preliminary alignment with the probe beam first so as to stay close to the correct beam path as best as we can. These steps turned out to work great for us. Once everything has been set up on the table, it only took us a day or two to see some signal from the atoms, first in a 1D dipole trap, then in a crossed dipole trap.

- Optimize vertical dipole trap (VDT) beam alignment. The VDT beam co-propagates with

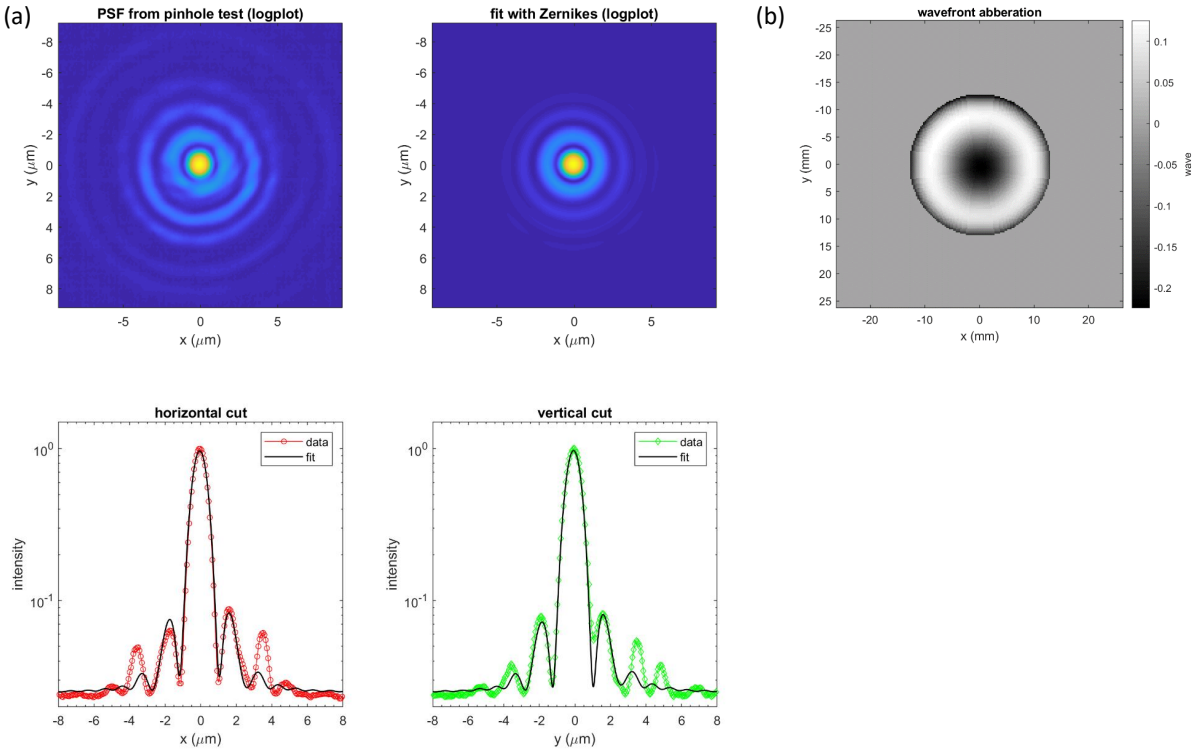

Figure 2.26: PSF fit with the wavefront distortion expanded in Zernike polynomials. (a) Top-left panel: measured PSF on log scale; top-right panel: fitting function with the first eight terms in Zernike polynomials; bottom panels: horizontal and vertical cuts through the center of the PSF on log scale to visualize the wiggles. (b) The wavefront distortion (i.e. the phase component of the exit pupil) determined from the PSF fit. In principle, a compensating phase plate with the same phase pattern but opposite amplitude can be used to completely suppress the aberrations.

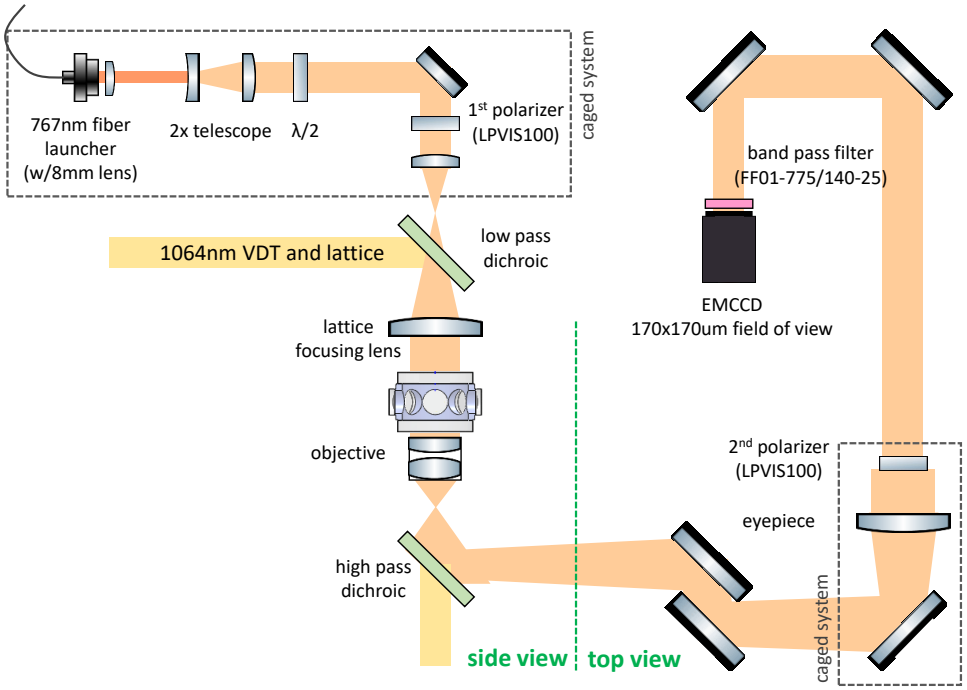

Figure 2.27: Optics layout for the top imaging setup on the science table. The distance between objective and eyepiece is set to equal $f_1 + f_2$.

the top probe beam in between the two dichroics therefore serves as a rough guidance. Note that our VDT beam is not perfectly perpendicular to the cell top/bottom windows for prevention of back-reflection.

- Collimate the top probe beam and overlap it on its back-reflection from the cell top window. Use a printed target to center the probe beam onto the window.

- Iris down the optical pumping (OP) beam to be about less than 1 mm. This OP beam travels through the same fiber as the top probe beam. We translate the OP beam while imaging the atoms from the side to make sure that the OP beam is hitting on the atoms and transferring them into the imaging spin state. The OP beam serves as a better guidance, although its beam size is still larger than the field of view of our objective lens, which is estimated to be about 0.1 mm in radius.

- Use the top probe/OP beam to align the optics downstream (e.g. dichroic, mirrors, eye-piece, camera). We also use an auxiliary diode laser (Thorlabs compact laser module) to propagate backwards from the camera as another guidance. This helps handle the extremely long and snaky beam path.

- The objective is inserted in the end. Three back-reflected beam spots can be observed, two small nearly-collimated ones and a large diverging one. They are from different optics surfaces in the objective. Centering them on top of each other fixes the tilting angles of the objective. Now the objective should be parallel with the cell top/bottom windows.

- We use a home-made lens tube adapter (see the inset of Fig. 2.24) to connect an iris to the back of the objective at a distance of around its focal length. We align the translation of the objective by closing down this aperture while observing the focused beam being isotropically cut in from the edge. This was the same method that we used when aligning the side imaging objective.

We also paid great attention to the polarization of the probe beam. On the output of the

caged fiber launcher, the extinction ratio of the polarization is better than $10^5 : 1$ (set by the film polarizer LPVIS100 from Thorlabs, damage threshold 1W/cm^2 continuous block, 5W/cm^2 continuous pass). Birefringence on cell windows, dichroics and mirrors reduces the extinction ratio to be $> 10^3 : 1$. This number should be sufficient for us to do non-demolition detections such as Faraday rotation imaging [47, 48, 49].

2.2.5 Science Camera Calibration

Our science camera for the top imaging is a Princeton Instruments ProEM 512B. The quantum efficiency of the CCD is around 77 % at 767 nm. We use the shot noise of dark frames to calibrate its noise level and ADC gain. As shown in Fig. 2.28 panel (a), we took two dark frames at different exposure times and extracted the mean dark counts from them. Assuming that all the pixels are equivalent, the standard deviation of the dark count per pixel is equal to the standard deviation of the two frames' difference divided by $\sqrt{2}$. Each frame contains a statistically large number of 512×512 pixels. In the short exposure time limit, the noise is dominated by the read noise. For long exposure times, we can extract the gain of the CCD from the shot noise on the dark current. In Fig. 2.28 panel (b), we fit the total noise per pixel into $\delta_{\text{total}} = \sqrt{\delta_{\text{cts}}^2 + \delta_{\text{read}}^2}$, and $\delta_{\text{cts}} = G\delta_{N_e} = G\sqrt{N_e}$, where G is the ADC gain. From this fit, the read noise turns out to be 7.3(8) cts. (counts, or *least significant bits*), and the gain is 0.98(4) cts. per electron. From the mean dark count in either frame, the bias reads 603 cts., and the dark current is estimated to be 33 cts. per pixel per second in the linear regime. The above measurements are taken at $-40\,^{\circ}\text{C}$, read out rate is 1 MHz and controller gain set to be 1.

2.3 Fast Magnetic Field Coils Setup

Our fast magnetic coils (named fast-B coils) are a pair of 11 turn coils made of 20 gauge magnetic wires. Each coil is 0.9" in inner radius and 1.0035" in outer radius. The inductance per coil is about 20-30 µH. The magnetic field from the fast-B coils is calibrated to be 2.25 G/A. So we need about 4.44 A current in order to generate a magnetic field change of 10 Gauss. This is enough

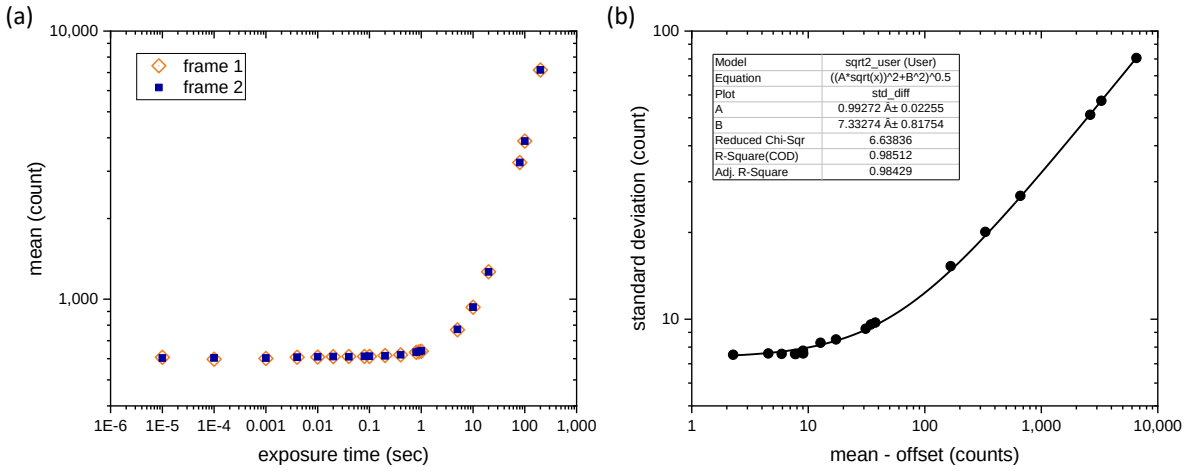

Figure 2.28: Calibration of top imaging camera. (a) Mean total dark current in count per pixel vs. camera exposure time. The total dark current consists of readout bias plus dark current. For each exposure time we took two frames with camera shutter closed. (b) Standard deviation of the dark count per pixel vs. mean dark count per pixel. The solid line shows a fitting function for the total dark noise which is the quadrature sum of read noise and shot noise.

for us to jump the scattering length of the atoms from $+200\,a_0$ (at 38 G) to $-200\,a_0$ (at 28 G). Note that the polarity of the fast-B coils is set to be opposite to that of the bias coils. The fast-B coils are air-cooled and in close proximity to the the science cell, hence any heating of the coils should be avoided. It is worth noting that due to the strong inductive couplings between the bias coils and fast-B coils (they are very similar in diameters as can be seen from Fig. 2.14 panel (a)), closing the loop of the fast-B coils can affect the bias feedback system if the proportional gain for the latter is aggressive. One should make sure the noise level of the bias current stays the same with and without the fast-B coils being present. For the bias field, we use Keithley multimeter to measure the voltage drop across the sensing resistor on the out-of-loop current transducer. By using fast mode on the multimeter, ppm level noise can be detected at a sampling rate of 10/PLC (power line cycle). For the fast-B field, we use a fast oscilloscope to calibrate the noise level on the out-of-loop Hall probe. The Hall probe is clamped onto the one of the current leads and placed 1 meter away from the coils. It is a quite sensitive device and prone to picking up noise from random sources.

2.3.1 Fast-B Servo and Setup

The fast-B feedback servo setup is shown in Fig. 2.29 with model numbers of individual components labeled on it. We employ the JILA coil drive designed by T. Brown, and a small resistor $0.25\,\Omega$ to sense the current. A clamp-on fast current probe is used for monitoring the current. For safety reason, the servo is first tuned up with a pair of test coils which are of the same dimensions as the fast-B coils. A fast-blow fuse is installed to break the loop after 0.5 seconds when the current exceeds 3 A. We also use the analog control of the fast-B coil power supply to gate its output. For a control voltage of 3.33 V, the power supply can output 100 V. The response time of the power supply to the analog signal is about 80 ms.

For tuning up the coil driver, we start off with all PID trimpots fully off. Then the gain and PI frequency are increased proportionally until oscillations in the current show up. The lead span and bandwidth are engaged in the end with the gain backed off and PI frequency increased when

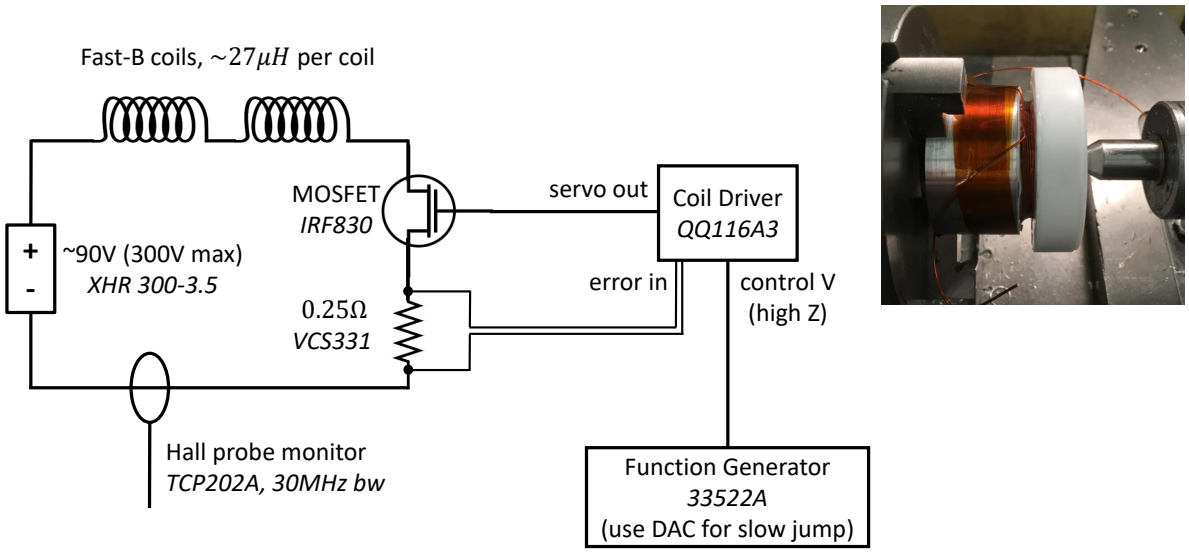

Figure 2.29: Schematic of the fast-B coils feedback servo setup. The inset photograph shows a test coil that we wound on a lathe.

necessary. The above adjustments are done iteratively in small steps. We are able to obtain a 10-90% rise time of about 3 µs on the fast-B current for a 10 Gauss field jump. The setpoint voltage is provided by an arbitrary function generator in this test. The results are shown by the scope traces in Fig. 2.30 panel (a)(b). We applied about 94 V to the coils so that the current changing rate is less limited by the coil inductance according to $V = -L\,(dI/dt)$. Due to the non-linearity of the MOSFET, a smaller jump distance requires a slightly different tuning of the servo. We also test the fast-B performance with a DAC line as the setpoint input as shown in Fig. 2.30 panel (c)(d). The DAC has a finite slew rate of about 1 V/µs. However, this does not seem to be limiting the fast-B current rise time in our case.

2.3.2 Compensation for Induced and Eddy Current

When the fast-B field is being changed very rapidly, it induces current in our bias coils and nearby metals. The induced current in bias coils oscillates at the resonance frequency which is determined by the coil inductance and also the bias coil power supply voltage. As presented in Fig. 2.31, the peak-peak amplitude of this oscillation amounts up to 1.5 G. And the damping time constant is about 120 µs. Since we do not trap atoms by magnetic field, the bias coils are the only ones that respond to the fast-B field change. The eddy current in our setup has a more minor effect on the total field. It curves the edge on the fast-B pulse and slows down its rise time from a few µs to about 200 µs.

We tried some RC snubbers on the bias coils but could not suppress the induced current oscillations very well. In the end as the fast-B field is pulsing on, we jump the bias current to a higher value (corresponding to a larger magnetic field and a smaller scattering length) at about 100 µs prior to the fast-B leading edge. As shown in Fig. 2.32 panel (a), this jump on bias coils generates a current oscillation with an opposite phase and exactly the same amplitude as the induced current from the fast-B pulse, therefore the two effects cancel each other. With the induced current on bias coils being removed, we can visualize the eddy current effect as presented by the rf spectroscopy in Fig. 2.32 panel (b) (black circles). This eddy current is fairly smooth therefore can be easily fixed

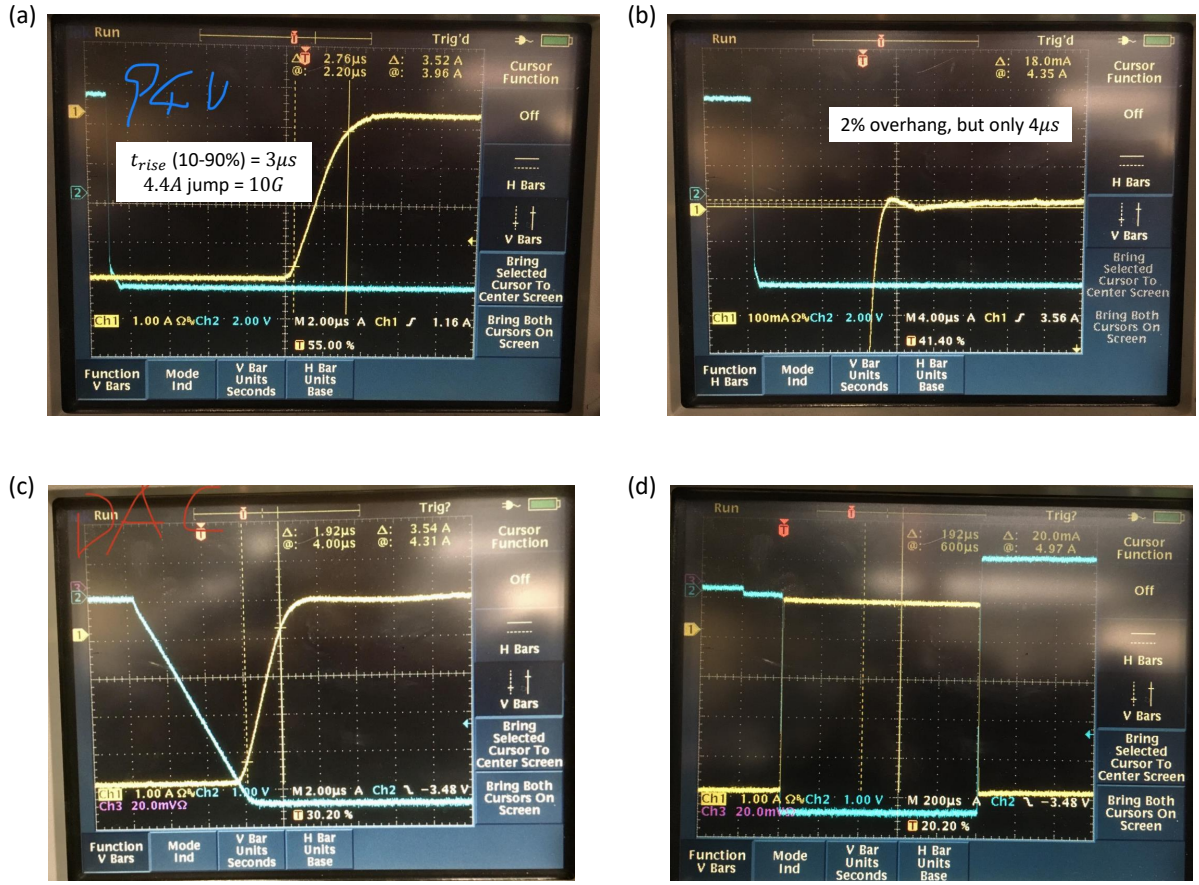

Figure 2.30: Tuning up the fast-B coils feedback servo. Blue traces: setpoint signal; yellow traces: clamp-on hall probe monitor. (a) The 10-90% rise time of the current is measured to be about 3 µs for a 10 Gauss jump. We use 94 V on the power supply for the coils. We use extremely low duty cycles ($< 0.5\%$) on the function generator that gives the set voltage when tuning this servo in order to minimize the heating. (b) Zooming in on the small overshoot of the current. Note that the delay between the setpoint and the actual current can be removed by pre-turning on the MOSFET gate with a small set voltage like -10 mV. (c) Use a DAC line as the set voltage instead of the arbitrary function generator. The rise time of the fast-B current is minimally affected by the finite slew rate of the FPGA DAC line. (d) The full fast-B pulse of about 1 ms duration. A small pre- and post-pulse positive setpoint completely shuts off the fast-B current to prevent it from oscillating at such high power supply voltage.

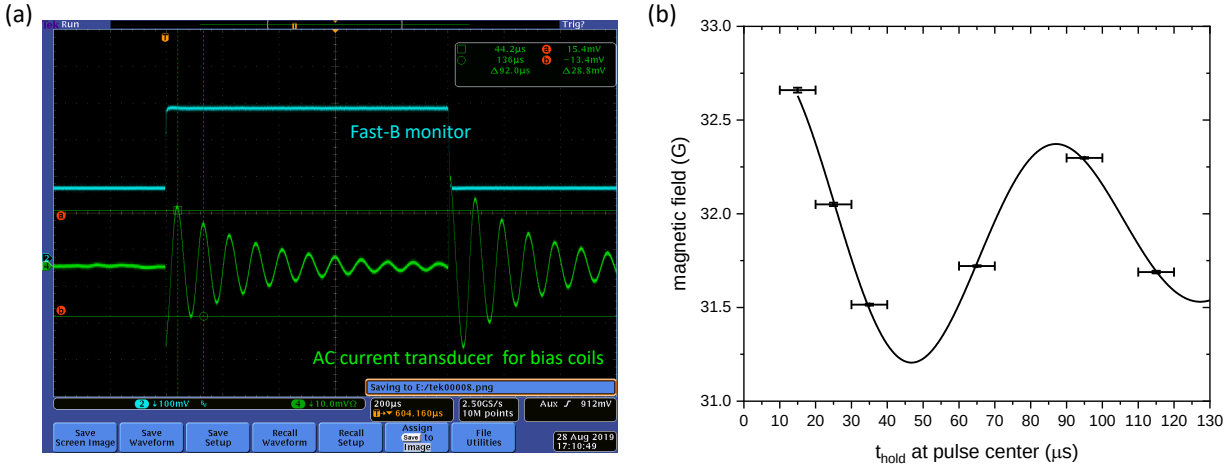

Figure 2.31: Induced current in bias coils due to a fast-B field jump of 8 G. (a) Induced current measured on an out-of-loop AC wide-band current transducer (Pearson Electronics, Inc). (b) The actual magnetic field calibrated with rf spectroscopy. The horizontal error bars represent the pulse width of the microwave for a hyperfine transition. The solid line is a fit with damped sine function. Note that the two different detection methods are consistent in the oscillation period and amplitude, which indicates that the bias coils are the only source of this induced current since the mechanical relays on all other coils are open at this moment.

by feeding-forward to the setpoint on the fast-B field. The data in Fig. 2.32 panel (b) show one such example in which we overshoot the fast-B setpoint by about 1 G and then ramp it back to the target field by two 100 µs steps. Some iterations of this optimization process might be needed if one desires a even more fine control of the scattering length especially at short hold times.

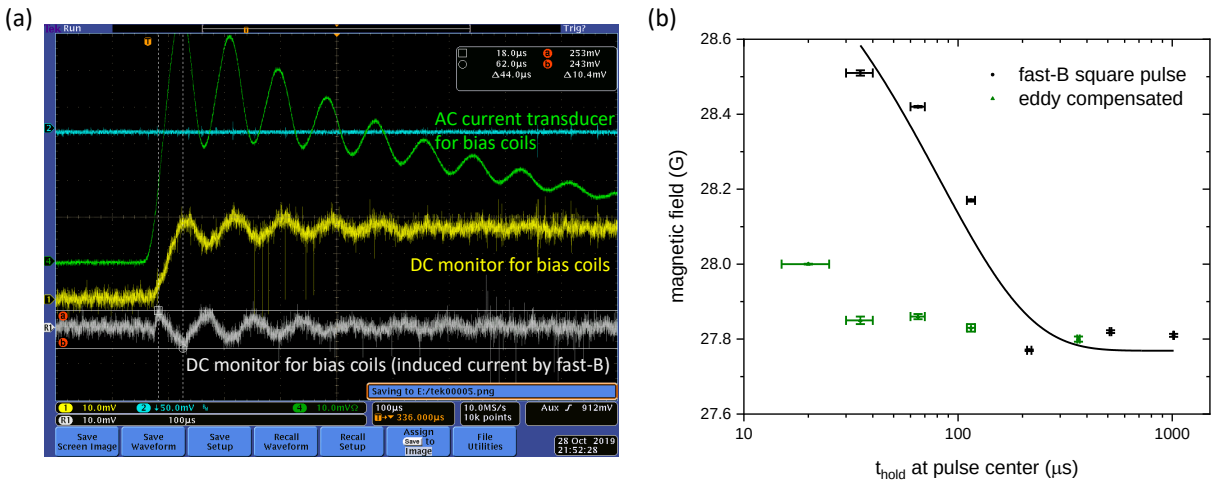

Figure 2.32: Compensating the induced current and eddy current caused by the fast-B field jump. (a) The current wiggles on bias coils induced by a fast-B rapid change (yellow trace) can be canceled out by jumping the bias coil current (gray trace) with an opposite phase and a properly-adjusted amplitude. Note that the noise on the bias current is mainly from the picked-up signal along the long BNC cable on this out-of-loop monitor. (b) Black circles: by canceling out the induced current in bias coils, we can see the eddy current effect that manifests as the corner of the square pulse being smoothed over. The solid line indicates a fit with exponential function. Green triangles: by "overshooting" the setpoint on the fast-B field by about 1 G and slowly ramp it back we can remove most of this eddy current.

Chapter 3

Efimov Physics: A Brief Review

Comprehensive discussions on Efimov physics can be found in review papers such as [50, 51, 52, 53]. In this thesis, I focus on some fundamental aspects of the research highlights in this field, including both experimental and theoretical works.

3.1 From Two to Three

3.1.1 Two-Particle Scattering in Zero-Energy Limit

In ultra-cold scattering theories, a *channel* can be specified by the spin quantum numbers of the two colliding atoms, e.g. $\alpha = \{f_1 m_{f_1} f_2 m_{f_2} l m_l\}$, where l and m_l specify the angular momentum of the collision [1] . A channel is referred to as "open" when the asymptotic channel energy $E_\alpha = E_{f_1 m_{f_1}} + E_{f_2 m_{f_2}}$ is lower than the system total energy E; and "closed" if otherwise. The scattering potentials for different channels are shifted with respect to each other due to the Zeeman effect. In the two-channel picture of a magnetic Fano-Feshbach resonance (FR), a pair of atoms in the open channel (or entrance channel) are coupled to a shallow bound state in the closed channel via virtual spin-exchange process. As shown in Fig. 3.1 panel (a), the energy difference between the two channels can be conveniently tuned by an external magnetic field. As a result, the near degeneracy between the scattering state and shallow bound state leads to a scattering resonance in the s-wave scattering length a_s as shown in Fig. 3.1 panel (b). In the zero collision energy limit,

[1] We closely follow the notations introduced in [54] in this section.

a_s can be parameterized as

$$a_s(B) = a_{\rm bg}\left(1 - \frac{\Delta}{B - B_0}\right), \tag{3.1}$$

where Δ represents the width of the FR in units of Gauss. The $a > 0$ and $a < 0$ regions correspond to effectively repulsive and attractive interactions between atoms. Scattering processes in general are contributed by the background scattering (the first term in Eqn. 3.1, given by $a_{\rm bg}$ which in most cases is on the order of $r_{\rm vdW}$) plus the resonant part (the second term in Eqn. 3.1).

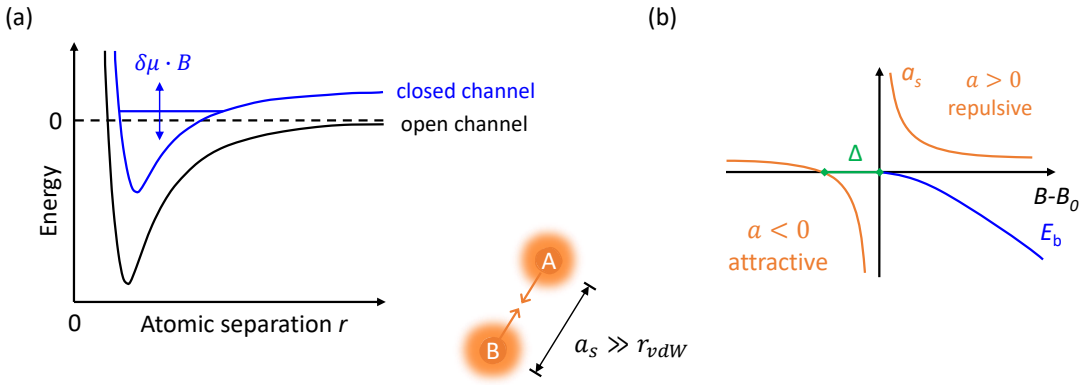

Figure 3.1: (a) Two-channel model of Feshbach resonances, and (b) the s-wave scattering length a_s as a function of magnetic field B. The cartoon picture shows that the delocalized wave packets of two atoms interact with each other at a distance of a_s which can be much longer than $r_{\rm vdW}$ in the vicinity of a Feshbach resonance.

The shallow bound state in dressed state picture becomes the Feshbach molecule and its binding energy is E_b. The wavefunction of a Feshbach molecule can be expressed as a superposition of the bare bound state and the background scattering state as

$$|\psi_b\rangle = \sqrt{Z}\phi_c|{\rm c}\rangle + \chi_{\rm bg}|{\rm bg}\rangle, \tag{3.2}$$

where $Z \in [0, 1]$ indicates the weight of the closed-channel component and depends on the magnetic field detuning $(B - B_0)$. Both Z and E_b vanish in the limit of $B \to B_0$.

One important parameter that characterizes the strength of the coupling between the open

and closed channels is $s_{\rm res}$. In a field theory formalism, $s_{\rm res}$ can be defined as

$$s_{\rm res} = \frac{\bar{a}}{r^*}, \tag{3.3}$$

where $\bar{a} \approx 0.956\, r_{\rm vdW}$ and r_* is sometimes called the range of the FR [55]. For ^{39}K, $r_{\rm vdW} = \frac{1}{2}\left(mC_6/\hbar^2\right)^{\frac{1}{4}} = 64.61\, a_0$. We can relate r^* to the coupling amplitude g between the atomic and molecular field through $g^2 = 32\pi/r^*$ and determine its value by matching the experimentally measured profile $a_s(B)$. Another equivalent approach to calculate $s_{\rm res}$ is to use

$$s_{\rm res} = \frac{a_{\rm bg}\Delta}{\bar{a}}\frac{\delta\mu}{\bar{E}}, \tag{3.4}$$

where $\delta\mu$ stands for the differential magnetic moment between the open and closed channel, and $\bar{E} = \hbar^2/(m\bar{a}^2)$ is the energy scale associated with the van der Waals force. Feshbach resonances with $s_{\rm res} \gg 1$ ($\ll 1$) are termed *entrance- (closed-) channel dominated resonances* in that the near-threshold scattering and bound states have the spin character of the open channel over a large (small) fraction of the width Δ. Open-channel dominated resonances have been widely studied with ^{133}Cs and ^{85}Rb, etc. A single-channel approximation is sometimes sufficient in the case of ^{133}Cs. While closed-channel dominated resonances are relatively trickier to access due to their narrow widths Δ. A multi-channel description is usually needed to model such resonances.

In ^{39}K, a number of FRs are of intermediate coupling strengths. The FRs on all three $F = 1$ spin states at low magnetic field are plotted in Fig. 3.2. We focus on the $|F = 1, m_F = -1\rangle$ spin-polarized gas (called *cc* channel) in this thesis. The shallow bound states associated with this scattering channel are shown in Fig. 3.3. For the FR at 33.5820 G, five different spin configurations need to be involved in a full coupled-channel calculation. As shown in Fig. 3.4, the relative hyperfine energies of these channels are plotted with respect to the mean energy value. The fraction of each channel in the Feshbach molecule state is also plotted in order to visualize their weights as a function of magnetic field. All above calculations are done by P. S. Julienne, *et al.*

Although the strength parameter $s_{\rm res}$ is originally introduced for a two-channel model, we can define a multi-channel analogy of it for our FR in ^{39}K. As depicted in Fig. 3.6 and discussed

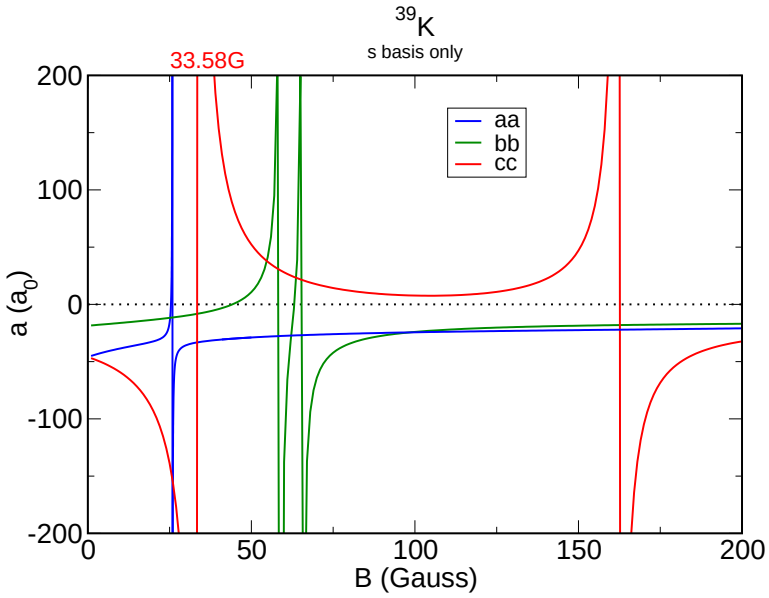

Figure 3.2: Feshbach resonances in ^{39}K for the $F = 1$ spin-polarized gases, $0 - 200$ G, s-wave basis; $a \to |F = 1, m_F = +1\rangle$, $b \to |F = 1, m_F = 0\rangle$, $c \to |F = 1, m_F = -1\rangle$. The FR we focus on is the one at 33.5820 G in the cc channel (red lines). (Fig. 3.2 to 3.5 are all generated by P. S. Julienne.)

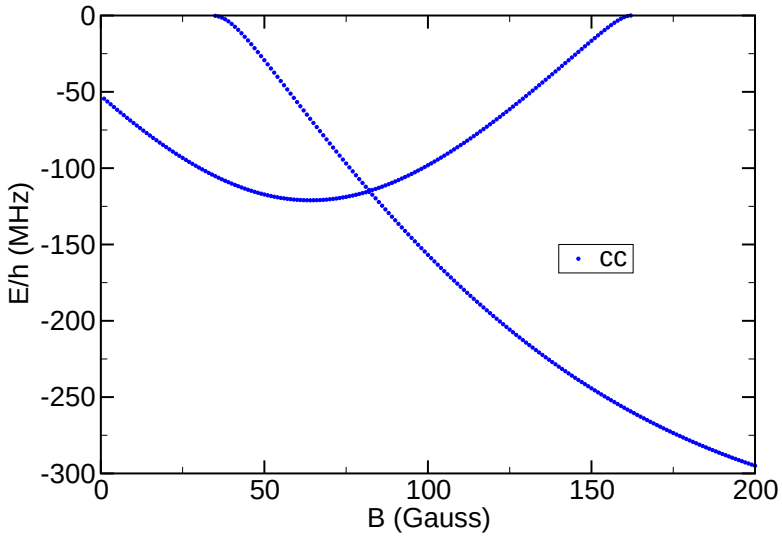

Figure 3.3: Two shallowest bound states in ^{39}K for the cc channel, $0 - 200$ G, which are associated with the two FRs at 33.5820 G and 162.34 G respectively.

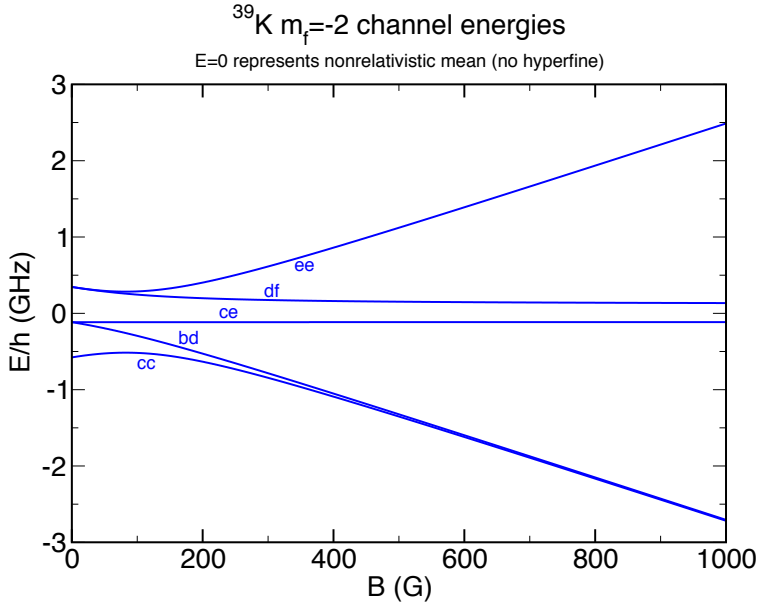

Figure 3.4: Hyperfine energies of the five spin configurations in the multi-channel model for ^{39}K, total $m_F = -2$, $0 - 1000\,\mathrm{G}$; $b \to |F = 1, m_F = 0\rangle$, $c \to |F = 1, m_F = -1\rangle$, $d \to |F = 2, m_F = -2\rangle$, $e \to |F = 2, m_F = -1\rangle$, $f \to |F = 2, m_F = 0\rangle$.

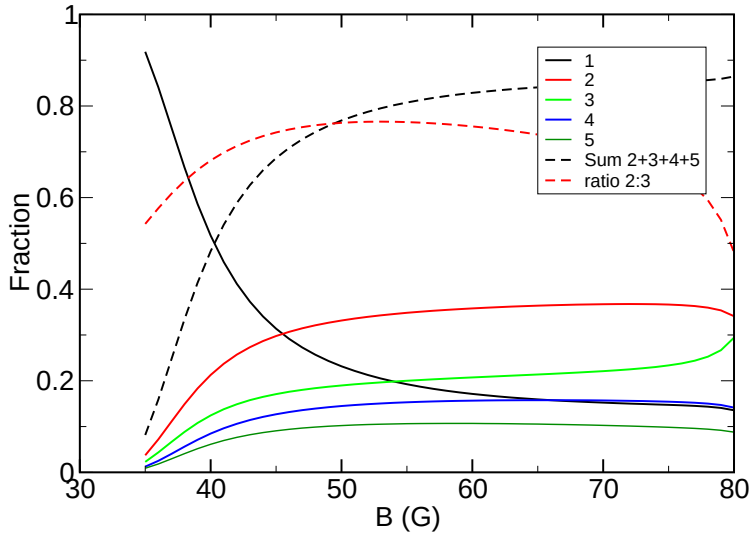

Figure 3.5: Fraction of each channel in Feshbach molecule as a function of magnetic field, $30 - 80\,\mathrm{G}$; $1 \to$ cc, $2 \to$ bd, $3 \to$ ce, $4 \to$ df, $5 \to$ ee. The *cc* entrance channel plays a predominant role near the pole of the resonance at 33.5820 G.

in [18], the dashed lines indicate the magnetic moments of two free atoms and the bare bound state in their linear regimes respectively. The differential magnetic moment is calculated to be $\delta\mu/h \approx 3.43\,\mathrm{MHz/G}$. The value of s_{res} is determined to be about 2.45 in this approach.

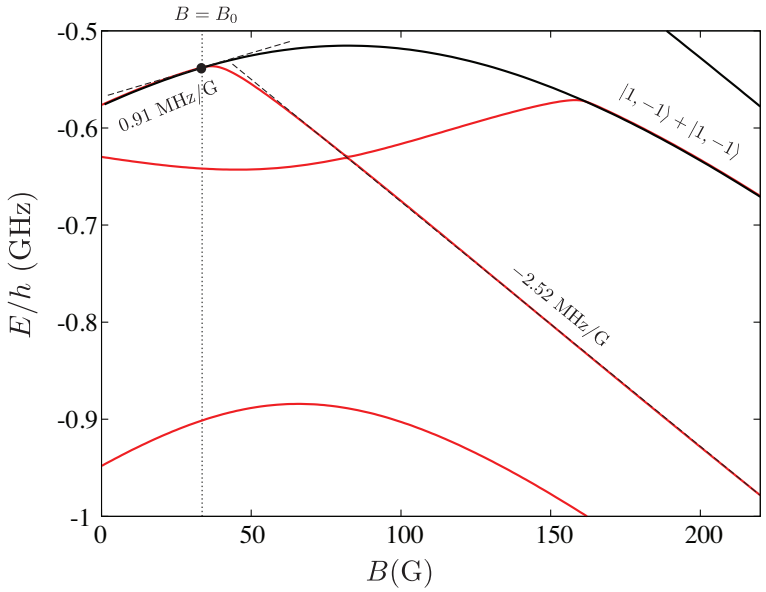

Figure 3.6: Atomic energy (solid black line) and coupled-channel calculation of bound state energies (red lines) near threshold for ^{39}K, $0 - 220\,\mathrm{G}$. The figure is borrowed from [18]. The dashed lines represent the atomic and molecular magnetic moments near and away from B_0 respectively. Their difference is $\delta\mu/h \approx 3.43\,\mathrm{MHz/G}$.

3.1.2 Finite-Energy Effects and Effective Range

For incoming atoms of finite momenta $\pm\mathbf{k}$ in the center of mass frame, the low-energy expansion of the scattering amplitude can be expressed in effective range approximation

$$f(k) = \frac{1}{-1/a + r_e k^2/2 - ik}. \tag{3.5}$$

The effective range r_e is another useful parameter which accounts for the finite energy effects up to order k^2. For a two-channel model, it is a function of magnetic field

$$r_e(B) = -2r^* \left(1 - \frac{a_{\mathrm{bg}}}{a(B)}\right)^2 + r_e^{(1)}, \tag{3.6}$$

where

$$r_e^{(1)}(a) = \frac{\Gamma(\frac{1}{4})^4}{6\pi^2}\bar{a}\left(1 - 2\frac{\bar{a}}{a} + \left(\frac{\bar{a}}{a}\right)^2\right) \tag{3.7}$$

is the single-channel approximation for large $s_{\rm res}$ values (see supplemental materials of [18]). The full function of r_e Eqn. 3.6 is plotted in Fig. 3.7 for various a. As $a \to \infty$, $r_e(B_0) = -2\bar{a}/s_{\rm res} + 2.91791\bar{a}$. For $s_{\rm res} \gg 1$, $r_e \to 3\bar{a}$; for $s_{\rm res} \ll 1$, $r_e \to -2r^*$; at $s_{\rm res} \approx 1$, r_e crosses zero as a result of continuity. Although the exact crossing point is model-dependent [56], this behavior implies a suppressed role of finite range in scattering and bound state problems.

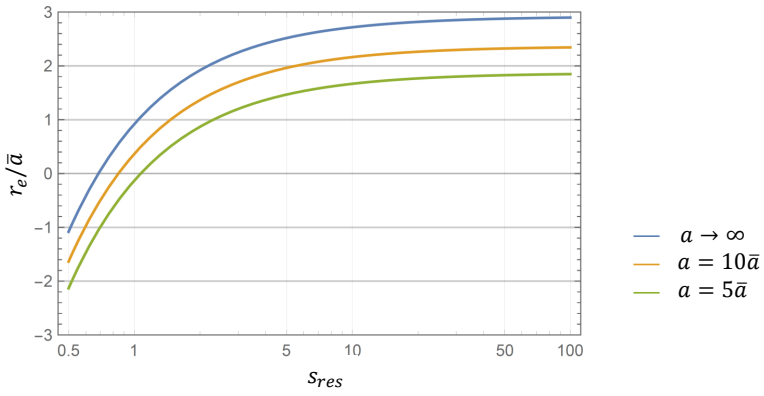

Figure 3.7: Effective range as a function of $s_{\rm res}$ evaluated at three different values of a. $a_{\rm bg}$ is set to 0 in this plot to represent species such as ^{39}K and ^{7}Li.

A physical interpretation of the change of sign in r_e can be found in E. P. Wigner's old concept of time delay in two-body scattering [57]). As depicted in Fig. 1 of [58], the s-wave phase shift at finite wave vector leads to a spatial shift Δr which is equal to r_e according to

$$\delta_0(k) = \frac{\pi}{2} - \frac{r_e k}{2} + \ldots \quad \Rightarrow \quad \Delta r = -2\frac{d\delta}{dk} = r_e + \ldots \tag{3.8}$$

at $a \to \infty$. The scattered wavepacket from far field appears as if it originates at Δr rather than $r = 0$. For open-channel dominated resonances, the situation is the same as in as single channel potential with a van der Waals tail, where $\Delta r \simeq 3\bar{a}$. In this case the particles can not get closer to the origin (in the center-of-mass frame) than about $3\,\bar{a}$. The situation is completely different for

closed-channel dominated resonances, where the two colliding particles form an intermediate bound state. The associated long time delay translates into a negative value of Δr, i.e. the scattered wave appears to come from negative relative distances.

A coupled-channel result on r_e as a function of B for ^{39}K cc channel is shown in Fig. 3.8 and compared to a single-channel calculation. By matching Eqn. 3.6 to the coupled-channel model, we arrive at $s_{\rm res} = 2.68$ which is consistent with the alternative approach given in 3.1.1.

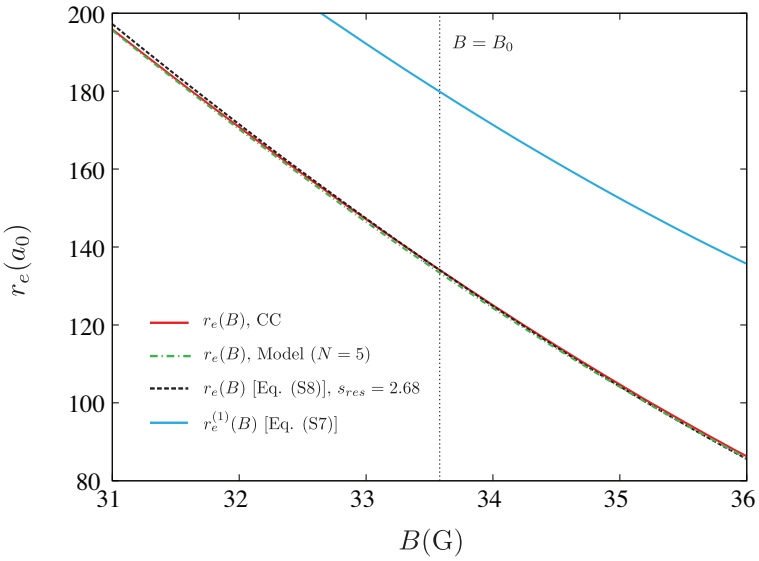

Figure 3.8: A full coupled-channel calculation of r_e for ^{39}K (red line) near the pole $B = B_0$. The figure is borrowed from [18]. The cyan line is single-channel formula Eqn. 3.7.

3.1.3 A Pedagogical Illustration of Three-Particle Scattering

For three particles located at $\vec{x}_1$, $\vec{x}_2$ and $\vec{x}_3$, eliminating the center of mass, the system can be described in *Jacobi coordinates*:

$$\vec{r}_{ij} = \vec{x}_j - \vec{x}_i, \quad \vec{\rho}_{ij,k} = \frac{2}{\sqrt{3}}\left(\vec{x}_k - \frac{\vec{x}_i + \vec{x}_j}{2}\right) \tag{3.9}$$

where (i, j, k) are chosen among $(1, 2, 3)$. Three-body problems can be greatly simplified by doing a frame transformation into the so-called *hyper-spherical coordinates*:

$$r = R\sin\alpha, \quad \rho = R\cos\alpha \tag{3.10}$$

where $R = \sqrt{r^2 + \rho^2}$ is the hyper-radius that sets the overall spatial extent of the system, and $\alpha = \arctan(r/\rho) \in [-\pi/2, \pi/2]$ is the Delves hyper-angle. In this representation, the motions of three or more particles can be quasi-separated into hyper-radial and hyper-angular wavefunctions.

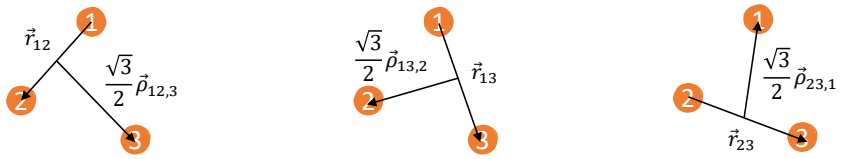

Figure 3.9: Jacobi coordinates describing the relative positions of three identical particles.

In 1970, V. Efimov discovered an effective long-range attractive interaction in three-particle systems with short-range inter-particle interaction near a scattering resonance [59, 60]. In the near-resonance condition, the details of the interactions can be ignored as the scattering length a_s sets the only length scale in two-particle scattering processes. Efimov proved that with two-body resonant interactions, the ground potential of three-body hyper-radial motion has an effective attraction of the form

$$V_0(R) = -\frac{|s_0|^2 + 1/4}{R^2}, \tag{3.11}$$

where s_0 is a constant that depends on the mass ratio. For three identical bosons, $s_0 \approx 1.00624$. Heuristically, the long-range interaction arises from two particles interacting with each other at a long distance by effectively exchanging the third one [52]. The idea is shown by the cartoon in Fig. 3.10 panel (a). This process becomes clearer in the Born–Oppenheimer picture (e.g. covalent bond between atoms) especially for mass-imbalanced systems with two heavy particles and one light particle, in which the Efimov effect is in fact strengthened (i.e. featured by larger $|s_0|$ values). The effective long-range attraction is sometimes said to be of kinetic origin since it happens with the aid of low-energy diffused wave packets as its media [61].

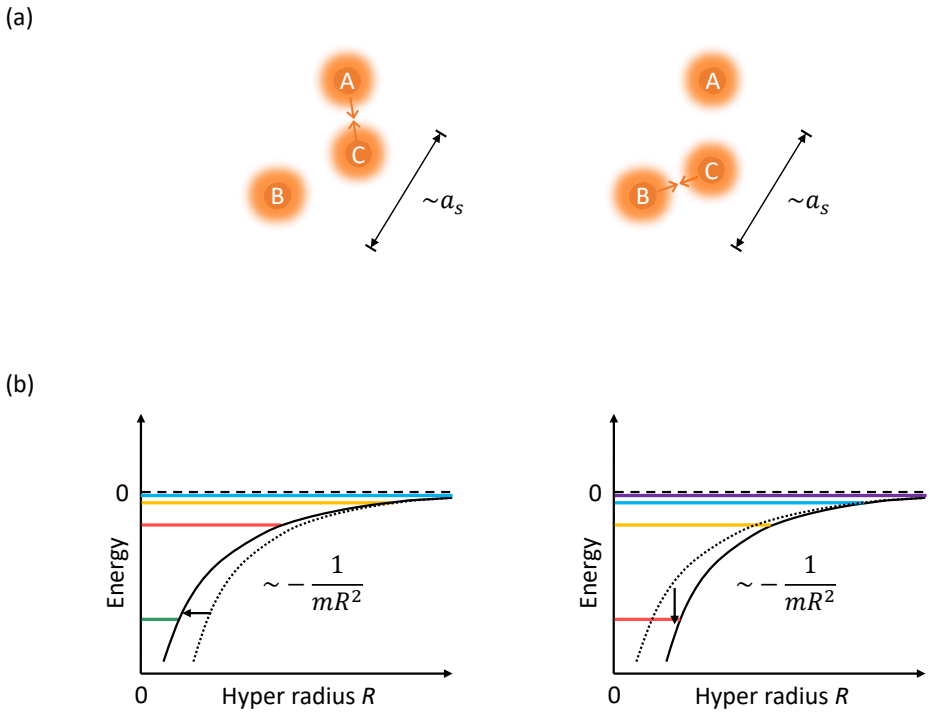

Figure 3.10: Efimov attraction and scaling invariance. (a) Effective long-range interaction arises in a three-particle system in which each pair of atoms are resonantly interacting. Particle A and B can interact at a long distance by exchanging a "fast" particle C. Note that real particles are indistinguishable bosons in homonuclear case. (b) A sketch of this long-range attraction as a function of hyper-radius R. Dragging the potential from the dashed black line to solid black line accomplishes a scaling transformation on R. The bound states which are indicated by the colored solid lines remain in the same place after this transformation.

A consequence of this effective long-range attraction is *scale invariance*. A $\propto 1/R^2$ form of potential energy scales as the kinetic energy $\propto d^2/dR^2$ under scaling transformation $R \to \lambda R$. As a result, the quantized bound state spectrum in a potential such as the one give by Eqn. 3.11 displays *discrete scale invariance* with a scaling factor of $e^{2\pi/|s_0|}$. Namely, an infinite number of three-body bound states form a geometric series of energies accumulating at the threshold at unitarity. This scaling invariant spectrum associated with the effective long range potential is qualitatively explained in Fig. 3.10 panel (b). Only three of the infinite number of bound states are drawn in the picture.

Remarkably, Efimov has shown that this discrete scale invariance can be extended to finite scattering lengths. The bound state spectrum can be plotted in a two dimensional space of $1/a$ and κ, where κ is the wave number of the bound state. A sketch of this well-known Efimov's scenario can be found in Fig. 3.11 panel (a). On the $a > 0$ side, the trimer states co-exist with the Feshbach dimer state. On the $a < 0$ side, the trimers can stay bound even when the inter-particle potential is not strong enough to support a two-body bound state. This is the so-called *Borromean state*. For three identical bosons, the scaling factor between adjacent trimer states in this $(1/a, \kappa)$ basis is $e^{\pi/|s_0|} \approx 22.7$. Efimov spectrum is famous for its self-similarity appearance. Familiar examples of self-similarity (or fractality) include the Matryoshka dolls and Romanesco broccoli as shown in Fig. 3.11 panel (b).

3.2 Universality in Efimov Physics

3.2.1 Observation through Loss

In his original work, Efimov considered nuclear systems such as triton (the nucleus of tritium ^{3}H), and the Hoyle state of ^{12}C (three α particles). Yet these nuclear systems do not fully satisfy the short-range interaction condition due to the presence of competing Coulomb repulsion in these systems. Neutral atoms, more than thirty years after Efimov proposed his ideas, have become a novel and ideal platform for the study of Efimov physics by virtue of an adjustable interaction

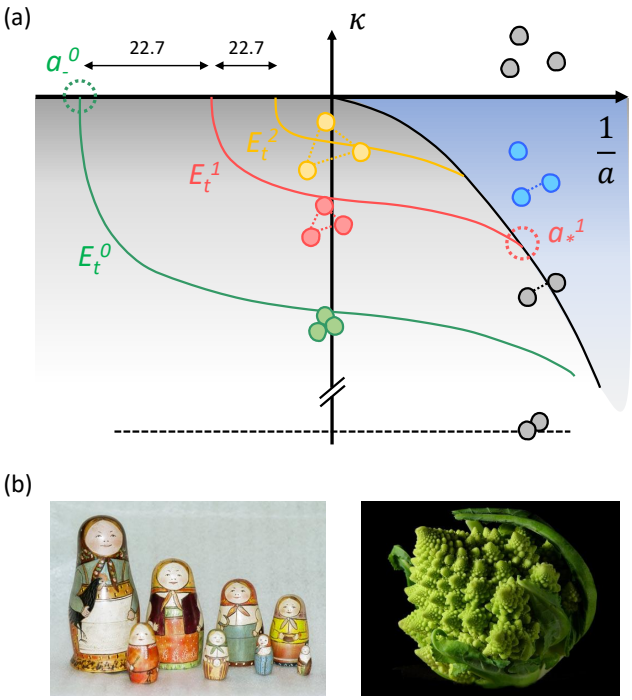

Figure 3.11: (a) Schematic plot of Efimov spectrum as function of $1/a$ in unit of wave number κ. The area above the x-axis indicates three-free-atom continuum. The blue shaded area indicates two-atom bound state plus a free atom. The gray shaded area indicates three-atom bound states. Three trimer states are drawn in colored solid lines with an artificially reduced scaling factor. They emerge at the three-atom threshold for $a < 0$ and connect to the atom-dimer threshold for $a > 0$. An infinite number of trimer states that accumulated at the resonance pole are omitted. A two-body potential in realistic systems also supports deeply bound dimer states whose binding energies are on the order of $\hbar^2/(mr_{\mathrm{vdW}}^2)$ and beyond. Those dimers are indicated conceptually as the dashed line near the bottom of the plot. (b) Nesting dolls and broccoli, two other examples that also present self-similar feature. Pictures are clipped from *Wikipedia*.

strength in the vicinity of a Feshbach resonance.

In contrast to ^{4}He for which the interaction potential only hosts one dimer state, potentials for alkali metals are deep enough to support a large number of ro-vibrational states whose binding energies are on the order of van der Waals energy $\hbar^2/(mr_{\mathrm{vdW}}^2)$ and beyond. An Efimov trimer in alkali metals is more of a quasi-bound state (i.e. resonances embedded in the continua formed by one atom and one diatomic molecule) and can dissociate into a deeply bound dimer plus a free atom. This process leads to a very limited lifetime of the Efimov trimers and disfavors direct observations of the trimers by spectroscopic methods. Due to this reason, Efimov trimers are usually detected through enhanced losses of the atoms (e.g. three-body recombination). As encircled by the dotted lines in Fig. 3.11 (a), a trimer state intersects the free-atom threshold ($a < 0$) and atom-dimer threshold ($a > 0$) at certain a's. The trimers at these locations can greatly enhance the losses by acting as intermediate decay products [62] and manifest as resonance-like peaks in the loss rate.

One such feature, the tri-atomic resonance at $a = a_-^{(0)}$, occurs where the ground trimer state crosses the free atom threshold. It is first measured in ^{133}Cs and later has been repeated with other atomic species [63]. Although it is quite difficult to access higher order trimer branches in order to verify the scaling invariance aspect of the Efimov spectrum, it is still convincing that this loss enhancement is linked to Efimov physics because of the Borromean nature of the trimer state. Physically $a_-^{(0)}$ sets the smallest size of the Efimov series for $a < 0$. This parameter in fact is a missing piece of information in the Efimov physics based on zero-range theories. As has been shown by L. H. Thomas, a zero-range potential can lead to three-body bound states with arbitrarily large binding energies therefore a lower-bound for the interaction range has to be introduced. The experimentally determined $a_-^{(0)}$ provides such a lower-bound. It had been long anticipated to be unknown *a priori* due to its close relationship with the details of the inter-particle forces at short distances [64].

3.2.2 Van der Waals Universality

Three-body observables such as the above mentioned loss enhancements are associated with the short-range boundary condition that regularizes the zero-range theory of three particles. It is sometimes termed three-body parameter or "3BP" as a shorthand. This boundary condition in general depends on the detailed form of the short-range potential, in analogy to the two-body case. For instance we know that for an attractive potential with a deep well, the scattering wavefunction accumulates a large phase inside the well and a minute change in the potential can modify the scattering length drastically. The difficulty in predicting the 3BP for three-body attractive potentials can be understood in an analogous way. Generic three-body potentials for neutral atoms can be written in terms of a pairwise sum of van der Waals interaction, plus genuine non-additive three-body forces such as Axilrod-Teller interaction [53].

The discovery of *van der Waals universality* shed the first light on the 3BP problem. Experimental groups measured a constant value of $a_{-}^{(0)}$ in ^{133}Cs after sampling a series of FRs that are located at from a few Gauss to over 800 Gauss [12]. This experimental result suggests that the three-body short-range physics is not substantially altered by the absolute value of the magnetic field. Extensive experimental evidence later on confirms that $a_{-}^{(0)}$ is often about 9 times r_{vdW} regardless of the atomic species being used (see Fig. 21 in [52] for a summary plot). The microscopic mechanism of this universal location is revealed by a numerical calculation done in hyper-spherical coordinates. Wang *et al* found that the ground hyper-radial potential exhibits a steep repulsive barrier at a hyper-radius $R \approx 2\, r_{\mathrm{vdW}}$ instead of a strong attraction as one would naively expect from van der Waals potentials [13]. This repulsive barrier prevents the hyper-radial wavefunction from penetrating into the short-range part of the hyper-spherical potential where the situation becomes more species specific. They also proved that this effective three-body repulsion arises from the acceleration of the two-body relative motion due to the attractive van der Waals potential. This acceleration makes the two atoms spend little time at short separations and equivalently leads to a suppression of the two-body probability. As a consequence, a deformation of the three-body system

takes place as it changes from its configuration at large separations to that at small hyper-radii. At larger hyper-radius, the most probable configurations of hyper-angular wavefunction have an elongated-triangle geometry. While at smaller hyper-radii on the order of r_{vdW}, the suppression of two-body probability forces the system to adopt an equilateral configuration. This deformation of the three-body system gives rise to an increase of the kinetic energy cost and manifests as a repulsive barrier in the ground hyper-radial potential. An illustration of this change in three-body geometry can be found in Fig. 22 of [52]. Briefly, the van der Waals universality in 3BP has its origin in the two-body van der Waals universality in the $r > r_{\mathrm{vdW}}$ region, because the two-body radial probability density is suppressed in the $r < r_{\mathrm{vdW}}$ region as if there were a repulsive core in the potential.

The above conceptual explanation is based on a single-channel van der Waals potential. This is a good approximation near Feshbach resonances characterized by $s_{\mathrm{res}} \gg 1$. One would expect deviations from this theory when multiple channels are coupled by hyperfine interaction and participate in the scattering processes together. ^{39}K is such a species with an intermediate s_{res} value. Indeed, in our lab we made the first definitive observation of a deviation from vdW universality among homonuclear systems [18]. A compilation of all experimental values are presented in Fig. 3.12. The gray band indicates the prediction of single-channel vdW universal value $a_{-}^{(0)}/r_{\mathrm{vdW}} = -9.73 \pm 15\%$. The uncertainty is determined by the variance of details of the potentials used in individual theories. For the FR at 33.5820 G in ^{39}K, we experimentally nailed down the value of $a_{-}^{(0)}$ to be $-14.05(17) r_{\mathrm{vdW}}$ with unprecedented precision. Our result has been reproduced by a coupled-channel three-body model done by J. P. D'Incao with relatively good agreement. In this model, we incorporate realistic spinor physics that we learned from our Feshbach resonance calibration project.

3.2.3 Zero-Range Universality

Single-channel van der Waals universality is unique to the interaction potential of a $1/r^6$ form between two neutral atoms. In the original, more general version of Efimov physics, discrete

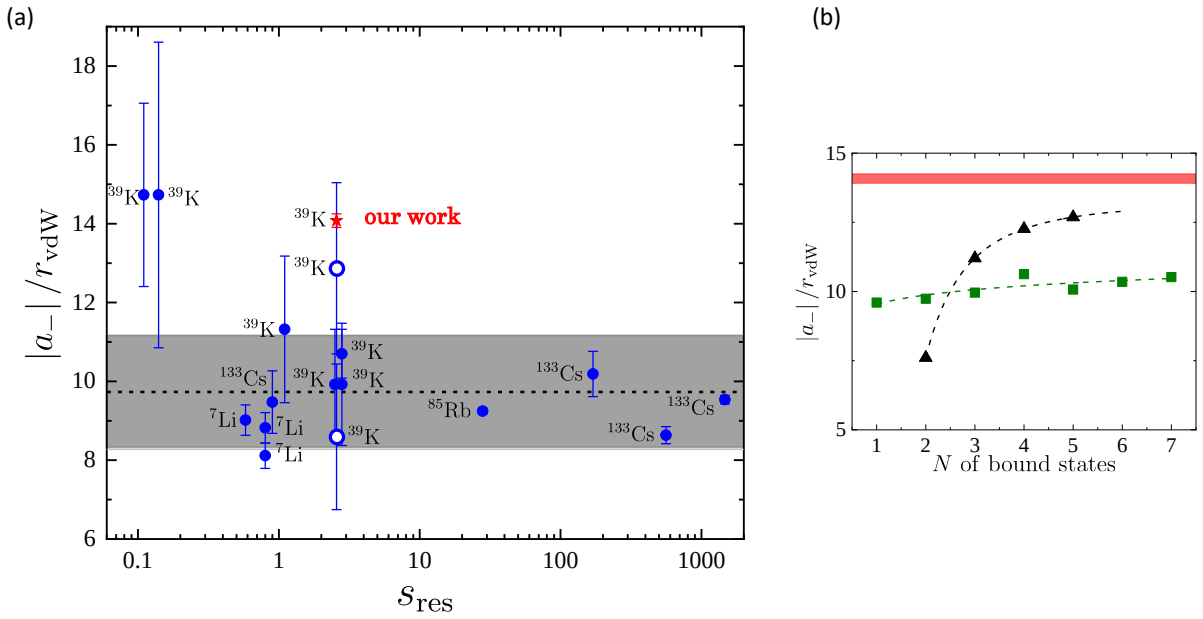

Figure 3.12: (a) A summary of experimentally determined values of $a_-^{(0)}$ in homonuclear systems as function of $s_{\rm res}$. ^{7}Li: Rice University, Bar-Ilan University, ENS; ^{39}K: LENS, Aarhus University, JILA; ^{85}Rb: JILA; ^{133}Cs: University of Innsbruck. The red star indicates our reported value of $a_-^{(0)}$ for ^{39}K. The open blue circles indicate previous results on the same $a_-^{(0)}$. The dashed line and gray band represent the range of van der Waals universality prediction. (b) Numerical calculations of $a_-^{(0)}$ based on a single van der Waals potential (green squares) and a multi-channel model (black triangles). N represents the number of s-wave diatomic bound states in the model. The red band indicates our experimental value. Both figures are cited from [18].

scaling invariance and a universal shape of the trimer levels in the $(1/a, E)$ plane are the two central results of a zero-range theory. In this *zero-range universality* framework, single-channel vdW universality plays the role of finite-range corrections to the low-lying trimers on the Efimov spectrum. In other words, the benefit of knowing the lower bound of the spectrum comes at the cost of severe distortions to the ground and first excited trimer energies $E_t^{(n)}$ $(n = 0, 1)$. This also shifts the corresponding locations of the scattering resonances where these trimers meet the scattering continua (e.g. $a_-^{(0)}$ and $a_*^{(1)}$), as well as the ratios between these locations (e.g. $a_*^{(1)}/a_-^{(0)}$). It is worth noting that the Feshbach molecule state is also modified by the finite range effect in the small a region. The atom-dimer resonances $a_*^{(n)}$ are then related to the distortions of both dimer and trimer energy levels on the $a > 0$ side. In particular, the ground trimer state actually never meets the atom-dimer scattering threshold [65].

The above descriptions on vdW and zero-range universality are illustrated in Fig. 3.13. Two frequently measured observables, three-body recombination rate coefficient L_3 and atom-dimer relaxation rate coefficient $\beta_{\rm AD}$ are plotted as a function of $r_{\rm vdW}/a$ in this figure. The scattering resonances $a_-^{(n)}$, $a_*^{(n)}$ as well as the interference minima $a_+^{(n)}$ (and maxima $a_p^{(n)} \equiv a_+^{(n)}\, e^{\pi/(2s_0)}$, with $e^{\pi/(2s_0)}$ being one half of the Efimov period [66]) are associated with corresponding crossing points on the trimer spectrum through the green dotted lines. The portions of the trimer energies and three-body observables plotted in solid black lines indicate predictions based on zero-range theory. The relative locations of these trimer branches are fixed by zero-range universality. The dashed black lines indicate the portions which are subject to modifications due to finite-range effects in real systems. The locations of these low-lying resonances relative to the more excited ones depend on the details of the interaction potentials.

The basic idea of Fig. 3.13 is the following. In real atomic systems, the experimental observation of a complete Efimov spectrum is thwarted by two factors. One is the finite-range effects which distort the Efimov energy levels at small a's. These regions are indicated by the faint yellow squares whose upper bounds are approximately set by $\pm r_e$ multiplied by a prefactor. The other factor comes from the systematic errors when a is large compared to the de Broglie wavelength λ

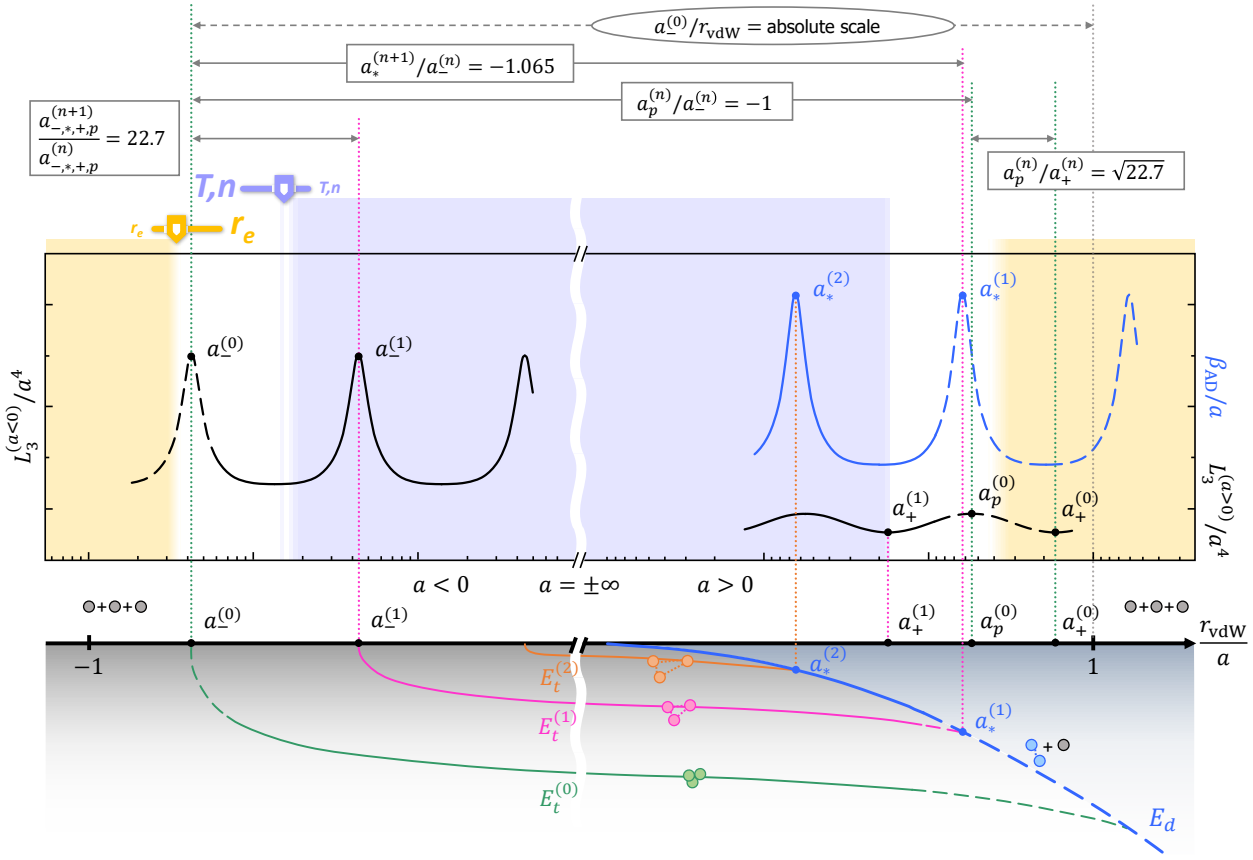

Figure 3.13: Efimov universality. The bottom panel shows trimer ($E_t^{(n)}$) and dimer (E_d) energies as a function of a^{-1}, with energy levels distorted to make clearer the resonance locations. The nth trimer is resonant with three free atoms at $a = a_-^{(n)}$, with the dimer at $a = a_*^{(n)}$. The middle panel depicts the rate constants for inelastic collisions. The three-body recombination constant L_3 peaks at each value of $a_-^{(n)}$; while the atom-dimer relaxation constant β_{AD} peaks at each value of $a_*^{(n)}$. The entire structure is log-periodic with period 22.7. For $a > 0$, L_3/a^4 shows quantum interference, with each local maximum $a_p^{(n)}$ spaced from the corresponding local minimum $a_+^{(n)}$ by $\sqrt{22.7}$. Each value of $a_p^{(n)}$ is related to the corresponding $a_-^{(n)}$ by a factor of exactly -1, but is offset from the nearest value of $a_*^{(n)}$ by 6.5%. Going from relative to absolute values of a requires a single absolute scale indicated by the oval circle. All these ratios are for the zero-range limit; the dashed curves suggest the possibility of perturbations as $|a|$ enters the region, indicated by yellow shading, where it is not large compared to the effective range r_e. The range of the yellow zone may be "adjusted" by choosing atomic species with different r_e. The purple shading represents large $|a|$ regions that are prone to systematic effects such as those caused by finite temperature and density.

or the inter-particle distance $n^{-1/3}$ of the sample. This region is indicated by the purple square whose lower bounds are set by the temperature and number density of the cloud [2] . The above two factors leave us very limited windows for an observation of Efimov's original predictions based on zero-range interaction. These windows are indicated by the white gaps on both sides of the FR pole.

One signature of the zero-range universality is the universal ratios between three-body observables for $a < 0$ (i.e. a_-) and for $a > 0$ (i.e. a_*, a_+ and a_p). We collect all experimental results on these ratios in homonulear systems as summarized in Fig. 3.14 and compare them to a zero-range theory [50] and a two-channel theory that incorporates the FR coupling strength $s_{\rm res}$ [15]. One of the conclusions from the latter theory is the dependence of the ratios on $s_{\rm res}$, which can be traced to the close relationship between $s_{\rm res}$ and the effective range r_e (r_e is in general a function of a and $s_{\rm res}$ as discussed in Section 3.1.2). As pointed out by the two-channel theory, a suppressed r_e is associated with an enlarged universal window, meaning that the ratios obey the zero-range results even on the low-lying trimer state with $n = 0$; whereas for open-channel dominated resonances with relatively large r_e, these ratios slowly approach its zero-range values as n increases from $n = 0$ to $n \geqslant 1$ (see Table 1 in [15]). This predicted trend is evidenced by the experimental values of $a_*^{(1)}/a_-^{(0)}$ in panel (a) of Fig. 3.14. In the zero-range limit, the three-body recombination maxima $a_p^{(n)}$ turns out to be about equal to $a_*^{(n)}$ within a few percent [50, 53]. Therefore we also add this ratio to this summary plot.

In panel (b) of Fig. 3.14, we compile results on another ratio $a_+^{(0)}/a_-^{(0)}$. The scattering interference $a_+^{(0)}$ is not within the scope of the two-channel predictions in [15], so we only compare the experimental values to the zero-range theory. The observable $a_+^{(0)}$ lies deeply inside the small a region for all available species. Therefore it is not surprising to see no particular dependence on r_e for the ratio $a_+^{(0)}/a_-^{(0)}$. This ratio hence does not serve as a promising candidate for the realization of zero-range universality.

[2] These technical issues can be conquered by generating extremely cold samples with low densities for instance in a microgravity environment. We collaborate with the Cold Atom Laboratory (CAL) at NASA's Jet Propulsion Laboratory (JPL) and a group at Washinton State University (WSU) on this project

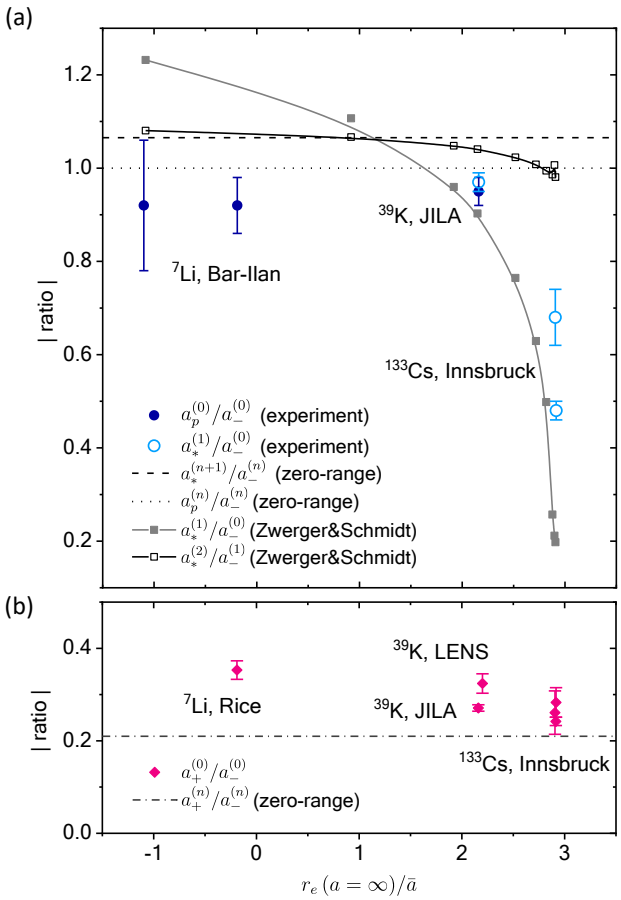

Figure 3.14: Summary of experimental and theoretical results for Efimov's ratios between three-body observables for $a < 0$ and $a > 0$ as function of r_e. r_e is evaluated at unitarity $a \to \infty$ using the model given in the supplemental materials of [18]. Definitions of the three-body observables are illustrated in Fig. 3.13. The zero-range results are predicted by [50, 53]. Zwerger&Schmidt refers to a two-channel model that incorporates the FR coupling strength and provided by [67]. Note that the atom-dimer threshold takes the universal functional form in this theory. The accuracy of this model could be readily improved by using more realistic values of the dimer binding energy [67].

3.3 An Outline of Our Work

In our previous work [18], we studied Efimov physics in the attractive interaction regime, or the so-called Borromean state as defined in Section 3.1.3. The main results are the following:

- We calibrate a FR in ^{39}K with unprecedented precision by doing Feshbach molecule dissociation spectroscopy; this helps refine the two-body coupled-channel model in the s-wave sector.
- We precisely locate an Efimov tri-atomic resonance for $a < 0$, which is a first definitive deviation from the single-channel vdW universal value in homonuclear systems.
- We develop a three-body coupled-channel model based on realistic two-body vdW potentials, and reproduce the measured location and width of the tri-atomic resonance with relatively good agreement.

In this thesis, we extend our precise calibrations of few-body physics to the $a > 0$ region. The main results are the following:

- By mapping out the lifetimes of Feshbach molecules as function of magnetic field, we calibrate the d-wave sector of the two-body coupled-channel model.
- We discover an atom-dimer resonance in ^{39}K and associated finite temperature effects.
- We locate the loss rate interference minimum and maximum for $a > 0$.
- We observe signatures of zero-range universality in ^{39}K by relating the three-body observables for $a < 0$ and $a > 0$.

Chapter 4

Experiments on Feshbach Molecules

In contrast to the attractive interaction regime, Efimov physics in the repulsive interaction regime is relatively less explored and not as well understood. To achieve a global picture of Efimov physics in ^{39}K, we perform a series of two- and three-body collision experiments in the $a > 0$ region. In this chapter, we focus on the experiments on Feshbach molecules (also known as the shallow dimers, or sometimes dimers for short).

4.1 Feshbach Molecule One-Body Lifetimes

Our science state $|F = 1, m_F = -1\rangle$ is not the ground spin state in the Zeeman manifold, meaning that atoms or molecules in the $|1, -1\rangle + |1, -1\rangle$ configuration (or cc channel) can spontaneously relax into lower Zeeman states accompanied by an energy release whose magnitude is a function of magnetic field. A Feshbach molecule is a quasibound state in nature in our case. As depicted in Fig. 4.1, for the incoming cc channel, the decay channels are bc, ac and bb spin configurations. And the energy differences between the exit and entrance channels are on the order of tens of MHz at a magnetic field around 34 G.

4.1.1 Measurements of Feshbach Molecule Lifetimes

The experimental timeline for molecule lifetime measurements is shown in Fig. 4.2 and Fig. 4.3. We use magneto-association to produce the shallow dimers in a standard way. We scan the magnetic field to a negative scattering length and then hold it there for 10 ms to damp

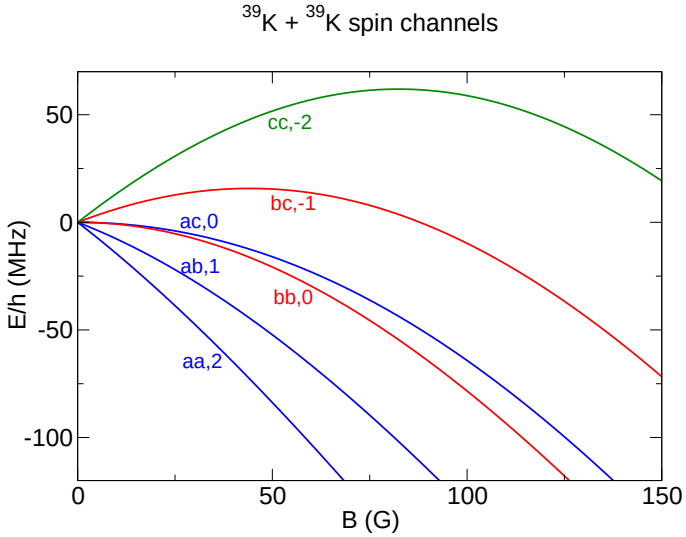

Figure 4.1: Zeeman energies of the d-wave decay channels (bc, ac, and bb) for the incoming cc channel, $0 - 150\,\mathrm{G}$. $a \to |F = 1, m_F = +1\rangle$, $b \to |F = 1, m_F = 0\rangle$, $c \to |F = 1, m_F = -1\rangle$.

out the cloud's breathing motion which is excited by the rapid magnetic field change. We then ramp the field back to the positive side at about $500\,a_0$ as our home field. At this field, we adjust (or eliminate) the number density of the residual atoms. We apply a Gaussian-enveloped adiabatic rapid passage (ARP) pulse followed by an optical blasting pulse to eject the atoms either thoroughly or partially. For our measurement of molecular one-body decay, we remove over 99.9% of the atoms. We optimize this purification process such that it only takes about 0.5 ms and is highly reproducible from day to day. The binding energy of the molecules at this home field is about 500 kHz, so that the molecules are unaffected by the $\Delta = \pm 150$ kHz span of the ARP pulse which flips the free atoms into $|2, -2\rangle$ state with the molecules intact.

To produce molecule samples with different initial conditions (e.g. temperature and number density), we adjust the final stages in the evaporation process prior to the association step. After all these preparations, we jump (within 0.5 ms) the magnetic field to a target science field and let the dimer clouds evolve. At the end of the interrogation, we jump the field back to $500\,a_0$ for detection. An ideal detection scheme for the molecules would be *in situ* absorption imaging in which the spatial distribution of molecules can be preserved. However since we deal with molecule samples of extremely low densities in this spontaneous decay measurement, we choose an alternative method which is to convert them into free atoms by sweeping the magnetic field back to the negative scattering length side so that both parent atoms can be imaged. This method enhances the signal and applies to experiment in which the spatial distribution information of the molecules are not critical.

We map out the molecule population as a function of interrogation time at various magnetic fields. The population decay data is fit into an exponential function to extract the $1/e$ lifetime of the molecules. In survey of the large a regions (at a couple of thousand a_0), we only fit the tails of the data so that the initial decay which is potentially contaminated by the collision-induced loss processes can be excluded. We can comfortably work with low atom numbers from 500 up to 3000 (peak OD from 0.05 up to 0.3) by virtue of the low background noise in our imaging system. The molecule lifetime $\tau_{\rm bg}$ as function of field is presented in Fig. 4.4 panel (a) together with various

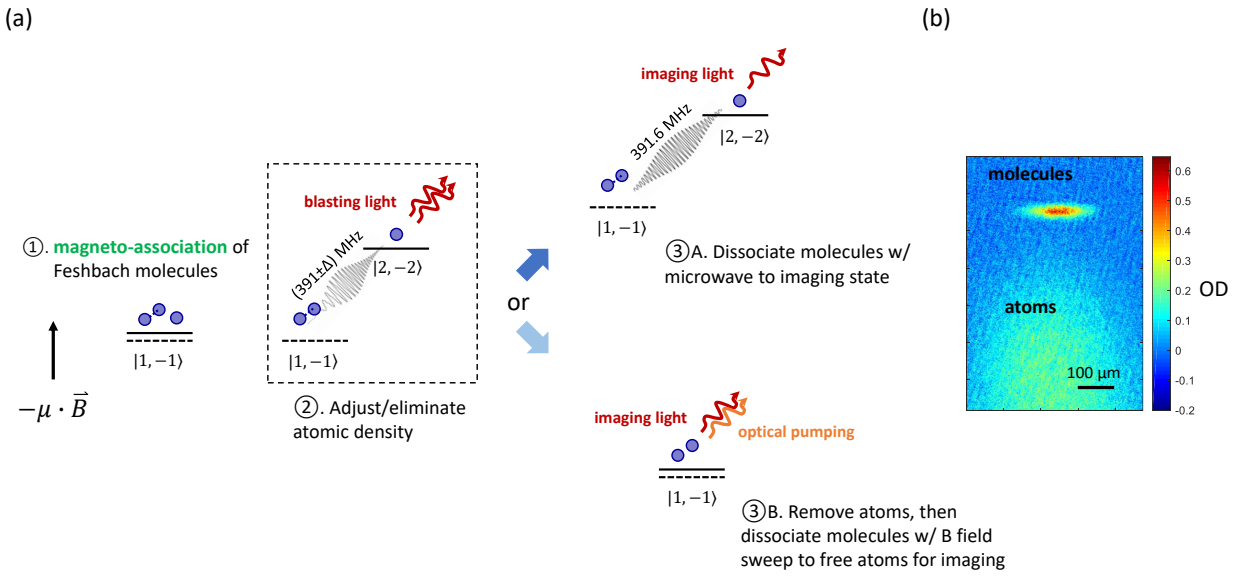

Figure 4.2: Magneto association of Feshbach molecules and atom purification processes (a) and an absorption image of the molecule cloud which is spatially separated from the free atom cloud after the atoms absorbing the blasting photons (b). The step inside the dashed square is skipped for preparation of a full atom number in the atom-dimer collision experiment. The ARP pulse used in this step is made fast and diabatic in order to partially remove the atoms.

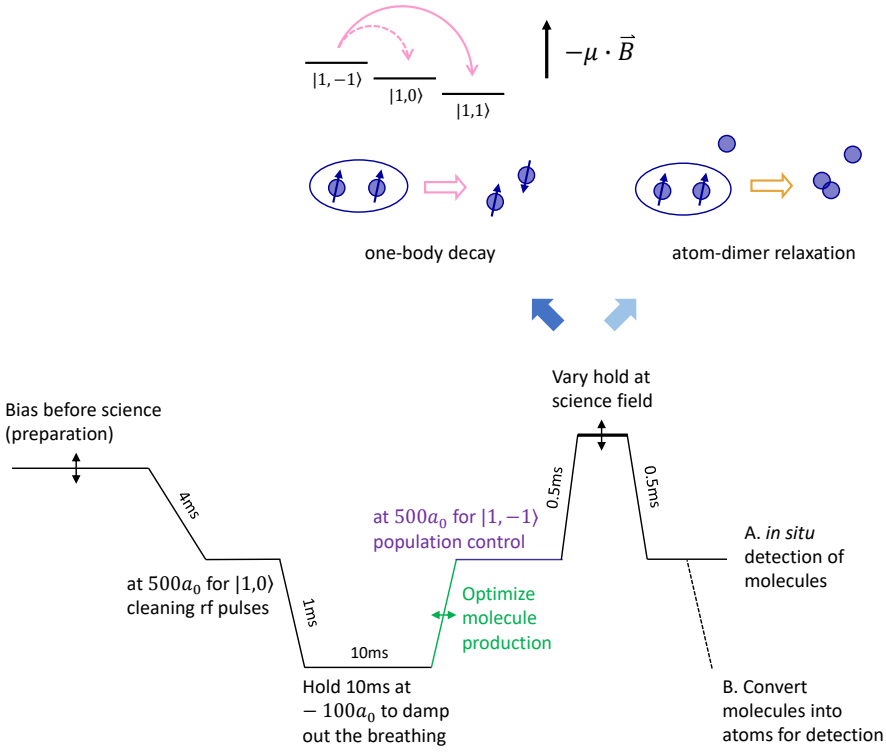

Figure 4.3: Timeline of Feshbach molecule lifetime experiments, B vs. *time*. The double-headed arrows indicate stages that are to be adjusted. The ramps to and from the science field are done in a diabatic way in order to reduce the loss of molecules during the magnetic field sweeps. The blue arrows indicate that at science field two major collision processes can happen. One is molecule one-body decay which is introduced in this section. The other is atom-dimer relaxation which we discuss in 4.2.1.

theoretical models.

4.1.2 A Coupled-Channel Model for the Lifetime of the Quasibound State

For incoming scattering channel with orbital angular momentum $L = 0$ for the relative motion of the two atoms, the bound state responsible for the resonance is also of predominantly $L = 0$ character. However, there is weak coupling from $L = 0$ to the channels with $L = 2$. This coupling is entirely responsible for the inelastic processes involving two free atoms or two atoms in the shallow bound state. The coupling operator is

$$\hat{V}^d(R) = \lambda(R)[\hat{s}_1 \cdot \hat{s}_2 - 3(\hat{s}_1 \cdot \vec{e}_R)(\hat{s}_2 \cdot \vec{e}_R)], \tag{4.1}$$

where $\hat{s}_1$ and $\hat{s}_2$ are the electron spin operators for the two atoms, and $\vec{e}_R$ is a unit vector along the internuclear vector of length R, and the amplitude has the functional form

$$\lambda(R) = E_\mathrm{h}\alpha^2 \left[A_\mathrm{SO} e^{-\gamma R/a_0} + \frac{g_S^2 a_0^3}{4R^3} \right], \tag{4.2}$$

where α is the fine structure constant, g_S is the g-factor of electron. The second term in the above equation is the magnetic dipolar interaction between the two electronic spins. The first term represents the second-order spin–orbit interaction [68], which has been previously ignored in calculations on light species such as K, Na and Li [1] .

In Fig. 4.4 the measured molecule lifetime is compared to a coupled-channel calculation converged with an automated procedure by M. D. Frye and J. M. Hutson. The calculation (dashed line) which neglects second-order spin–orbit coupling shows qualitatively the correct behavior, with a strong peak in the lifetime close to the pole of the resonance and a weaker peak around 46 G. The peak close to the resonance occurs because in this region the quasibound state is dominated by the component in the incoming channel, whose spatial extent scales as a. The subsidiary peak occurs because of interference between the decay amplitudes from the closed-channel and incoming components.

[1] The calculations in this section are to be published in [69] and contributed by M. D. Frye and J. M. Hutson.

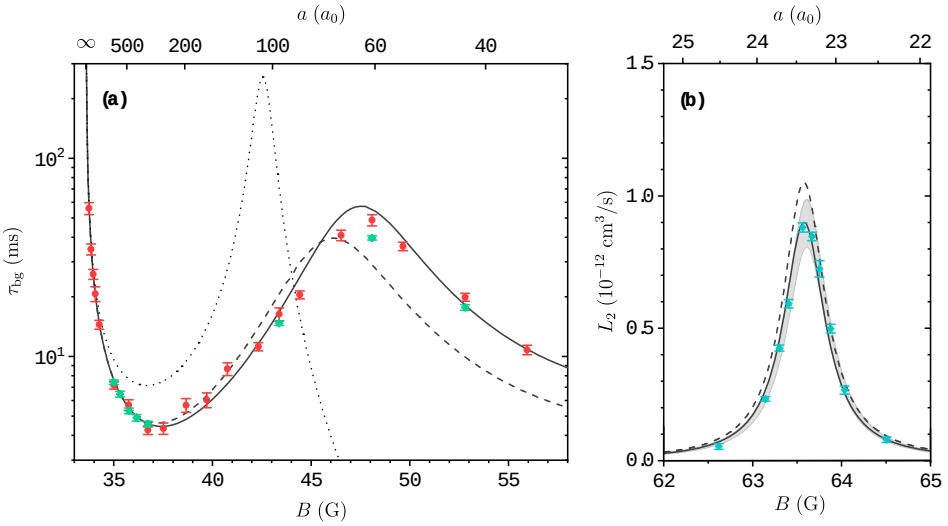

Figure 4.4: Refinement of the d-wave sector of the two-body coupled-channel (cc) model. (a) Lifetime of Feshbach molecules (shallow dimers) measured after the free atoms being removed from the trap. Two different dimer conditions $\langle n_D \rangle = 2 \times 10^9\,\mathrm{cm}^{-3}$, $T = 70\,\mathrm{nK}$ (red circles) and $\langle n_D \rangle = 6 \times 10^{10}\,\mathrm{cm}^{-3}$, $T = 280\,\mathrm{nK}$ (green diamonds) are presented. Solid line: cc-model that includes spin-spin dipolar interaction plus second-order spin–orbit coupling of optimal magnitude; dashed line: cc-model that includes only spin-spin dipolar interaction; dotted line: model from [70]. (b) Comparison of the experimental free-atom spin-relaxation rate constant (teal diamonds) with cc-model calculations. The gray region indicates the experimental systematic uncertainty on atomic density. Solid and dashed curves are produced with the same sets of parameters as being used for the corresponding curves in (a).

The position of the subsidiary peak depends on the ratio of the decay amplitudes from the closed-channel and incoming/open components of the quasibound state. A short-range term in the coupling $A_{\rm SO}$ is introduced to vary this ratio. The results are not very sensitive to the exponent γ, so we fix it at the value 0.7196 obtained for Rb [71]. The solid black line in Fig. 4.4 shows the lifetime with the value of $A_{\rm SO}$ fitted to the experimental lifetimes. The resulting value, $A_{\rm SO} = -0.8$, gives a second-order spin–orbit interaction of $-0.015\,{\rm cm}^{-1}$ at the zero-energy inner turning point of the triplet state of K_2.

Köhler *et al.* [70] developed a model for the lifetime of the quasibound state near a resonance and obtained the expression

$$\tau = \frac{4\pi a^3}{L_2}, \tag{4.3}$$

where L_2 is the zero-energy rate constant for two-body inelastic collision from the incoming channel. Physically speaking, the relaxation of Feshbach molecule in the $B \to B_0$ limit can be viewed as half-collision process in a pre-assigned atomic configuration (in particular encoded in the volume $4\pi a^3$). As shown by the dotted line in Fig. 4.4, this model is a good approximation close to the pole of the resonance. The fact that this mode fails to reproduce the height and location of the subsidiary peak is not surprising since the incoming closed-channel components play a crucial role in τ but not in L_2.

The second-order spin–orbit interaction partially cancels the magnetic dipolar coupling. For the optimized value of $A_{\rm SO}$, $\lambda(R)$ crosses zero inside the classically forbidden region for the triplet state. In ^{39}K the overall coupling is thus dominated by the magnetic dipolar term, and the effect of the second-order spin–orbit term is to reduce slightly the total decay rates due to spin relaxation. Fig. 4.4 panel (b) shows the rate coefficient for two-body inelastic loss across the narrow d-wave resonance near 63.609(4) G with full-width-at-half-maximum of 0.567(12) G. There is a small discrepancy in the calculated position of the resonance, due to remaining deficiencies in the singlet and/or triplet potential curves. Without $A_{\rm SO}$ the prediction overestimates the height of the peak (dashed line), whereas the prediction including $A_{\rm SO}$ agrees with the height and width within the

experimental uncertainties. This provides an independent sanity check on the accuracy of the overall coupling function $\lambda(R)$.

As illustrated in Fig. 4.5, this narrow d-wave resonance at 63.6 G is associated with a ramping d-wave bound state that lies at higher magnetic field. This d-wave resonance is extremely weak, as evidenced by the barely noticeable change in the scattering length going across the pole. As shown in Fig. 4.6, the singularity is almost totally extinguished by the strong resonance decay.

4.2 Finite Temperature Effects in Atom-Dimer Reactions

A through understanding of two-body physics in ^{39}K provides a foundation of the experiments on three-body physics. In this section I discuss in particular how Feshbach molecules interact with free atoms, which is essentially a three-body process. Two atom-dimer resonances have been previously located in ^{133}Cs [72, 73]. The Cs_2 molecules are relatively long-lived in their ground Zeeman sublevel. The locations of the atom-dimer resonances are found to agree with a numerical model based on van der Waals interaction [73]. A lack of discernible temperature dependency on the resonance peaks in these works contradicts the predictions by [74, 75].

4.2.1 Discovery of an Atom-Dimer Resonance

In the atom-dimer reaction experiment, we measure the number and size of the dimers *in situ* as a function of interrogation time as shown in Fig. 4.7. We apply a Gaussian-enveloped rf pulse to dissociate the dimers and spin-flip one of the parent atoms into the imaging state. The frequency of this rf pulse is chosen to be at the empirical peak response of the molecule dissociation spectrum. This rf pulse is of full power so that it can deplete the molecule population in a short amount of time about 120 µs. We then take absorption images on $|2,-2\rangle$ spin state at $500\,a_0$ field with the quantization axis provided by the bias coils. Only one parent atom from each molecule is imaged in this method. We repeat the measurements with various translational temperatures of the molecules. For the lowest temperature 60 nK condition, we only have enough imaging signal by detecting both parent atoms. This is realized in the alternative detection scheme in which the atoms are removed

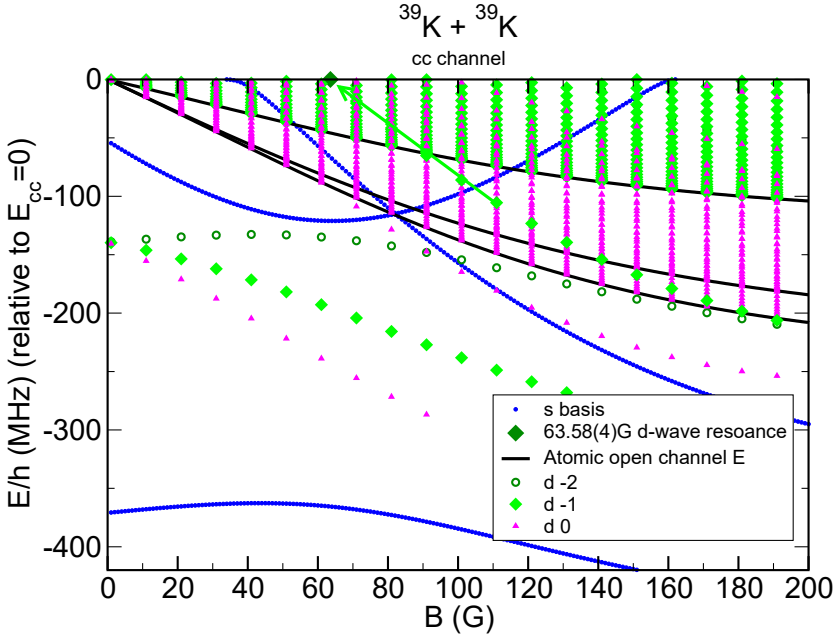

Figure 4.5: Bound state calculations for ^{39}K in *sd*-wave basis, $0 - 200$ G, plotted relative to the cc channel energy as zero. The three bold black lines are the open channel thresholds (bc, ac, bb from top to bottom). Above such thresholds there are the quasi-continua, and below are the true bound states. Bound states are shown for $(L = 0, M_s = -2)$ and for $L = 2$ with $M_s = -2$, -1, and 0. A bound state in the $(L = 2, M_s = -1)$ channel that lies below the bc threshold and above the bb and ac thresholds (represented by the green diamonds) projects to near where the 63.6 G resonance is observed (indicated by the green arrow). Figure is generated by P. S. Julienne.

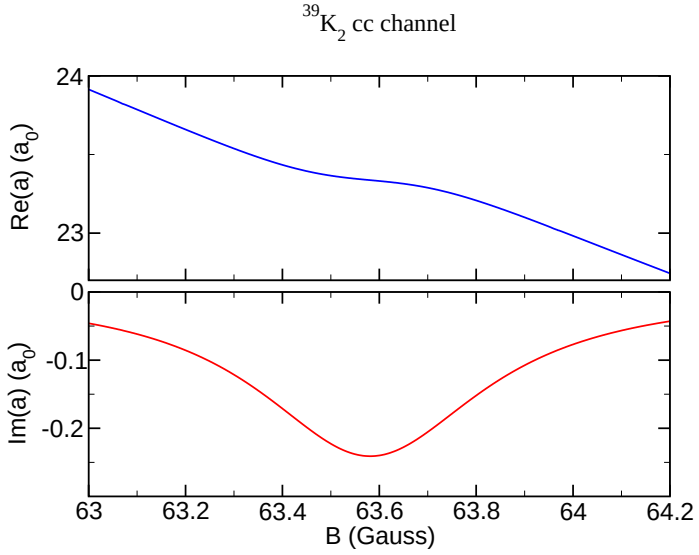

Figure 4.6: Real and imaginary parts of a in vicinity of the narrow d-wave resonance.

at end of the hold time and molecules are swept into free atoms by a magneto dissociation process (Fig. 4.2 step 3B). The temperature information therefore may not be accurately maintained in this case. The width of the molecules along the tightest confinement direction is about 5 µm, which is large compared to our imaging resolution of 1.5 µm. Both molecule width and imaging resolution are given in root-mean-square radius.

In the previous section, I describe how we measure the intrinsic lifetime of the dimers τ_{bg} with atoms completely ejected from the trap. By skipping the atom population control step, we let the molecules interact with atoms in addition to the molecules decaying by themselves. The total lifetime of molecules is denoted as τ_{tot}. Since the atom cloud causing the inelastic decay is 10 to 30 times denser than the dimers, the reaction processes mainly happen between atoms and dimers rather than within dimer themselves. We again fit the dimer population N_{D} with an exponential form and extract its $1/e$ lifetime as a function of scattering length a. We then extract the atom-dimer reaction coefficient from the rate equation:

$$\begin{aligned} \frac{\mathrm{d}N_{\mathrm{D}}}{\mathrm{d}t} \equiv -\frac{N_{\mathrm{D}}}{\tau_{\mathrm{tot}}} &= -\beta_{\mathrm{AD}}\langle n_{\mathrm{A}}\rangle N_{\mathrm{D}} - \frac{N_{\mathrm{D}}}{\tau_{\mathrm{bg}}}, \\ \beta_{\mathrm{AD}} &= \frac{1}{\langle n_{\mathrm{A}}\rangle}\left(\tau_{\mathrm{tot}}^{-1} - \tau_{\mathrm{bg}}^{-1}\right), \end{aligned} \tag{4.4}$$

where $\langle n_{\mathrm{A}}\rangle = N_{\mathrm{A}}\left[m\bar{\omega}^2/\left(4\pi k_{\mathrm{B}}T_{\mathrm{A}}\right)\right]^{3/2}$ is the mean density of atoms in a harmonic trap, where N_{A} is the atom number, m is the atomic mass, $\bar{\omega}$ is the geometric mean trap frequency and T_{A} is the atom temperature. It is worth noting that in our optical trap, the polarizability of dimers is twice that of free atoms. The trap frequencies of the atoms and the dimers are hence the same. And because of the unequal mass, the density distribution of atoms and dimers are different. The spatial overlap between atoms and dimers as a result leads to an overestimation of the relaxation coefficient $\beta_{\mathrm{AD}}^{\mathrm{harmonic}}$ in a harmonic trap in the above equation by a factor of $\frac{8}{\sqrt{27}} \approx 1.5$ compared to $\beta_{\mathrm{AD}}^{\mathrm{homogeneous}}$ for homogeneous gases,

$$\beta_{\mathrm{AD}}^{\mathrm{harmonic}} = \frac{8}{\sqrt{27}}\,\beta_{\mathrm{AD}}^{\mathrm{homogeneous}}. \tag{4.5}$$

As can be told from Fig. 4.8 panel (a), the molecule lifetime gets significantly reduced in the

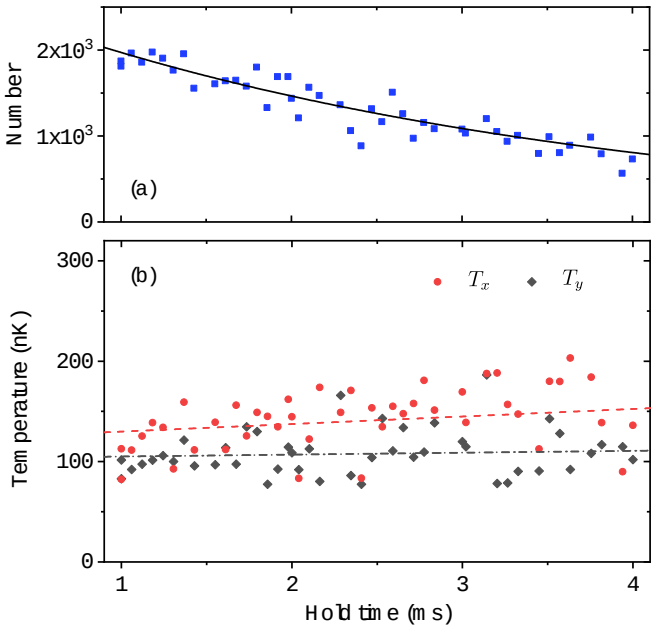

Figure 4.7: Time evolution of dimers measured at $1200\,a_0$ with atoms being the majority in the sample. (a) Dimer number decay (blue squares) fitted with an exponential function (solid line) with a $1/e$ lifetime $\tau_{\rm tot}$. (b) Temperature of dimers extracted from the horizontal ($\hat{x}$, red circles) and vertical ($\hat{y}$, gray diamonds) widths of the cloud from *in situ* images of the molecules. The heating rate on the order of a few nK/s is minimal during the short hold time.

presence of free atoms. By following Eqn. 4.4 we subtract out the one-body decay rate from the dimer total decay rate and obtain the atom-dimer relaxation coefficient β_{AD} at different temperatures as shown in Fig. 4.8 panel (b). A resonance-like peak at around $900\,a_0$ is quite pronounced for all temperatures. With the highest temperature condition, we vary the atom density by ejecting two thirds of the atoms from the trap to confirm that the atom density in this experiment acts as a scaling factor that is divided out to get β_{AD}.

Throughout this thesis, the magnetic field is calibrated with rf spectroscopy. We use the most up-to-date Feshbach resonance calibration given by [18] for the conversion from magnetic field to a. The uncertainty on scattering length amounts to about 5% at around $20,000\,a_0$ and is negligible below $10,000\,a_0$.

4.2.2 Zero-Temperature Model

In the zero collision energy limit, the interaction between atoms and dimers can be described in an *effective field theory* (EFT) formalism [50]. In the presence of deep dimers, the scattering length between an atom and a dimer is

$$a_{\mathrm{AD}} = (1.46 + 2.15\cot[s_0\ln(a/a_*) + i\eta_*])\,a. \tag{4.6}$$

At the atom-dimer scattering threshold $E = -E_b$, the s-wave differential cross section is $|a_{\mathrm{AD}}|^2$. The effects of deep dimers encoded in η_* is to fill in the zeroes of the cross section and prevent it from saturating the unitarity bound. As to inelastic collision, the dimer relaxation constant is deduced from the imaginary part of a_{AD} and given by

$$\beta_{\mathrm{AD}} = \frac{20.3\sinh(2\eta_*)}{\sin^2[s_0\ln(a/a_*)] + \sinh^2\eta_*}\frac{\hbar a}{m}, \tag{4.7}$$

which is a log-periodic function of a_*.

The scaling behavior $\beta_{\mathrm{AD}} \propto \hbar a/m$ can be understood as the following argument. For a reaction event between a free atom and a dimer of size a in a unit volume, three things need to happen. 1) The atom and dimer approach each other at a distance on the order of a. 2) The three

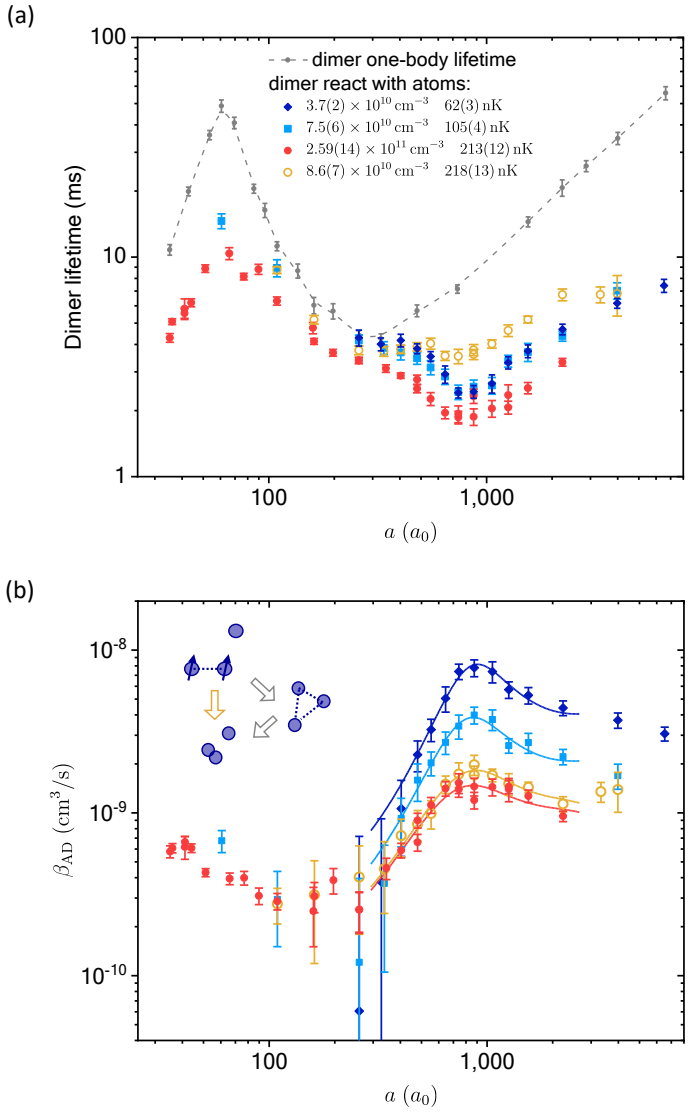

Figure 4.8: (a) Lifetimes of dimers with and without atoms being present at various temperatures. Error bars on dimer lifetimes are extracted from the fitting routine and include only the statistical noise on dimer number. Gray dots represent the intrinsic lifetimes of the dimers. Gray dashed line is a guide to the eye. (b) Temperature dependence of atom-dimer relaxation coefficient β_{AD} as a function of scattering length a. Only atomic density is varied between the two highest temperature data sets. Error bars on β_{AD} stand for 1σ propagated uncertainty involving the statistical error of atom density as well as the uncertainty of dimer lifetimes. Solid lines are fitting curves with a zero-range finite-temperature model [74] at corresponding temperatures. The inset of (b) is a cartoon picture that illustrates the role of a trimer in enhancing the atom-dimer relaxation process as an intermediate decay product.

atoms together come from distance a to R_0 which represents the recombination region. 3) Once they are at R_0 they recombine at a certain rate. The probability for the first two steps are a^3 and $(R_0/a)^2$ (as a property of the scale-invariant hyperradial wavefunction in the $R_0 < R < a$ region ([52], etc.), and the recombination rate of the final step is $\hbar/(mR_0^2)$. In the end, the total rate coefficient turns out to be proportional to $\hbar a/m$. The reason that the short-range length scale R_0 drops out of the picture can also be viewed as a result of the "mode matching" between three free atoms within a distance of a and the Efimov hyperradial wavefunction [76]. In other words, the Efimov channel in the $R_0 < R < a$ region can transport atoms to the short distances without any barriers.

4.2.3 Finite-Temperature Model

We follow the model introduced in [74] to incorporate finite temperature effects in the fitting function for the atom-dimer relaxation data. The decay rate of dimer number is expressed as a thermal average of the rate constant,

$$\frac{\mathrm{d}N_\mathrm{D}}{\mathrm{d}t} = -\frac{1}{2\pi^3}\int_0^\infty r^2\mathrm{d}r\int_0^\infty P^2\mathrm{d}P\int_0^{k_\mathrm{D}} k^2\mathrm{d}k\times\int_{-1}^1 \mathrm{d}x n_\mathrm{A}(p_\mathrm{A},r)n_\mathrm{D}(p_\mathrm{D},r)g(k), \tag{4.8}$$

where $\mathbf{P} = \mathbf{p}_\mathrm{A} + \mathbf{p}_\mathrm{D}$ is total wave number of atom and dimer, $\mathbf{k} = \frac{2}{3}\mathbf{p}_\mathrm{A} - \frac{1}{3}\mathbf{p}_\mathrm{D}$ is relative wave number of atom and dimer, and x is the cosine of the angle between $\mathbf{P}$ and $\mathbf{k}$. We only evaluate the integral of k up to the dimer break-up wave number $k_\mathrm{D} = 2/(\sqrt{3}a)$ for the model to be valid. We assume Boltzmann distribution on $n_\mathrm{A}(p_\mathrm{A},r)$ and $n_\mathrm{D}(p_\mathrm{D},r)$ since the temperature here is always higher than $2\times T_\mathrm{c}$ for atoms. The different density distributions of atoms and dimers in a harmonic trap come into play in this step.

The function $g(k)$ is related to the atom-dimer inelastic scattering cross section,

$$g(k) \equiv \frac{3\hbar k}{2m}\sigma_\mathrm{AD}^\mathrm{inelastic}(k) = \frac{3\hbar k}{2m}\left(\sigma_\mathrm{AD}^\mathrm{total}(k) - \sigma_\mathrm{AD}^\mathrm{elastic}(k)\right), \tag{4.9}$$

where m is the atomic mass. We derive $\sigma_\mathrm{AD}^\mathrm{total}(k)$ and $\sigma_\mathrm{AD}^\mathrm{elastic}(k)$ from the atom-dimer scattering amplitude $f_\mathrm{AD}(k)$ that is parametrized by series of the product ka [74]. The short-range properties

of atom-dimer scattering are encoded in $f_{\mathrm{AD}}(k)$ by a_* and η_* which serve as the fitting parameters in our case. We then evaluate the integrals in Eqn. 4.8 to fit β_{AD} from $300\,a_0$ up to $2500\,a_0$. The upper bound guarantees that the temperature of the data always stays below one tenth of the dimer break-up energy. The lower bound is due to the assumption that this model breaks down outside the universal regime.

We use the Boltzmann distribution function for a harmonic trap whose geometric mean trap frequency is denoted as $\bar{\omega}$,

$$n_i(p_i, r) = \left(\frac{\hbar\bar{\omega}}{k_{\mathrm{B}}T}\right)^3 N_i \exp\left[-\frac{1}{k_{\mathrm{B}}T}\left(\frac{\hbar^2 p_i^2}{2m_i} + \frac{m\bar{\omega}^2 r^2}{2}\right)\right], \tag{4.10}$$

with the normalization condition being $\int \mathrm{d}^3r \int (2\pi)^{-3}\mathrm{d}^3p_i\, n_i(p_i, r) = N_i$ $(i = \mathrm{A}, \mathrm{D})$. By combining Eqn.4.8 with Eqn.4.4, we obtain the following expression for $\beta_{\mathrm{AD}}(T, a)$

$$\beta_{\mathrm{AD}}(T, a) = \frac{4}{\sqrt{\pi}} \frac{\hbar^3}{(mk_{\mathrm{B}}T)^{3/2}} \int_0^{k_{\mathrm{D}}} k^2 \mathrm{d}k \exp\left[-\frac{3\hbar^2k^2}{4mk_{\mathrm{B}}T}\right] g(k). \tag{4.11}$$

The algorithms for the numerical evaluation of this formula can be found in Appx. C. Some predictions from this model are plotted in Fig. 4.9 at various temperatures. In the $T \to 0$ limit this finite-temperature model perfectly reproduces the zero-temperature EFT result multiplied by a factor of 1.5 which accounts for the spatial overlap between atom and molecule clouds. It is worth noting that in the large a limit, this model predicts a suppressed β_{AD}. This trend is consistent with an independent model explained by [77]. To understand this behavior, consider that for $ka \gg 1$ atoms do not interact beyond the distance of $1/k$. The three-step argument in this regime is now modified as the following. 1) The two atoms in the dimer approach each other at a distance $1/k$ with a probability of $1/ka$. This can be calculated from the universal dimer wavefunction. 2) The third atom also gets to the distance $1/k$ with a probability of $1/k^3$ assuming a unit volume. 3) The three atoms come to R_0 from $1/k$ with a probability of $(kR_0)^2$. The recombination rate at the short range is again $\hbar/(mR_0^2)$. In the end, the total rate becomes $\beta_{\mathrm{AD}} \propto \hbar/(ak^2)$. Briefly, the suppression comes from the mode-matching that happens only at distances $1/k$ instead of a [76]. The above description presumes a well-defined atom-dimer channel for $ka \gg 1$.

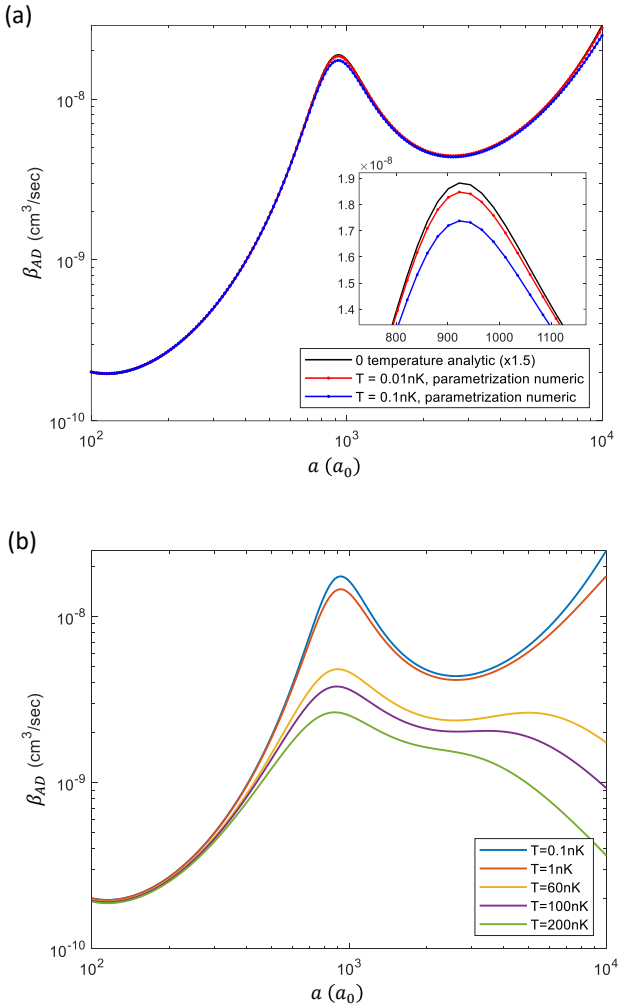

Figure 4.9: Finite-temperature model predictions for atom-dimer reaction rate coefficient β_{AD}. (a) Compare the finite-temperature predictions at 0.01 nK (red line) and 0.1 nK (blue line) to the zero-temperature EFT prediction (black line). Inset: zoom in on the atom-dimer resonance peak on linear scale. The zero-temperature theory is multiplied by a factor of about 1.5 to account for the spatial overlap between the atom and dimer clouds in thermal equilibrium in a harmonic trap. This comparison justifies the validity of the finite-temperature theory in the $T \to 0$ limit. (b) β_{AD} vs. a at various temperatures. The three highest temperatures represent the conditions used in our experiment. Their peak height is highly suppressed due to the finite temperature effects.

In the fitting process, the temperature of the sample is an input parameter to the fitting function and measured with absorption images on atoms after a long time-of-flight. As depicted by the solid lines in Fig. 4.8 panel (b), this finite temperature model captures the shape of the atom-dimer resonance across the whole temperature range accessed in our experiment.

4.2.4 Temperature Dependency of Atom-Dimer Resonance

In the above mentioned two fitting protocols, short-range physics is lumped into three fitting parameters, a_*, η_* and magnitude A_*. Similar to the definitions in the $a < 0$ region, a_* denotes the atom-dimer resonance position at zero temperature and describes how close the three particles can get together in the presence of any repulsive inner wall on the potential; η_* denotes the width of the resonance and quantifies how absorptive the wall is; a_* and η_* bundled together serve to fix the real and imaginary part of the three-body parameter (3BP). A_* indicates the global numerical factor in front of β_{AD}. It is associated with the total effect of deeply bound molecules on the inelastic exit channel, which can be a model-dependent number. It also handles experimental errors on the absolute density of atoms.

The fitting parameters are summarized in Fig. 4.10 as well as in Table 4.2.4. In contrast to the phenomenological fit results from a zero temperature model [78], the finite-temperature model reveals an energy independent three-body observable $a_*^{(1)}$ that we associate with the first excited Efimov trimer state. We determine $a_*^{(1)}$ to be $884(14)\,a_0 = 13.7(2)\,r_{\mathrm{vdW}}$ from the weighted mean of the four experimental points, indicated as the solid line in Fig. 4.10 panel (a). Combining $a_*^{(1)}$ with the three-body recombination resonance $a_-^{(0)} = -908(11)\,a_0$ [18], we obtain $a_*^{(1)}/\left|a_-^{(0)}\right| = 0.97(2)$. This number is only 8% lower than the universal ratio of 1.06522 obtained from the zero-range theory [50, 53]. Considering the fact that our $a_-^{(0)} = -14.05(17)\,r_{\mathrm{vdW}}$ dramatically deviates from the value according to the single-channel van der Waals universality, the ratio reported in this work implies that short-range physics shifts the absolute positions of the two resonances in the same direction while leaving their relative positions unchanged. Interestingly enough, the width parameter η_* overlaps with the previously measured η_- for $a < 0$ within experimental uncertainties

$\bar{T}_{\mathrm{atom}}$	$\langle n_{\mathrm{A}} \rangle$	$\langle n_{\mathrm{D}} \rangle$	$\bar{\omega}/2\pi$	$a_*^{(1)}$	η_*	A_*
nK	$10^{10}\,\mathrm{cm}^{-3}$	$10^{9}\,\mathrm{cm}^{-3}$	Hz	a_0		
218(13)	8.6(7)	7.8	42.7	901(28)	0.31(3)	0.85(9)
213(12)	25.9(1.4)	7.8	42.7	853(43)	0.37(6)	0.67(9)
105(5)	7.5(6)	6.4	24.4	862(28)	0.26(4)	1.14(19)
62(3)	3.7(2)	1.4	17.1	896(24)	0.26(3)	1.55(15)

Table 4.1: Atom-dimer resonance measurement conditions and fit results. The magnitude A_* includes corrections for the density overlap between atom and dimer clouds according to the temperature measurements on those two components respectively. The error bars on temperature and density represent the standard deviation of statistical noise.

(see Fig. 4.10 panel (b)). With the above observations, we report a 3BP that continuously connects $a < 0$ and $a > 0$ at short range, although it is approached along disparate scattering channels in these two regions in the long range.

4.3 Analysis of Systematic Effects

4.3.1 Atom-Dimer Thermal Equilibrium

The temperature of the samples used as an input parameter in the fitting function is measured with the atom component. Since the molecule creation efficiency is closely correlated with the local properties of the atom cloud in a harmonic trap, the molecule component may be created somewhat out of equilibrium with the atom component. This causes uncertainty on the spatial overlap between the atom and molecule clouds that enters the fitted global magnitude of β_{AD}. This issue is inevitable in our case since the decay of molecules is relatively fast compared to the thermalization rate. Extracted from their in-trap sizes, the effective temperature of molecules can be up to 30% higher than the temperature of atoms (Fig. 4.11). The magnitude of β_{AD} which scales as $T^{-3/2}$ thus can be at most 70% off from its correct value.

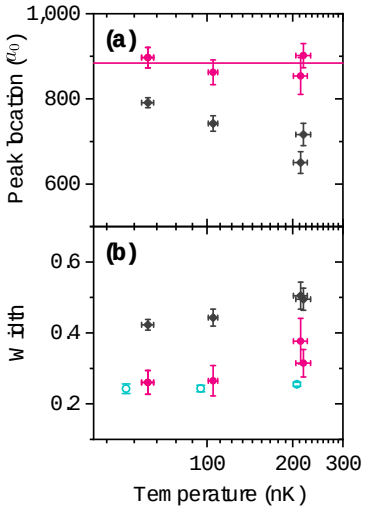

Figure 4.10: Summary of the three-body observables extracted from finite-temperature and zero-temperature models. (a) Whilst the zero-temperature model (black diamonds) gives a phenomenological peak location of the atom-dimer resonance that shifts up as temperature decreases [78], the finite-temperature model (magenta circles) reveals the true short-range atom-dimer 3BP that is independent of temperature. (b) Temperature effect plays a remarkable role in the width of the resonance. It broadens the resonance feature hence leads to an incorrectly large η_* in the zero-temperature fit. The η_* from the finite-temperature model is free of this broadening effect and reflects the intrinsic width of the Efimov trimer state at zero energy. It is consistent with η_- (open teal circles) reported in our previous work [18].

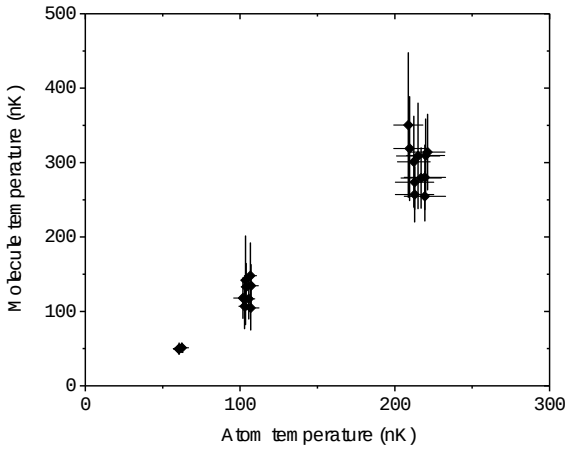

Figure 4.11: Comparison of atom temperature and molecule temperatures in the atom-dimer reaction experiment. The out-of-equilibrium of the two components stems from two processes. One is magneto association of molecules which has a spatially selective efficiency. The other is the rapid inelastic collisions between atoms and molecules subsequent to the magneto association. The latter process preferably consume the molecules near the center where the atoms are the densest. Note that the sagging between atom and molecule clouds due to gravity is negligible in our case.

4.3.2 Atom-Dimer Chemical Equilibrium

Near the pole of the resonance at positive a, the temperature of the cloud is no longer low compared to the binding energy of the shallow dimers. In the absence of any dissipative processes, atom and dimer relative populations are fixed by the chemical equilibrium condition. The dimer density is related to the atomic density by

$$n_{\mathrm{D}} = n_{\mathrm{A}}^2 \lambda^3 2\sqrt{2}\, e^{E_d/(k_{\mathrm{B}}T)}. \tag{4.12}$$

This equilibrium condition is described by the Saha-Boltzmann equation [79]. Two mutually time-reverse processes – three-atom recombination into shallow dimers and atom-dimer collisional breakup – balance each other to form a dynamic equilibrium [80, 77]. We numerically estimate the density of created atoms as function of scattering length at various dimer sample initial conditions (see Appex. C for details of the program). A box trap is used here for simplicity. As depicted in Fig. 4.12, atoms start to show up gradually around $1500 - 3000\, a_0$ for the temperature range of $60 - 300\,\mathrm{nK}$. In experiments we indeed observe free atoms emerging from initially pure dimer samples at large a's (see e.g. Fig. 4.14).

4.3.3 Dimer-Dimer Inelastic Collisions

One qualitative way to tell if dimer-dimer relaxation is competing with atom-dimer relaxation is to see if the dimer decay data deviates from the exponential functional form. According to this criterion, inelastic collisions between dimers is not a concern in our experiment on atom-dimer relaxation. A small deviation from exponential function can only be seen by going beyond $2000\, a_0$ and also cranking up the dimer density at the same time. To quantify the dimer-dimer relaxation rate in this large a region, we prepare pure dimer samples of relatively high density and extract the dimer-dimer inelastic collision coefficient γ_{DD}. The rate equations turn out not trivial in this large a region for two reasons. The first reason is that the dynamical field ramp can project molecule and atom states onto each other when ramping beyond roughly $2500\, a_0$. The second reason is that chemical equilibrium in the large a region requires a finite population of atoms at

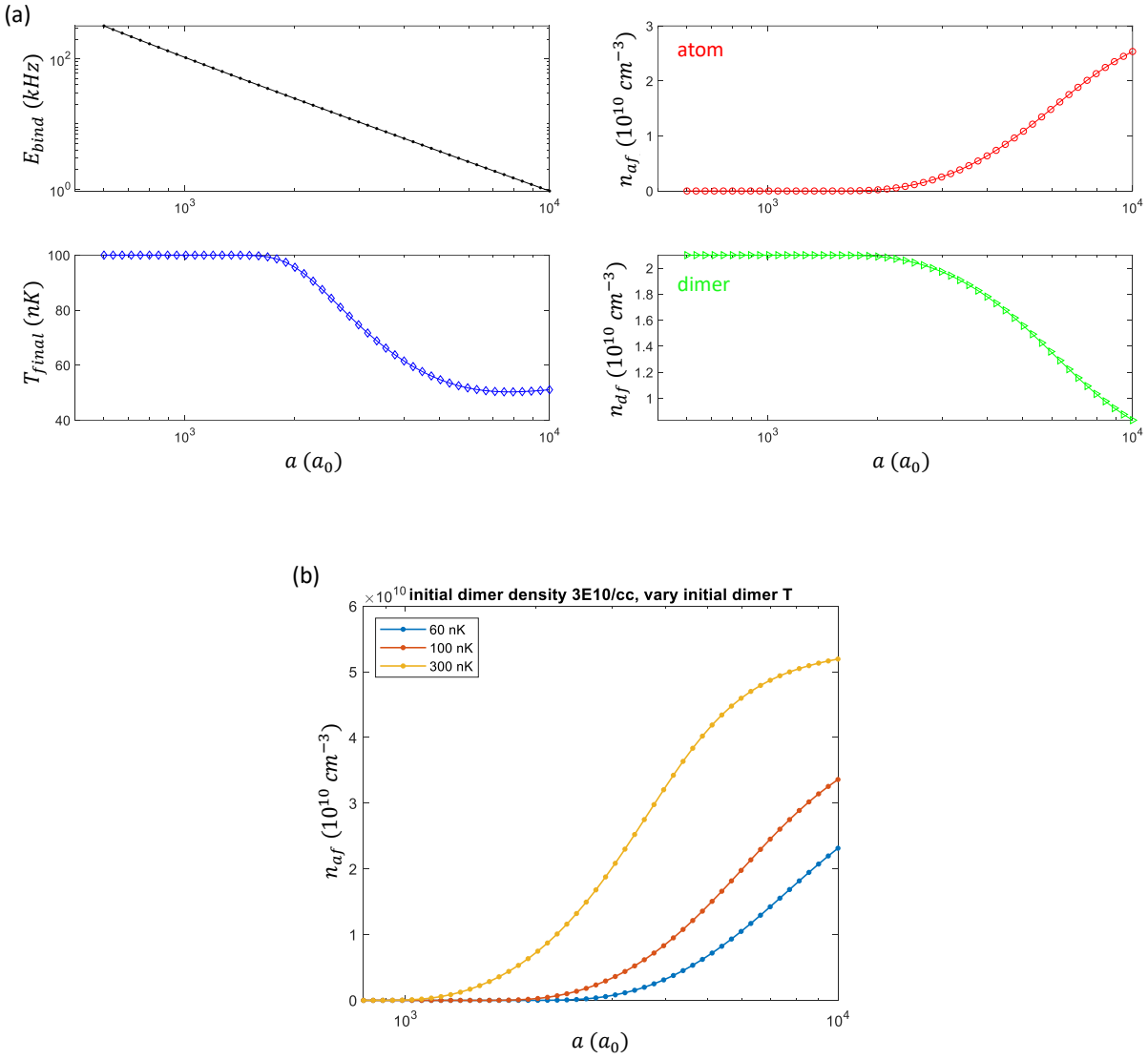

Figure 4.12: Atom-dimer chemical equilibrium condition as function of scattering length for (a) dimer initial temperature 100 nK and density $2.1 \times 10^{10}\,\mathrm{cm}^{-3}$. E_b is assumed to take the universal form. It can be seen that atoms start to show up at around $2000\,a_0$. (b) The same calculation is repeated with various initial dimer temperatures.

the experimentally available temperatures as discussed previously. In our case, these created atoms can consume molecules and lead to additional losses.

One solution to the first issue is to pick a new home field at $3000\,a_0$ to purify the molecules as well as for detection. Molecules are not energetically separated from atoms very well due to its small binding energy of 12 kHz at this field. We take the advantage of the magnetic field insensitivity on the $|F=1, m_F=-1\rangle$ to $|F=2, m_F=0\rangle$ transition and apply Gaussian π-pulses with Fourier width of ± 3 kHz to spin-flip the atoms. We then use two cascaded ARPs to further bring atoms into the $|F=2, m_F=2\rangle$ state to receive the blasting light. Detection of atoms or molecules is done at the same field with the final spin state being $|F=2, m_F=-2\rangle$ instead. And another solution is to design a two-step magnetic field ramp to large a region so as to stay adiabatic with respect to E_b throughout the ramp (Fig. 4.13).

To address the second issue, we image atoms and dimers individually to track both populations as a function of interrogation time. We take *in situ* images on both components to get the best signal-to-noise and to directly obtain their density distributions. We use the following coupled rate equations to describe the evolution of dimer density n_{D} and atom density n_{A}:

$$\begin{aligned}
\frac{\mathrm{d}n_{\mathrm{D}}}{\mathrm{d}t} =& -\frac{n_{\mathrm{D}}}{\tau_{\mathrm{bg}}} - \beta_{\mathrm{AD}} n_{\mathrm{A}} n_{\mathrm{D}} - \gamma_{\mathrm{DD}} n_{\mathrm{D}}^2 - \delta_{\mathrm{AD}} n_{\mathrm{D}}^2 + \delta'_{\mathrm{AD}} n_{\mathrm{A}}^2 n_{\mathrm{D}} + \text{ higher order terms in } n_{\mathrm{A}}, \\
\frac{\mathrm{d}n_{\mathrm{A}}}{\mathrm{d}t} =& -\beta_{\mathrm{AD}} n_{\mathrm{A}} n_{\mathrm{D}} - 2\delta'_{\mathrm{AD}} n_{\mathrm{A}}^2 n_{\mathrm{D}} + 2\delta_{\mathrm{AD}} n_{\mathrm{D}}^2 + \text{ higher order terms in } n_{\mathrm{A}},
\end{aligned} \tag{4.13}$$

where γ_{DD} denotes dimer-dimer relaxation coefficient into deeply bound states, δ_{AD} and δ'_{AD} are the dimer dissociation/formation coefficients for atom-dimer conversion. For atom-dimer conversion, we only consider the leading order binary process and its inverse ternary process $\mathrm{K_2}+\mathrm{K_2} \leftrightarrow \mathrm{K_2}+\mathrm{K}+\mathrm{K}$ given that atom density is small compared to dimer density [80]. Molecules containing more than two atoms are ignored here for simplicity. Keeping only the linear terms in n_{A} and using the empirical β_{AD} values, we numerically fit the coupled rate equations and extract γ_{DD}. This fitting process is presented in Fig. 4.15.

We map out γ_{DD} as a function of a in Fig. 4.16. The range in a is too limited to display any scattering length dependence. Below $2000\,a_0$, we hardly observe any deviation from exponential

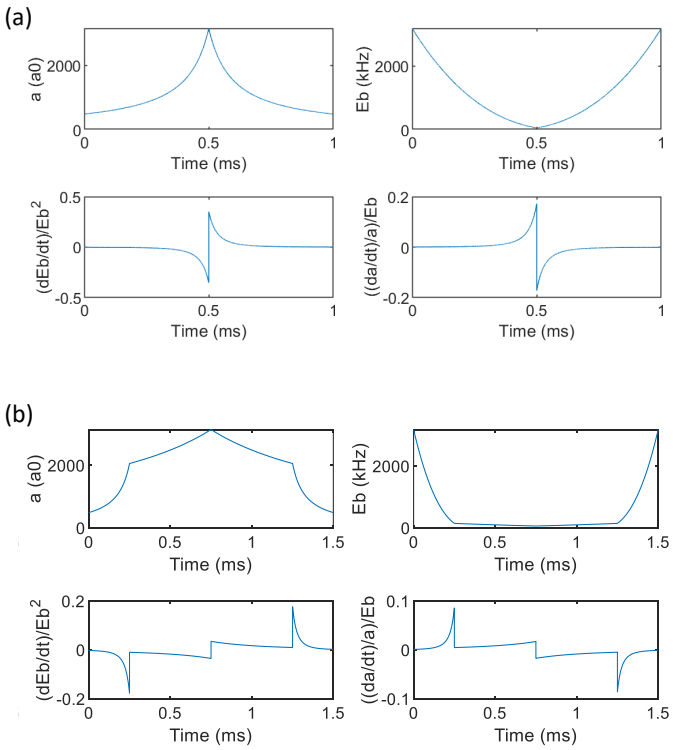

Figure 4.13: A two-step ramp to large a while staying adiabatic with respect to E_b. (a) Due to the non-linear forms of the E_b and a as function of B, a single linear magnetic field ramp can become highly diabatic near the end. (b) By doing two linear ramps with the latter step being slow, we can reduce the dimer-to-atom conversion associated with the dynamics induced by the ramp. Adiabaticity is qualitatively characterized by the dimensionless quantities $(dE_b/dt)/E_b^2$ and $(da/dt)/a/E_b$ here.

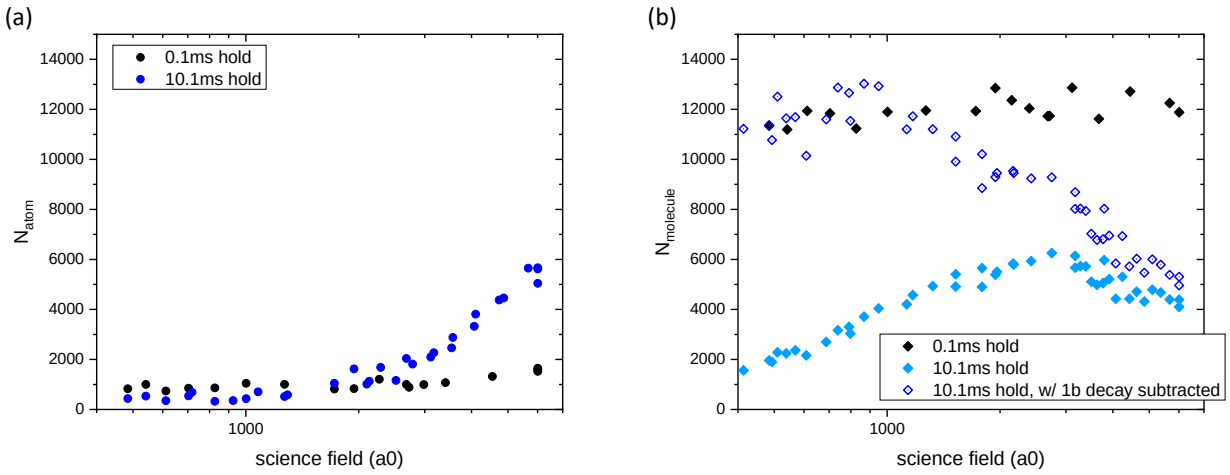

Figure 4.14: Atom formation as function of a in dimer-dimer experiment. A home field at 3000 a_0 is used to kill off the atoms. The data at short hold time 0.1 ms reflects the effect from the field ramp. The data at long hold time 10.1 ms reflects the dynamics at a certain science field. By subtracting out the dimer one-body decay rate, we obtain the dimer-dimer loss as presented by the open blue diamonds in (b). Part of the lost dimers are converted into free atoms as shown in (a). The rest of the lost dimers decay into deeply bound states. In the former process, the chemical equilibrium is in fact never reached due to the dissipative nature of the dimers. The latter process is what we are interested in and can be associated with the loss constant γ_{DD}.

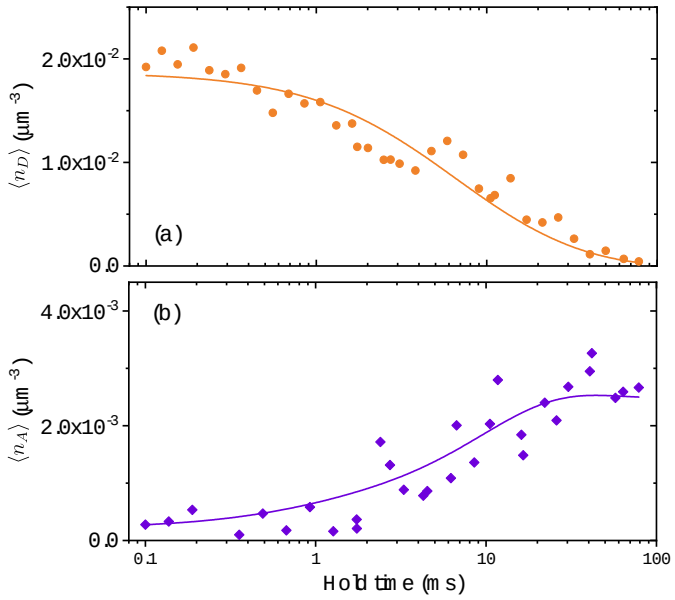

Figure 4.15: Time evolution of dimers and atoms at 150 nK, 3500 a_0 with dimers initially being the majority in the sample. (a) Dimer number (orange circle) decay can be associated with multiple inelastic processes. (b) Formation of a small number of atoms (purple diamonds) is driven by the atom-dimer conversion towards chemical equilibrium. This is similar to the process reported in [81] except that our dimer state is highly dissipative in nature. Dimer and atom data are simultaneously fitted with Eqn. 4.13 as indicated by the orange and purple lines respectively.

decay form even with our highest dimer density $2.5 \times 10^{10}\,\mathrm{cm}^{-3}$, neither can we observe any atoms being created. With the dimer densities used in the atom-dimer experiment $(1.4 - 7.8) \times 10^{9}\,\mathrm{cm}^{-3}$, the lower bound on the dimer-dimer relaxation time is on the order of hundreds of milliseconds to seconds. This is significantly longer than the time scales of the atom-dimer relaxation in the scattering length range of interest. Therefore we can safely ignore the collisions between dimers in the data analysis in Section 4.2.1.

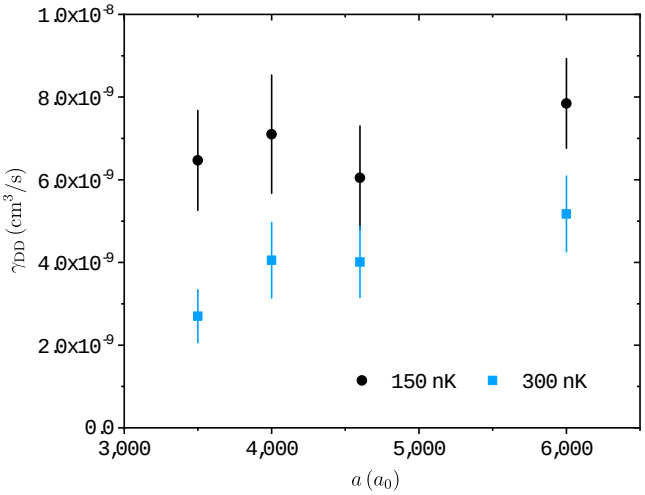

Figure 4.16: Dimer-dimer relaxation coefficient into deeply bound molecules measured above $3000\,a_0$. γ_{DD} is extracted from the fit with the coupled rate equations 4.13. A slight difference in magnitude can be resolved between the two temperatures. This measured γ_{DD} has the same order of magnitude as a theoretical simulation done for ^{133}Cs in [82].

4.3.4 Residual Breathing Motion of the Atom Cloud

The atom clouds present residual breathing motion during the atom-dimer relaxation process in spite of the 10 ms hold time added to damp it out. The breathing motion is at twice the trapping frequencies and is relatively slow compared to the dimer lifetimes. In order to estimate the atom density uncertainty introduced by this breathing mode, the sizes of the atom cloud are being traced for at least one period along the slow direction as presented in Fig. 4.17. The amplitude of the

fractional size change is up to about 5%. The actual correction to the atomic density is less than 3% during the short dimer lifetimes. They are calculated based on a sinusoidal fit whose phase is extracted from *in situ* sizes of the atoms. The corrections to atom densities are included in individual conditions listed in Table 4.2.4.

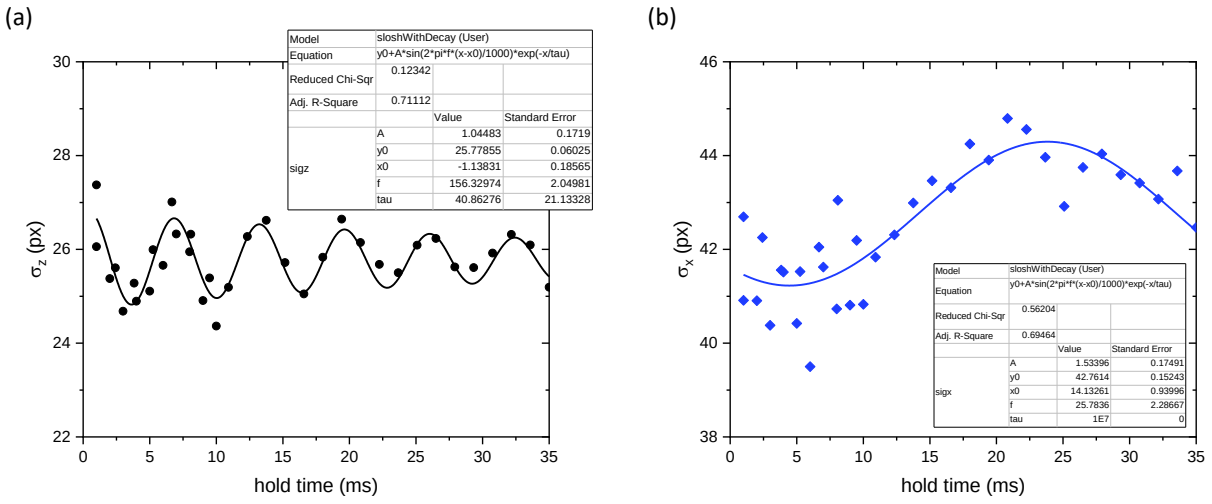

Figure 4.17: Residual breathing motion of atoms in atom-dimer relaxation experiment along the vertical (a) and horizontal (b) directions measured at a long time-of-flight. The breathing frequencies are twice the trapping frequencies along corresponding directions. The inset tables show the fitting parameters in a damped sine function.

4.3.5 *In Situ* Detection of Molecules

As a Feshbach molecule is dissociated by microwave field, the parent atoms acquire excess kinetic energies from the blue-detuned microwave photons. This leads to a fast expansion of the cloud as can be seen from Fig. 4.18. We make sure that the time gap in between the dissociation pulse and imaging pulse is of minimal duration so that the parent atom cloud can largely preserve the *in situ* density distribution of the molecule cloud.

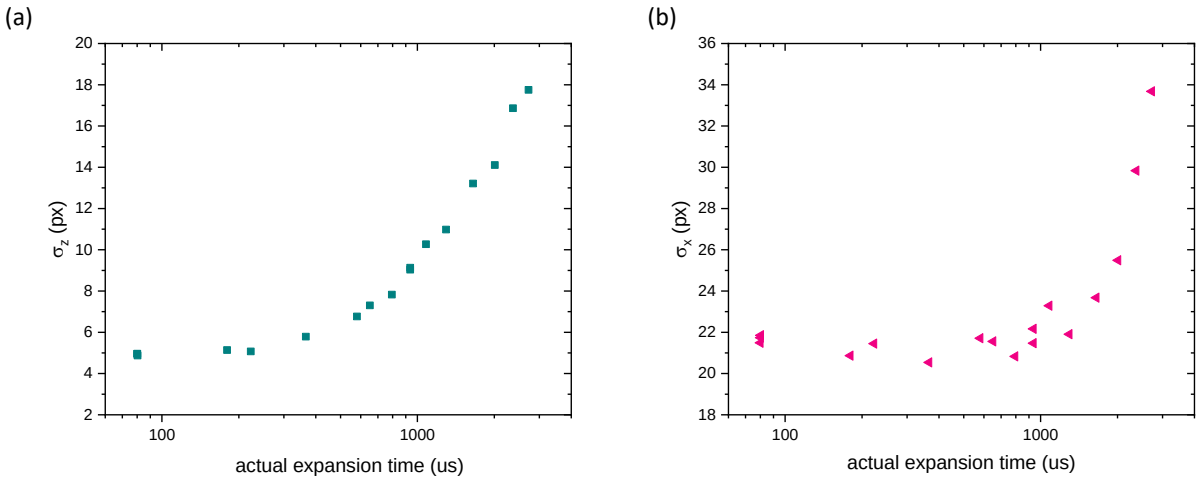

Figure 4.18: Expansion of post-dissociation molecule cloud along the vertical (a) and horizontal (b) directions. The x-axis expansion time is defined as the interval between the microwave dissociation pulse center and imaging light pulse center. The fast expansion of the dissociating atoms is consistent with the excess energy of the blue-detuned microwave photons.

4.4 Bound-to-Bound Transitions

For the remainder of this chapter, we explore the viability of using bound-to-bound transitions to detect the real component of the atom-dimer and/or dimer-dimer scattering length. The idea is to take the advantage of a narrow transition lineshape and a stable final state to probe small mean-field energy shifts in the loosely-bound upper level. One potential challenge is the tiny transition dipole moment that is limited by the Franck-Condon overlap between the initial and final states. The three bound states of interest can be found in Fig. 3.3 and Fig. 3.6.

We calculate the off-diagonal matrix element between two bound states to estimate how small the transition dipole is. The coupled-channel representation of the wavefunction of a certain bound state can be expressed as

$$\Psi_\alpha(r) = \sum_{\nu=1}^{5} f_\nu^{(\alpha)}(r) \left|\nu\right\rangle, \tag{4.14}$$

where $\alpha = -1, -2, -3$ indexing the three shallowest bound states, $\nu = 1, 2, 3, 4, 5$ indicating the five channels on the basis of free atom asymptotes, $f_\nu^{(\alpha)}(r)$ represents the projections onto these channels. Fig. 4.19 gives the amplitude of projections as function of inter-nuclear distance r. The transition dipole can then be calculated by evaluating the off-diagonal matrix elements

$$\left\langle\Psi_\alpha\right| \mu_B g_S S_z + \mu_N g_I I_z \left|\Psi_{\alpha'}\right\rangle = \int_0^\infty \left\langle\nu\right| \mu_B g_S S_z + \mu_N g_I I_z \left|\nu'\right\rangle f_\nu^{(\alpha)}(r) \cdot f_{\nu'}^{(\alpha')}(r) r^2 dr, \tag{4.15}$$

where μ_B, μ_N are the Bohr magneton and nuclear magneton, g_S and g_I are the g-factors of the electrons and nuclei, respectively, and S_z, I_z are the corresponding spin operator components in the direction of the magnetic field. A longitudinal magnetic rf drive is used since the total m_F is conserved in this kind of transition. The dipole moments turn out to be really small, only $0.05\,\mu_B$ for the $(-1) \to (-2)$ transition and $0.01\,\mu_B$ for the $(-1) \to (-3)$ transition at 35 G. And it decreases even more as we go to larger a.

The small dipole moment severely limits the Rabi frequencies on these transitions. We improve our magnetic field control system by suppressing the rf rectification as described in Section 2.1.6 so that we can send rf or microwaves at their maximal powers to the atoms. In the end, we are

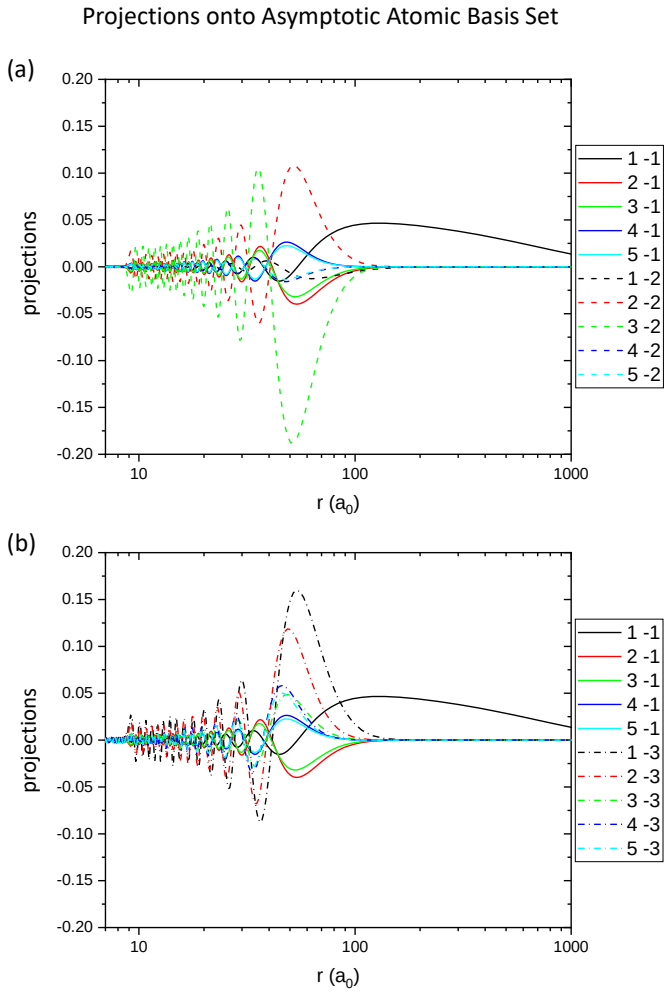

Figure 4.19: Projections of shallow dimers onto asymptotic atomic basis set as function of internuclear distance r, evaluated at 35 G. 1 $\rightarrow$ cc channel, 2 $\rightarrow$ db channel, 3 $\rightarrow$ ec channel, 4 $\rightarrow$ fd channel, 5 $\rightarrow$ ee channel. (-1) indicates the shallowest bound state (Feshbach molecule), (-2) and (-3) indicate the second and third shallowest bound states. The binding energies of the second and third bound states are calculated to be about $E_b^{(-2)} = 105\,\mathrm{MHz}$ and $E_b^{(-3)} = 363\,\mathrm{MHz}$ respectively at 35 G field. It is worth noting that the cc (open) channel component of Feshbach molecule state has a large weight in the classically forbidden region, which is as expected.

able to shovel a decent fraction of Feshbach molecules into the (-2) bound state by square pulses. The molecule population transferred to (-2) state manifests as losses in the (-1) state as shown in Fig. 4.20. Our pulse duration is limited by the magnetic field sensitivity of this transition about $0.5\,\mu_B$. The uncertainty on the center frequency is 100-200 Hz which is unfortunately not good enough to resolve the small energy shift due to atom-dimer or dimer-dimer interactions. For the $(-1) \rightarrow (-3)$ transition which is less sensitive to the magnetic field but requires even higher pulse power, we are only able to see some number losses from the (-1) state by using a frequency-scanning ARP.

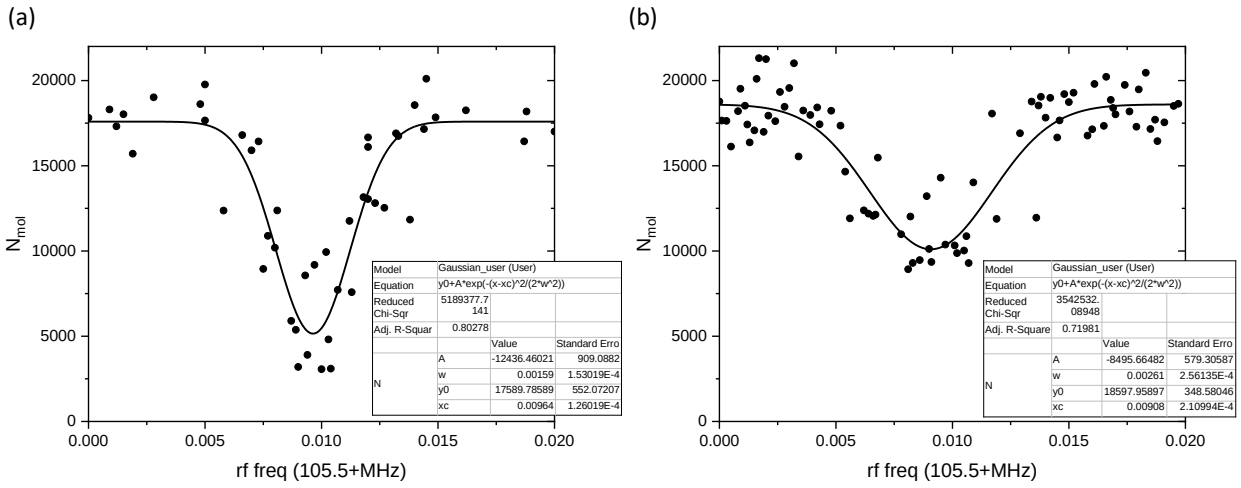

Figure 4.20: Bound-to-bound transition spectra for the $(-1) \rightarrow (-2)$ transition at about $500\,a_0$ field. N_{mol} stands for the remaining number of Feshbach molecules. A square pulse of 200 µs duration is applied in (a). Its Fourier width (r.m.s.) is about 1.7 kHz. A square pulse of 150 µs duration is applied in (b). Its Fourier width (r.m.s.) is about 2.3 kHz. The fitting functions and parameters are listed in the inset tables. Both spectra have Fourier-limited widths.

Chapter 5

Experiments on Free Atoms

In Ch. 4, we elaborated on three-body Efimov physics involving Feshbach molecules as an essential component. The other set of three-body observables in the $a > 0$ region can be located by scanning along the free atom scattering threshold instead of along the atom-dimer scattering threshold. Unlike on the $a < 0$ side, the three-body recombination rate constant $L_3^{(a>0)}$ is free of scattering resonances because the trimer states never meet the free atom scattering continuum on the positive side. Instead, $L_3^{(a>0)}$ is a sinusoidal function of a, featuring a series of interference minima and maxima, which are denoted by $a_+^{(n)}$ and $a_p^{(n)}$ respectively in this thesis. The parentage of associated Efimov trimer state is indexed by the integer n, whose physical meaning is the number of nodes in the three-body hyperradial wavefunction. Knowledge of $L_3^{(a>0)}$ are complementary to that on $\beta_{\rm AD}$ since the atom-dimer scattering potential which acts as the entrance channel in atom-dimer reaction now becomes the exit channel in three-atom recombination. Although $L_3^{(a>0)}$ has been previously measured on a variety of atomic species, we are the first group to report all values of $a_+^{(n)}$, $a_p^{(n)}$ and $a_*^{(n)}$ that can be used to characterize the Efimov spectrum for a homonuclear system.

5.1 Experimental Sequence

The experimental sequence for the three-body recombination measurements is relatively straightforward. At the end of the evaporation sequence, we ramp up the trap depth adiabatically to suppress residual evaporation. A typical timeline of the experiment can be found in

Fig. 5.1. The final trap depth is set to be 10 times the temperature of the cloud whereas the trap depth is found to be 8 times the temperature of the cloud in equilibrium as presented in 2.1.3. The peak value of the phase-space density (PSD) of the clouds is always restricted to below 1 to ensure Boltzmann statistics. Due to the small magnitude of L_3 on the positive side ($L_3^{(a>0)}$ is in fact three orders of magnitude smaller than $L_3^{(a<0)}$ at the same value of $|a|$!), this peak PSD is made to be a few times higher than that used in the $L_3^{(a<0)}$ measurements in order to avoid too long interrogation times. We avoid using BECs because they introduce density-related many-body effects which can be difficult to interpret. In order to ensure that the atoms are in thermal equilibrium, we must keep the three-body recombination rate small compared to the two-body elastic collision rate, i.e. $\Gamma_{3,inel}/\Gamma_{2,el} \ll 1$. For our case, $\Gamma_{3,inel}/\Gamma_{2,el} = (0.05 - 0.21)\lambda n a^2$ for finite scattering lengths and $\Gamma_{3,inel}/\Gamma_{2,el} = 0.04 n\lambda^3$ for unitary gases [83], where λ is the de Broglie wavelength and n is the number density. Therefore, a small PSD is always desired to satisfy the thermal equilibrium condition.

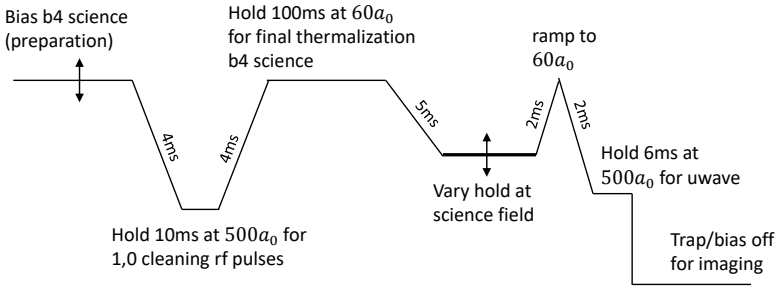

Figure 5.1: Timeline of three-body recombination experiments, B vs. *time*. The arrows indicate stages that are to be adjusted.

In order to cover a wide range dynamic in a, we stitch various initial conditions together. As illustrated in Fig. 5.2 panel (a), the dynamic range of a certain condition is limited on the low a side due to the competing timescales from the two-body loss and background loss, and on the high a side by the lack of thermal equilibrium. The timescales of the background loss (i.e. vacuum

lifetime) are given in 2.1.3. All conditions are generated in the H2+V crossed dipole trap setup except for the highest temperature one which is generated in the H1+V setup for the purpose of maximizing the number density. As shown in Fig. 5.2 panel (b), at small scattering lengths, the atom loss becomes dominated by the background loss. This limits our lowest sampled a to be at around $100\,a_0$. The competing timescales in this small a region were not scrutinized in previous works.

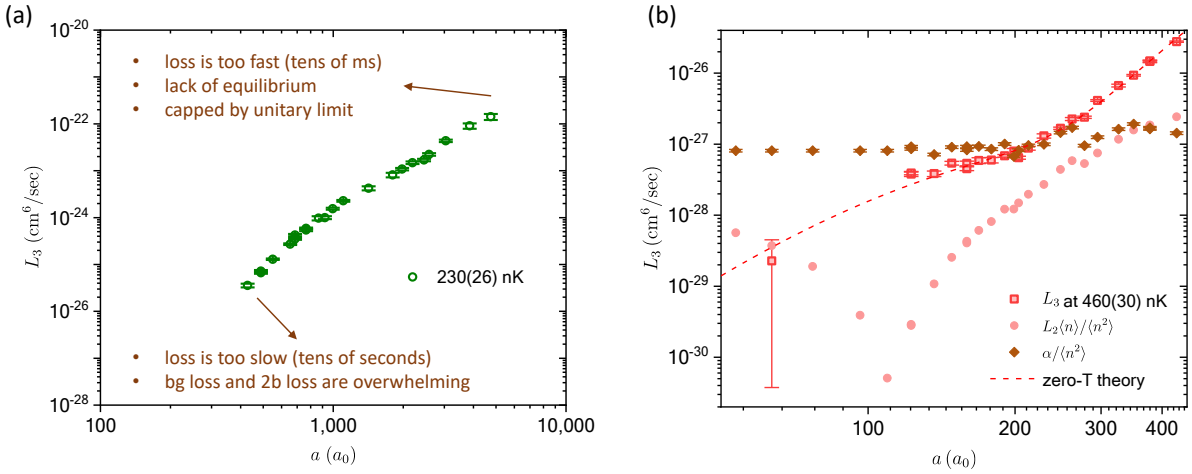

Figure 5.2: (a) Dynamic range of individual condition in three-body recombination experiments. Here the 230 nK data is used as an example. (b) Comparison of the three-body recombination rate coefficient L_3 (squares) with theoretical two-body inelastic collision rate L_2 (circles) as well as background loss rate α measured on the $|1,1\rangle$ ground spin state (diamonds). L_2 and α are rescaled by empirical $\langle n^2\rangle/\langle n\rangle$ and $\langle n^2\rangle$ respectively to give the proper dimension.

5.2 Experimental Results

The measured $L_3^{(a>0)}$ as function of a at various temperatures is presented in Fig. 5.3 together with our previously reported $L_3^{(a<0)}$ in [18]. Six different conditions are combined together to cover an eight order-of-magnitude range on L_3. The good overlaps between adjacent conditions indicate minimal density-dependent systematic effects (see 2.1.5 for discussions on absorption imaging method). Since the overall scaling of L_3 obeys an a^4 law as anticipated for pair-wise interactions

[84], this scaling factor is divided out from $L_3^{(a>0)}$ in Fig. 5.4 in order to emphasize the logarithmic periodic modulation on L_3 due to Efimov physics.

The destructive interference minima $a_+^{(n)}$ (or constructive interference maxima $a_p^{(n)}$) can be elucidated in the picture of a Fabry-Pérot cavity. As illustrated by the inset cartoon in Fig. 5.4 right panel, the couplings between different hyperspherical potentials behave effectively as "mirrors" in the three-body recombination pathways. The location of the inner mirror R_1 is set by the range of interaction r_0, and the location of the outer mirror R_2 is set by the scattering length a in low energy limit ($R_2 = \min(|a|, 1/k)$ in general) [85]. The two decay pathways are associated with weakly and deeply bound molecular channels respectively. They are coherent and can interfere with each other. By scanning the scattering length a (or equivalently the "length" of the cavity), interference minima and maxima show up with a period that is determined by the Efimov scaling factor $e^{\pi/|s_0|}$ defined in Ch. 3. A more rigorous expalanation of generic recombination pathways can be found in Fig. 9 of [53].

In order to extract $a_+^{(0)}$, we numerically fit the data set of 460 nK with an S-matrix formalism that is introduced in [86]. The fitting curves are represented by the red solid lines in Fig. 5.4 and Fig, 5.3. In this model, short-range physics is lumped into three fitting parameters, $a_+^{(0)}$ and η_+ accounting for the location and contrast of the interference minimum, and a scaling factor A_+ for adjusting the global magnitude. Only collisional process of zero total angular momentum has been included in the model. We obtain $a_+^{(0)} = 246(6)\, a_0$, $\eta_+^{(0)} = 0.20(2)$ and scaling factor of unity. This result agrees with the fit with a zero-energy model within uncertainties [50], indicating the negligible effects from finite temperature in this small a region. To extract $a_p^{(0)}$, we then fix the contrast parameter to 0.20 in the same finite temperature model and fit the data sets of 410 nK and 230 nK with their empirical temperatures as inputs to the fitting function. These fitting results are summarized in Table 5.2. All data and fits are plotted individually in Appx. E. As we move on to larger a's, severe temperature effects lead to noise and obscure the first excited minimum $a_+^{(1)}$. A better understanding of the finite temperature effects and also systematic effects is needed to truly nail down the location of $a_+^{(1)}$.

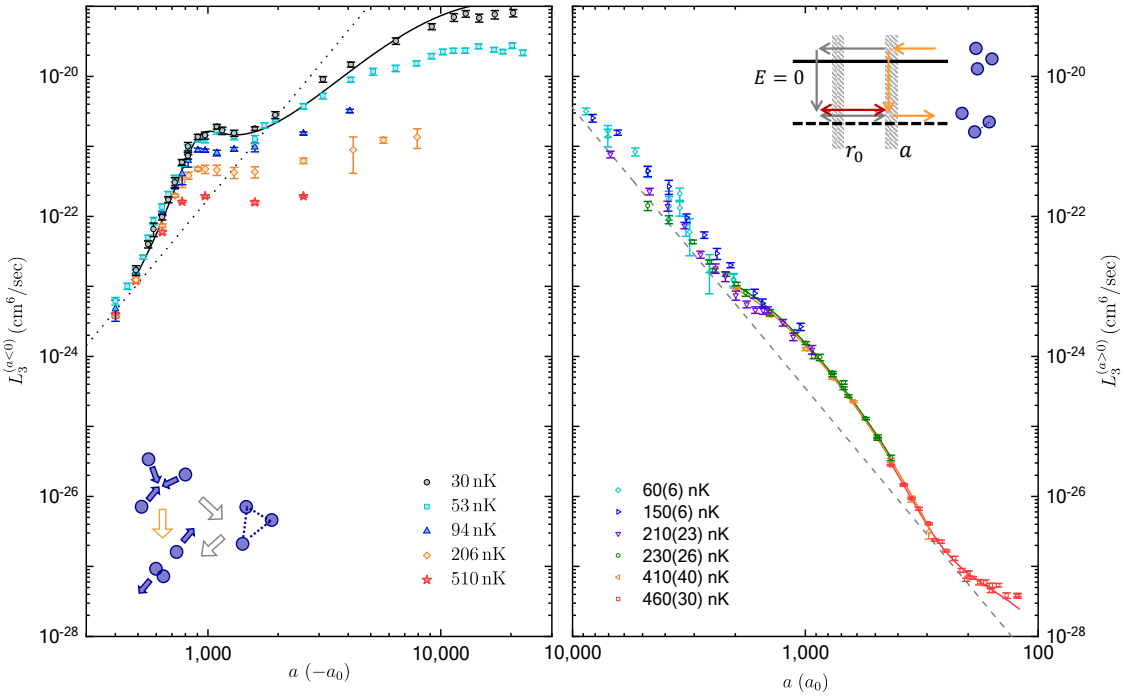

Figure 5.3: Compilation of L_3 measurements for $a < 0$ (left panel) and $a > 0$ (right panel) respectively. Solid lines represent finite-temperature model fits. The dotted line on the left panel represents the a^4 scaling in the absence of Efimov physics. The inset cartoon picture illustrates the role of a trimer in enhancing the three-body recombination process as an intermediate decay product. The dashed line on the right panel represents recombination into deeply bound dimers with $\eta = 0.20$. The inset cartoon picture illustrates the coherent interference between different decay paths in three-body recombination into shallow dimers.

$T_{\rm i}$ nK	$\bar{T}$ nK	$\langle n\rangle_{\rm i}$ 10^{11} cm^{-3}	$\bar{\omega}/2\pi$ Hz	$a_+^{(0)}$ a_0	$a_p^{(0)}$ a_0	η_+	A_+
370	460(30)	51.2(4.2)	260.1	246(6)	–	0.20(2)	0.99(8)
300	410(40)	26.4(2.8)	79.4	–	893(28)	0.20(0)	0.74(2)
150	230(26)	9.9(9)	54.6	–	860(28)	0.20(0)	0.77(2)

Table 5.1: Three-body recombination conditions and fit results. $a_+^{(0)}$ and $a_p^{(0)}$ are fit in a local range of scattering lengths to avoid presumptions about the absolute value of Efimov period. The η_+ with fitting errors of zero are fixed parameters in the fit. T_i and $\bar{T}$ denote initial temperature and temperature averaged over the decay time respectively. The error bar on $\bar{T}$ represents the variance during the interrogation time. $\langle n\rangle_{\rm i}$ is the initial density-weighted density. The error bar on $\langle n\rangle_i$ represents the standard deviation of statistical noise. $\bar{\omega}$ is the geometric mean of trap frequency.

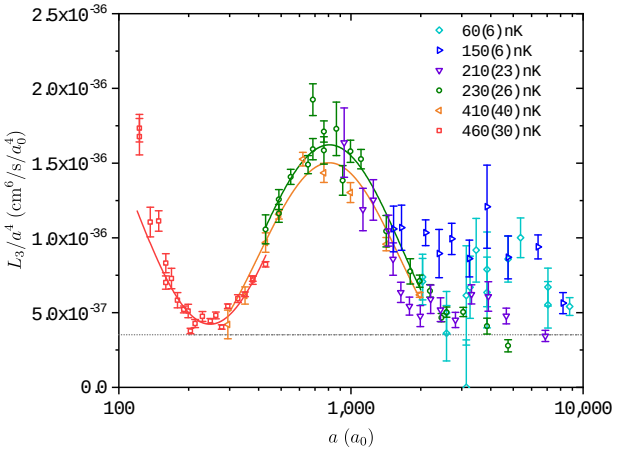

Figure 5.4: Three-body recombination coefficient L_3 scaled by a^4, measured at 460(30) nK (red squares), 410(40) nK (yellow left-pointing triangles), 230(26) nK (green circles), 210(23) nK (purple down-pointing triangles), 150(6) nK (blue right-pointing triangles), 60(6) nK (cyan diamonds). Colored solid lines represent finite-temperature model fits either to the neighborhood of the maximum or the minimum. The gray dotted line represents the recombination into deeply bound dimer states with $\eta = 0.20$.

5.3 Analysis of Raw Data

In the atom number loss measurements, absorption images are taken after a long time-of-flight to track both population decay and heating as a function of interrogation time. To describe the three-atom recombination decay process, we use the following rate equation for atom number N:

$$\frac{1}{N}\frac{\mathrm{d}N}{\mathrm{d}t} = -\alpha_{\mathrm{bg}} - L_2\langle n\rangle - L_3\langle n^2\rangle, \tag{5.1}$$

where $\langle n\rangle = N\left[m\bar{\omega}^2/\left(4\pi k_{\mathrm{B}}T\right)\right]^{3/2}$ is the spatially averaged density-weighted density, $\langle n^2\rangle = N^2\left[m\bar{\omega}^2/\left(2\sqrt{3}\pi k_{\mathrm{B}}T\right)\right]^3$ is the averaged density-weighted square density, and α_{bg} is the background loss rate which is calibrated for each individual condition on the lowest spin state $|F=1, m_F=1\rangle$ at about $60\,a_0$. The temperature of the sample T is being tracked at the same time and fitted into polynomial functions which are then plugged into the above rate equation in the form of cloud density. The d wave resonance at 63.6 G introduced at the end of 4.1.2 is measured in a similar manner with the L_3 term being neglected in the small a region.

Ideally, we use relatively high density cloud while keeping the phase space density low so that the leading contribution to the number loss is from the L_3 term. This is the case for the data below $2000\,a_0$. We fix L_2 to its theoretical value in our fitting function and float the value of L_3 in this regime. We call this method fitting protocol I.

The density dependence of the losses in large a region turns out to be not so straightforward. To figure out the actual decay mechanisms that are involved, we vary the density of the cloud by ten orders of magnitude and float both L_2 and L_3 in the fitting process. The obtained L_2 and L_3 values as shown in Fig. 5.5 are relatively constant. This implies that these two terms alone can deplete the density dependence and no four-body or higher order terms are needed in the rate equation.

Although we can always extract L_2 and L_3 by floating them in the rate equation, the fitting uncertainty is fairly large due to the inseparable time scales of two- and three-body losses for a single sample condition. To suppress the fitting error, we combine decay data sets that are

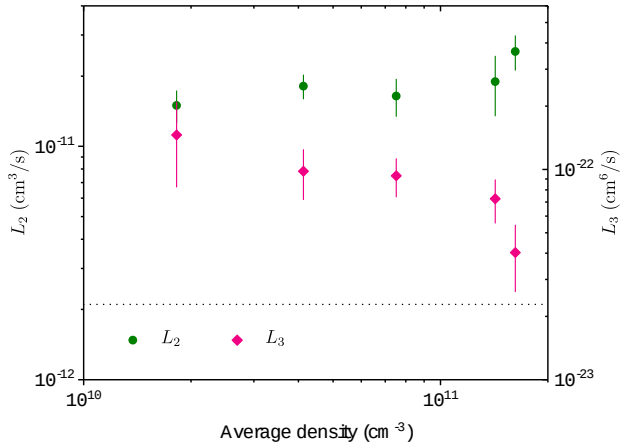

Figure 5.5: Two- and three-body loss coefficients extracted from atom samples of various densities at 210 nK, 3000 a_0. The dotted line shows the theoretical prediction of L_2 at this field.

taken on two samples of drastically different densities but identical temperatures and fit them simultaneously. This fitting method is presented in Fig. 5.6. In this fitting protocol II, L_2 and L_3 are shared parameters between data sets while atom numbers and temperatures from each data set are independent. All the data points above $1000\,a_0$ in Fig. 5.3 and Fig. 5.4 come out of fitting protocol II. The fitting algorithms are documented in Appx. D.

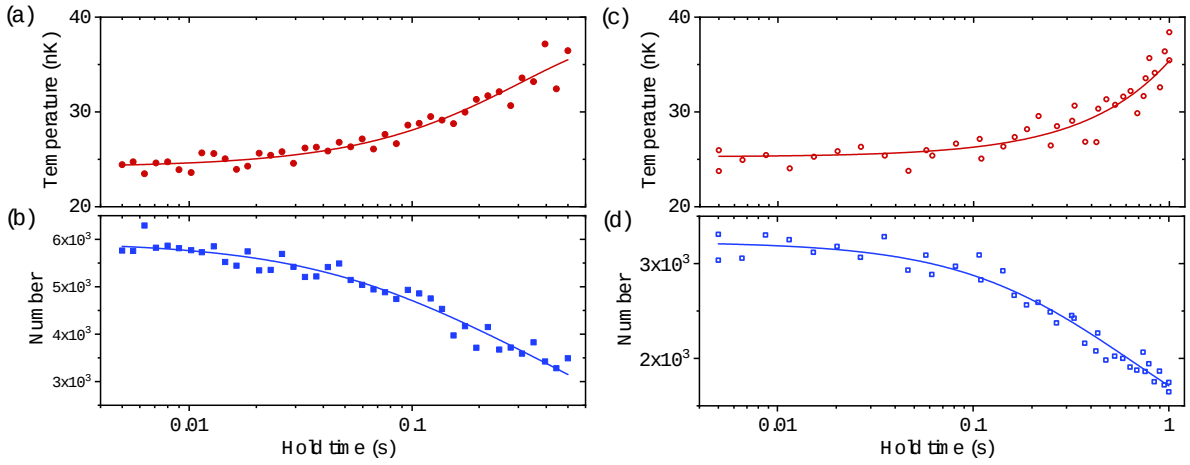

Figure 5.6: Illustration of fitting protocol II that combines atom samples of two different initial densities but same time-averaged temperatures. (a)-(d) Time evolution of number (blue squares) and temperature (red circles) for the high density condition (solid symbols) and low density condition (open symbols) respectively. The data traces are taken at 3000 a0. Red solid lines are fitting curves for temperatures with polynomial functions. Blue solid lines are fitting curves for atom numbers with Eqn. 5.1.

Above $2000\,a_0$, we discover some enhanced two-body losses that can not be explained by the two-body coupled-channel theory. The abnormally high L_2 is plotted in Fig. 5.7. This inconsistency is rather unexpected considering the perfect overlap between experiment and theory on the dimer spontaneous dissociation lifetime in the same region (see Section 4.1.2). Our detailed two-body model of ^{39}K does not predict a resonance in the vicinity of $a = 3000a_0$. Our analysis protocol II yields not only the unexplained excess two-body decay at $a = 3000a_0$, but also scattered temperature dependence of the three-body rate for $a > 1500a_0$. Taken together these results suggest that the overall explanation may come from some combination of uncharacterized systematic errors. We note that as a becomes larger in magnitude, the binding energy of the dimer is no longer much

greater than $k_{\mathrm{B}}T$, opening up other collisional channels. Also the energy released by three-body decay into the shallow dimer becomes no longer large enough to eject the decay products with absolute certainty [87, 77]. Finally, the cloud begins to become collisionally opaque, opening the possibility of decay products undergoing some collisional cascade. Our simple attempts to develop a model for our observations could not establish any of these mechanisms as leading to a definitive explanation. A more sophisticated model that incorporates effects such as secondary collisions will be needed to track down the kinetics in this large positive a regime.

Below in Section 5.5, hypothesized sources of systematic effects in atom loss rate experiment are discussed. However, none of them are well supported by the auxiliary measurements that we made.

5.4 Finite Temperature Model of Three-body Recombination

We follow closely the S-matrix method introduced in [86] to fit L_3 as a function of a in order to account for the finite temperature effects. The three-body recombination coefficient is formulated as:

$$L_3 = N_{\mathrm{lost}} K_3(T) = N_{\mathrm{lost}} \frac{\displaystyle\int_0^\infty \mathrm{d}E E^2 e^{-E/(k_{\mathrm{B}}T)} \left(K_{\mathrm{shallow}}^{(J=0)}(E) + K_{\mathrm{deep}}^{(J=0)}(E) \right)}{3! \displaystyle\int_0^\infty \mathrm{d}E E^2 e^{-E/(k_{\mathrm{B}}T)}}, \tag{5.2}$$

where $N_{\mathrm{lost}} = 3$ denotes the number of atoms being lost per collision event, the factor of 3! in the denominator accounts for the indistinguishable nature of three identical particles, and E denotes the total energy of the three particles. $K_{\mathrm{shallow}}^{(J=0)}(E)$ and $K_{\mathrm{deep}}^{(J=0)}(E)$ represent the decay rate constants into the shallow dimer and deep dimers respectively at finite energies . They can be expressed in terms of universal scaling functions $s_{12}(ka)$, $s_{22}(ka)$ and $s_{11}(ka)$:

$$\begin{aligned} K_{\mathrm{shallow}}^{(J=0)} &= \frac{144\sqrt{3}\pi^2}{(ka)^4} \left(1 - \left| s_{22} + \frac{s_{12}^2 e^{2i\theta - 2\eta}}{1 - s_{11} e^{2i\theta - 2\eta}} \right|^2 - \frac{(1 - e^{-4\eta}) |s_{12}|^2}{|1 - s_{11} e^{2i\theta - 2\eta}|^2} \right) \frac{\hbar a^4}{m}, \\ K_{\mathrm{deep}}^{(J=0)} &= \frac{144\sqrt{3}\pi^2}{(ka)^4} \frac{(1 - e^{-4\eta}) \left(1 - |s_{11}|^2 - |s_{12}|^2 \right)}{|1 - s_{11} e^{2i\theta - 2\eta}|^2} \frac{\hbar a^4}{m}, \end{aligned} \tag{5.3}$$

where the momentum k is related to E through $E = \hbar^2 k^2 / m$ with the atomic mass m, and the angle θ is defined as $s_0 \ln(a/a_+)$ with $s_0 \approx 1.00624$ for three identical bosons. We only include the

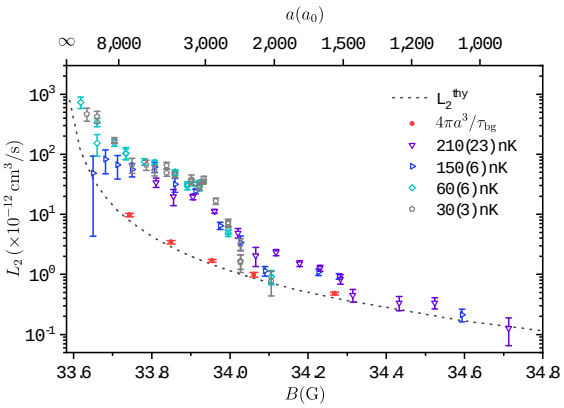

Figure 5.7: Two-body loss rate coefficient L_2 as function of B and a. The open symbols are measurements taken with pure atom samples and extracted by using fitting protocol II. These experimental points present a strong enhancement around 33.9 G (or $3000\,a_0$) and show little temperature dependence. This enhancement gradually diminishes for a below $2000\,a_0$. Solid red circles are deduced from the measured shallow dimer lifetimes τ_{bg} in the large a limit by using a model from [70]. The dashed line indicates the prediction from our refined two-body cc model on *sd* wave basis.

contribution of zero total orbital angular momentum $J = 0$ in the above equations. The numeric values of s_{ij} $(i, j = 1, 2)$ matrices are taken from [86] in the region of $0 < ka < 1$. Prior to doing the thermal averages, $K_{\text{shallow}}^{(J=0)}$ and $K_{\text{deep}}^{(J=0)}$ are smoothly extrapolated to their threshold values in the limit of $ka \to 0$ where this numerical method loses its accuracy [88]:

$$K_{\text{shallow}}^{(J=0)}(T=0) = \frac{768\pi^2(4\pi - 3\sqrt{3})\left(\sin^2\theta + \sinh^2\eta\right)}{\sinh^2(\pi s_0 + \eta) + \cos^2\theta}\frac{\hbar a^4}{m},$$
$$K_{\text{deep}}^{(J=0)}(T=0) = \frac{(3/2) \times 128\pi^2(4\pi - 3\sqrt{3})}{\sinh^2(\pi s_0)}\frac{\sinh(2\pi s_0)\sinh(2\eta)}{\sinh^2(\pi s_0 + \eta) + \cos^2\theta}\frac{\hbar a^4}{m}. \tag{5.4}$$

We use the measured temperatures of each condition as a fixed input parameter in the fit. Two free fitting parameters $a_+^{(0)}$ and η_+ which account for the location and width of the three-body recombination minimum can then be extracted. When fitting for the maximum $a_p^{(0)}$, θ is substituted with $\pi/2 + \theta$. The details of the algorithms can be found in Appx. D.

We also play with this model to further explore the role of angular momentum terms with $J \geqslant 1$ in three-body recombination into the shallow dimer. The contribution from arbitrary angular momentum J takes the form

$$K^{(J)}(E) = \frac{144\sqrt{3}\pi^2(2J+1)f_J(ka)}{(ka)^4}\frac{\hbar a^4}{m}, \tag{5.5}$$

where $f_J(ka)$ is related to the imaginary part of the atom-dimer scattering phase shift through $f_J(ka) = 1 - \exp\left(-4\,\text{Im}[\delta_{\text{AD}}^{(J)}(E)]\right)$. The numerical values of $f_J(ka)$ are provided by D. Kang. For three identical bosons, the leading term is $J = 2$. We extrapolate $f_J(ka)$ to small values of ka by using their asymptotic values according to the threshold behaviors,

$$f_J(ka) = a_J(ka)^{2\lambda_J+4} + b_J(ka)^{2\lambda_J+6}, \tag{5.6}$$

where $\lambda_1 = 3$ and $\lambda_J = J$ for $J = 2$ to 6. As presented in Fig. 5.10 panel (b), the contribution from $J \geqslant 1$ terms can even overtake the $J = 0$ term at large enough a according to this model. This observation could qualitatively explain why the second recombination minimum is completely smeared out by the finite temperature effects. This observation is consistent with an independent model given in [89].

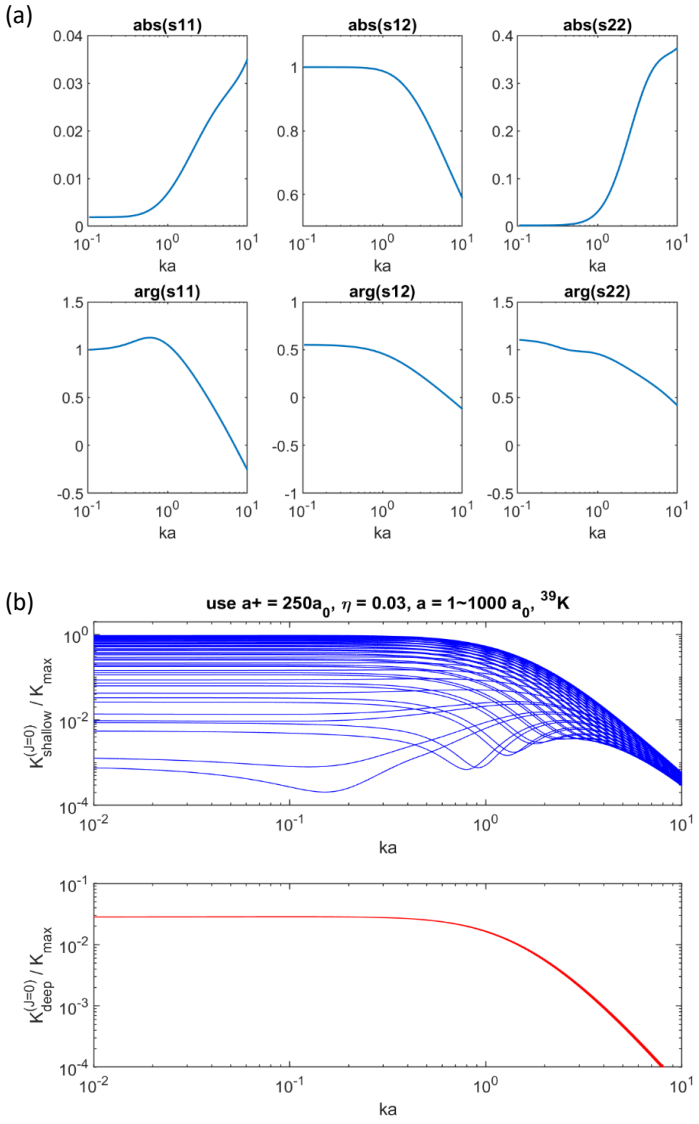

Figure 5.8: Using the S-matrix method to calculate L_3 at finite temperatures. (a) Universal scaling functions s_{12} (left) s_{22} (middle), and s_{11} (right) as functions of the product ka. The modulus $|s_{ij}|$ and the phase $\arg[s_{ij}]$ of the functions are shown in the top and the bottom panels, respectively. (b) The rescaled integrand K_{shallow} and K_{deep} in the $J = 0$ sector as defined in Eqn. 5.4. The different curves are evaluated for $a = 1 - 1000\, a_0$ as function of ka. The variance on individual K_{shallow} curves is related to the modulation due to Efimov physics. The variance on individual K_{deep} curves is much smaller and cannot be resolved on this scale.

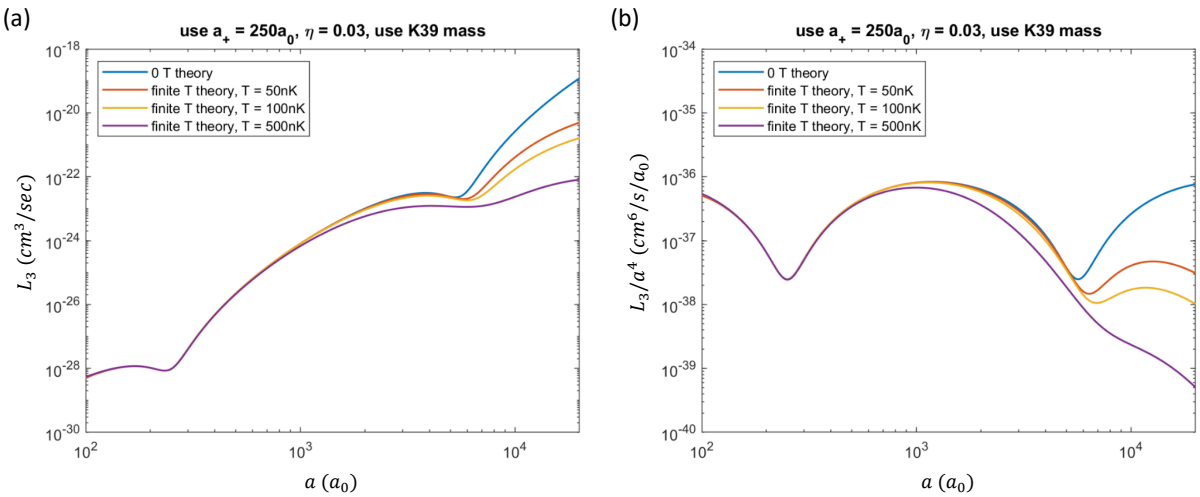

Figure 5.9: Finite-temperature model predictions for three-body recombination rate coefficient (a) $L_3^{(a>0)}$ (b) and $L_3^{(a>0)}/a^4$ in the total angular momentum $J = 0$ sector. It is worth noting that here the finite temperature effects shift the recombination minimum to higher a; contrarily the resonance peaks on $L_3^{(a<0)}$ are shifted to lower a.

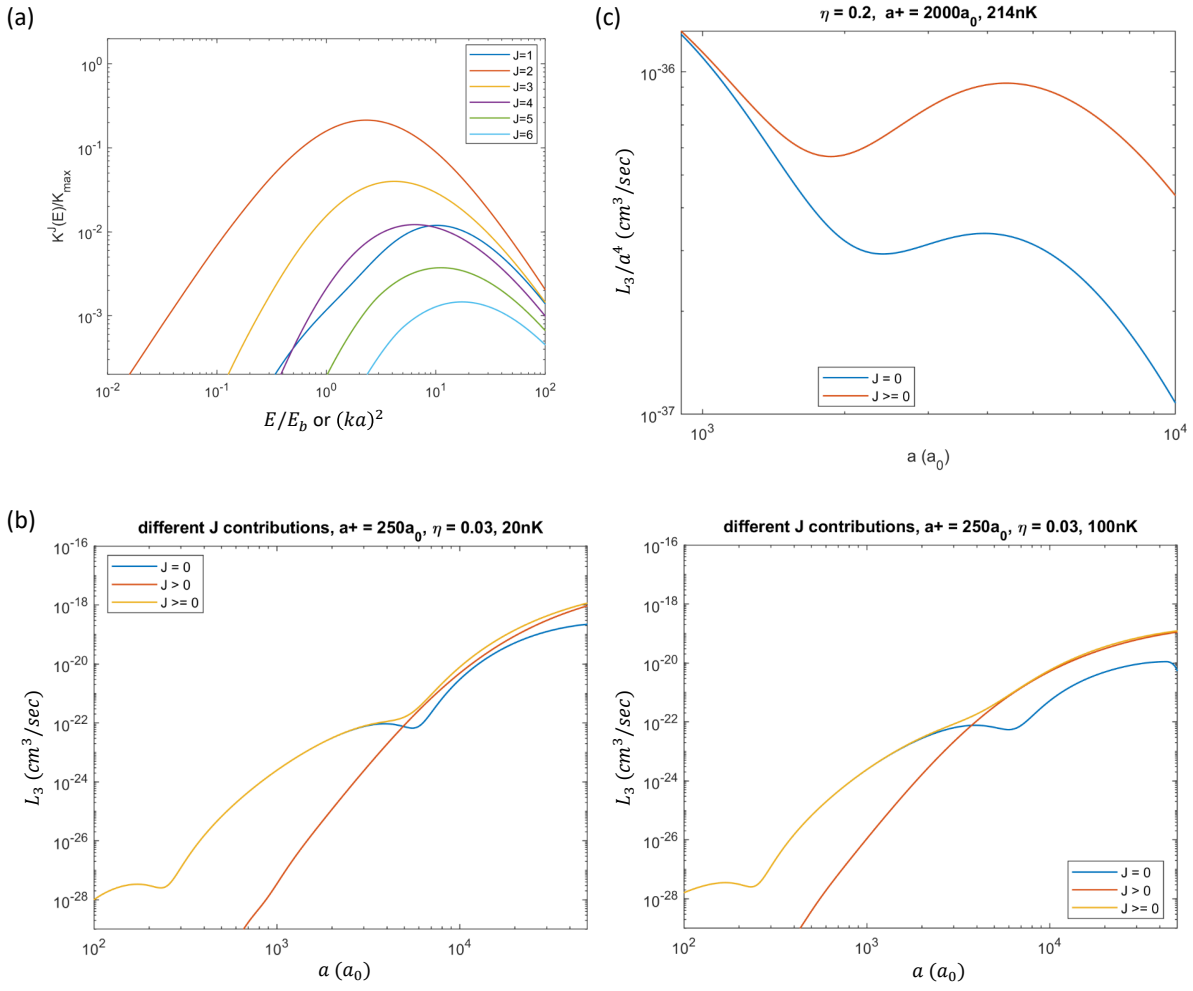

Figure 5.10: Contributions to the three-body recombination rate into the shallow dimer from angular momenta $J = 1 - 6$ (a) The rescaled integrands for $J = 1$ to 6 as function of $(ka)^2$. (b) Comparison of contributions from $J = 0$ (blue line) and $J \geqslant 1$ (red line) at 20 nK (bottom left) and 100 nK (bottom right). The yellow lines represent total loss rate with $J = 0$ to 6. (c) The effects of $J \geqslant 1$ terms tend to shift the recombination minimum to smaller a. This trend is intriguingly opposite to the finite temperature effects from the $J = 0$ term as shown in Fig. 5.9.

5.5 Analysis of Systematic Effects

We spent a tremendous effort to understand the anomalously high values of L_2 around $3000\,a_0$. Does it actually come from technical artifacts or real physics? According to a coupled-channel calculation on *sdg*-wave basis, there is no resonance-like features in this region at all as depicted in Fig. 5.11. And we already show in Section 4.1.2 that this model successfully reproduces the Feshbach molecule lifetime data without any scaling fudge factor. Both two-body loss rate L_2 and molecule one-body lifetime $\tau_{\rm bg}$ have their roots in the d-wave sector in the two-body Hamiltonian. The excellent agreement between experiment and theory on $\tau_{\rm bg}$ suggests that the enhancement on L_2 could be caused by systematic effects rather than real resonances. To summarize, the systematic effects that have been ruled out are listed as the following:

- The atom loss rate is uncorrelated with the magnetic field ramping time to/from the science field in the range of 0.5 to 50 ms.
- There is no detectable Feshbach molecule population during the loss processes.
- There is no abnormal magnetic field noise at this scattering length, as evidenced by the rf spectroscopy in Fig. 5.12.
- Increasing the trap depth by a factor of 2 does not affect the loss rate (see Fig. 5.13 (a)). The initial temperature and density of the cloud generated in these two traps are delicately kept the same (Fig. 5.13 (b)).
- The frequency difference between two ODT beams (vertical and horizontal) does not play a role. The frequency difference is to prevent interference pattern between the two beams.
- We do frequency and amplitude modulations on the two ODT beams to purposely enlarge the technical noises on the ODT frequency and intensity. This experiment shown in Fig. 5.14 rules out any Raman-type two-photon transitions in which two free atoms are associated into Feshbach molecules which are then lost from the trap via subsequent collisions with other atoms.

Interestingly, none of the above technical concerns appears to be correlated to the two-body loss peak that we have observed around $3000\,a_0$.

Another systematic effect that has been frequently suspected in previous experiments [90, 91, 92] but never resolved in a quantitative way [93, 94, 87, 95] is the so-called avalanche effect. An avalanche effect is hypothesized to happen at large a's where the E_b of the shallow dimers is small compared to the trap depth. The released energy on one of the recombination products, shallow dimers, is not high enough for them to escape the trap. The remaining shallow dimers will then collide with free atoms with a relatively large (in)elastic cross section at a small relative momentum. These secondary inelastic collisions can lead to extra loss of atoms hence modify the population decay vs. hold time in a sophisticated way. These shallow dimers could in fact only exist in the trap for a transient amount of time thus evade regular detection methods. Or their population could be just too small to be observed.

We introduce a toy model to emulate the effects of secondary collisions between shallow dimers and atoms. We use empirical values on the atom-dimer relaxation rate constant β_{AD} and theoretical values on K_2 in the following coupled rate equations

$$\begin{aligned}
\frac{dn_{\mathrm{A}}}{dt} &= -3\left(K_3^{\mathrm{deep}} + K_3^{\mathrm{shallow}}\right) n_{\mathrm{A}}^3 - 2K_2^{\mathrm{theory}} n_{\mathrm{A}}^2 - \beta_{\mathrm{AD}} n_{\mathrm{D}} n_{\mathrm{A}} - \alpha n_{\mathrm{A}}, \\
\frac{dn_{\mathrm{D}}}{dt} &= 3K_3^{\mathrm{shallow}} n_{\mathrm{A}}^3 - \beta_{\mathrm{AD}} n_{\mathrm{D}} n_{\mathrm{A}} - \frac{n_{\mathrm{D}}}{\tau_{\mathrm{bg}}}.
\end{aligned} \tag{5.7}$$

The predicted decay curves by these rate equations are plotted in Fig. 5.15 and compared to our data. This model can indeed grasp the formation of shallow dimers at the early stage of the three-body recombination process. And these shallow dimers decay away very quickly by reacting with the atoms. However, the population of these shallow dimers is not large enough to lead to persistent atom number losses at long hold times.

Although the toy model seems to suggest a negligible role of the existence of shallow dimers in the trap, it is too primitive to completely rule out their effects in the kinetics of the atoms. A Monte Carlo simulation such as in [94, 87] will be needed to take into full account the energy dependent atom-dimer (in)elastic collision cross section as well as the trajectories of the atoms and

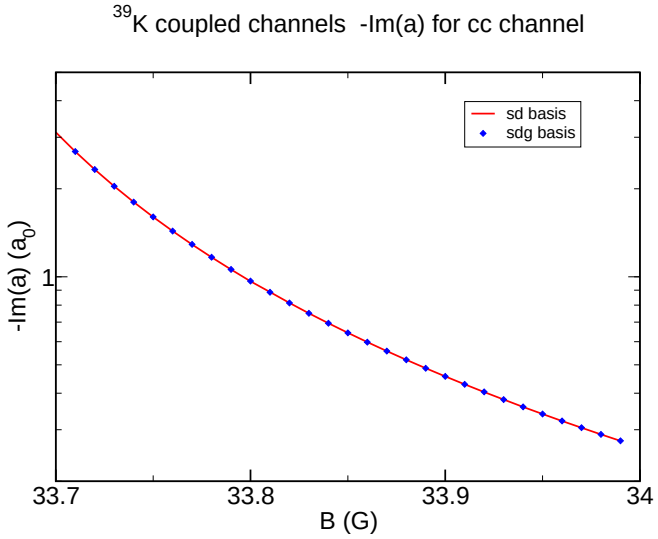

Figure 5.11: A coupled-channel calculation of $-\mathrm{Im}(a)$ in *sdg*-wave basis near 34 G. The numerics are provided by P. S. Julienne.

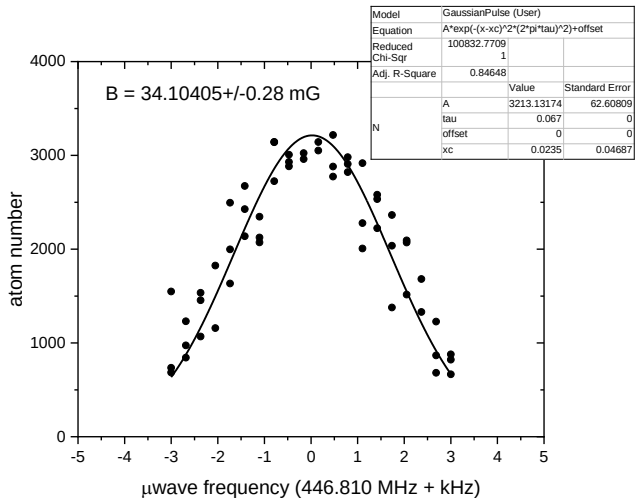

Figure 5.12: Rf lineshape for the $|1,-1\rangle \rightarrow |2,0\rangle$ transition at around $2000\,a_0$. The fitting function is shown in the inset table. The r.m.s. width of the Gaussian pulse is fixed to the set value of 67 μs in temporal domain.

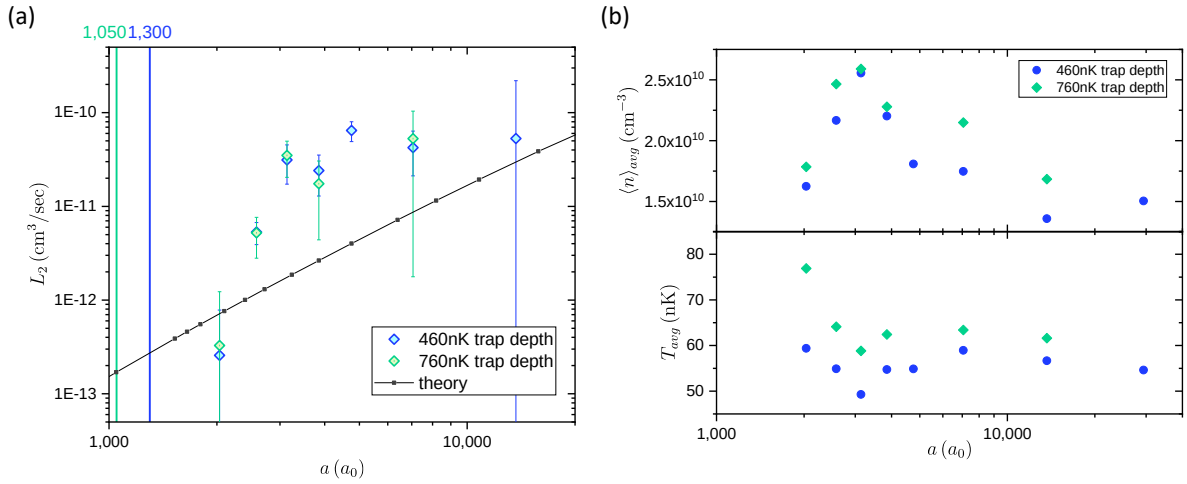

Figure 5.13: Vary the trap depth in three-body recombination experiment at large a. (a) Two different trap depths give essentially the same result on L_2. The vertical lines indicate the scattering lengths at which E_b is equal to the trap depth. (b) The time-averaged conditions of the samples generated in two trap depths are controlled to be about the same.

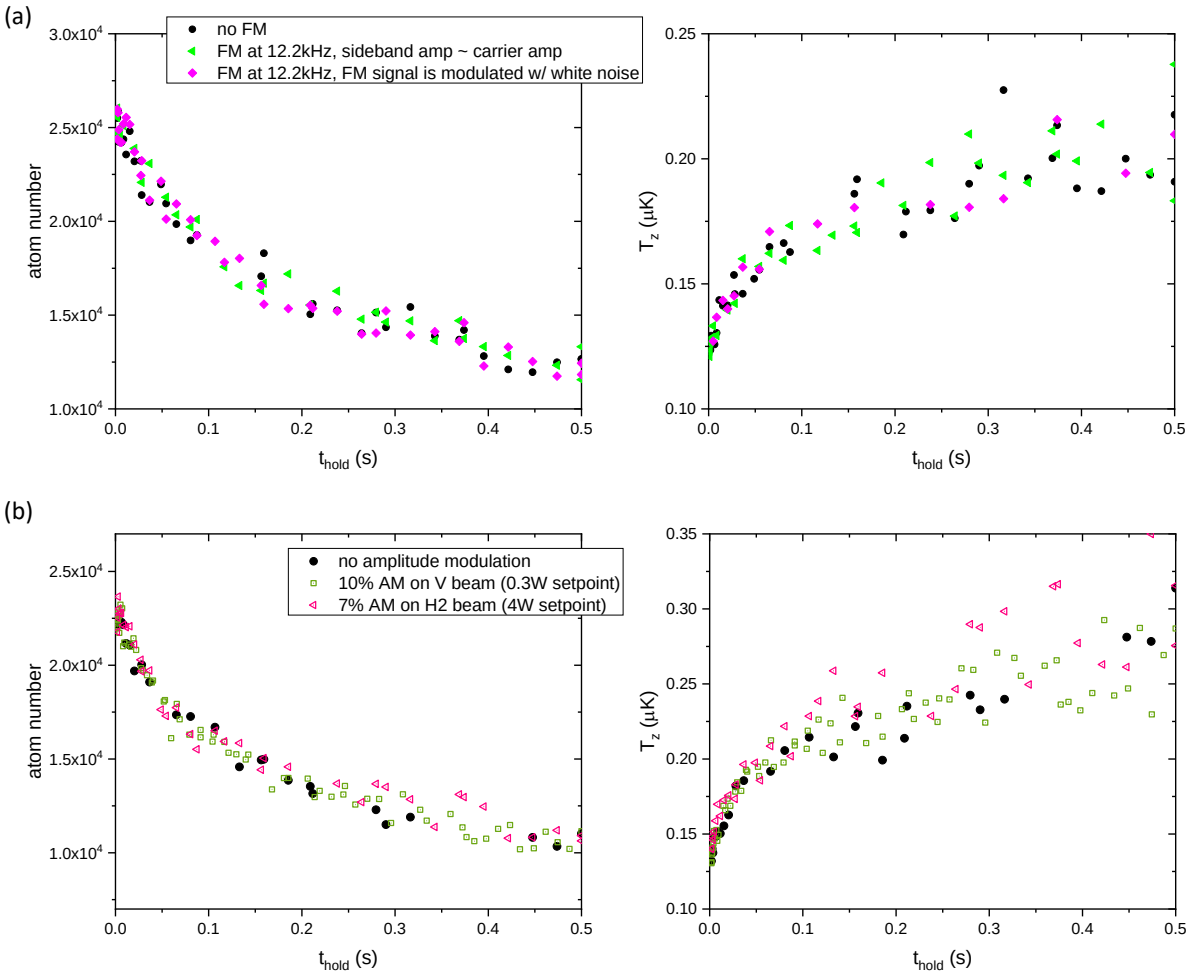

Figure 5.14: Frequency (a) and intensity (b) modulation on the ODT beams, initial temperature 120 nK, science field 3000 a_0. In (a), we modulate the frequency of the ODT at a single frequency of $E_b = 12.2\,\text{kHz}$, as well as in a broad-band fashion respectively. In (b), we modulation the intensity of two ODT beams at frequency of $E_b = 12.2\,\text{kHz}$ up to a modulation index of 10%. Black circles represent loss data without any modulations. None of these modulations enhances the number losses or heating rates.

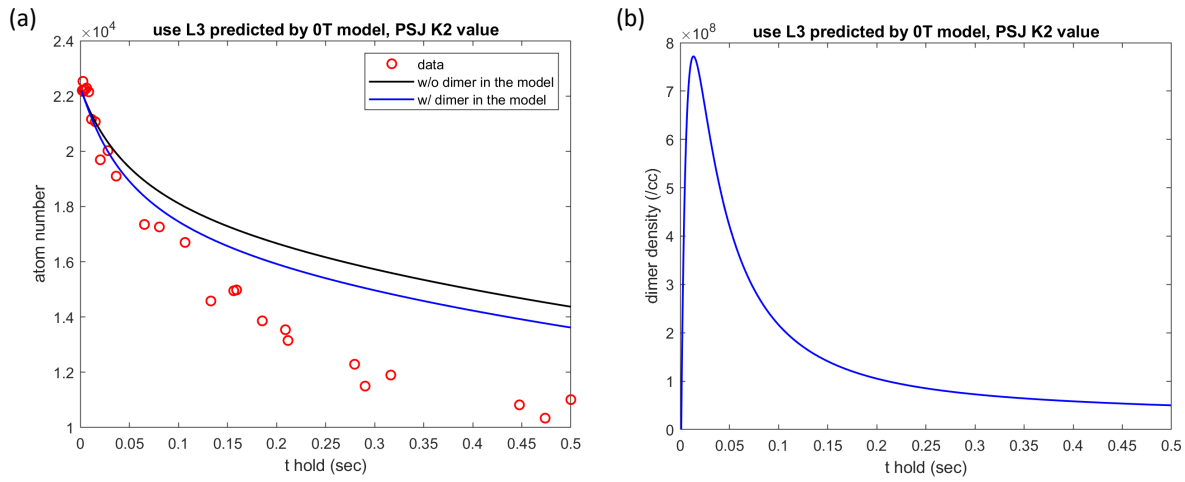

Figure 5.15: Comparison of three-body recombination data with the predictions by a toy model that includes avalanche effects. The time-averaged temperature is 200 nK and the science field is $3000\,a_0$. The black line represents three-body recombination assuming that the shallow dimers all leave the trap immediately. The blues lines represent atom population (a) and shallow dimer population (b) assuming that the shallow dimers all remain in the trap after being created.

dimers in the trap with a finite depth.

Chapter 6

Summary and Outlook

6.1 Fifty Years of Efimov Physics

Recent decades have witnessed tremendous progress in the field of few-body physics. This burgeoning field has been meanwhile motivating both technical and computational developments in ultracold atoms. We dedicate our work to improving the experimental precision on two- and three-body observables as well as to characterizing the systematic effects that have been previously neglected. Our goal is to set a technical standard for the studies of few-body physics with ultracold atoms. Comparison of our work with generic few-body models can be made along two independent axes of magnetic field and collision energy respectively. As regards physics, we emphasize the global picture of Efimov's scenario by connecting the three-body observables in the $a < 0$ and $a > 0$ regions together. Within a very limited universal window as illustrated in Fig. 3.13, we are able to observe signatures of Efimovs's original zero-range results manifested in ^{39}K in the vicinity of an intermediate-strength Feshbach resonance.

All the measured three-body observables in our work are summarized in Table 6.1 and compared to theoretical models of various layers of complexity. The two ratios $a_*^{(1)}/|a_-^{(0)}|$ and $a_*^{(1)}/(a_p^{(0)}$ which lie inside the universal window agree with the zero-range results within the experimental uncertainties. The width parameters associated with each location – $\eta_-^{(0)}$, $\eta_*^{(1)}$ and $\eta_+^{(0)}$ – are found to be consistent with each other. This discovery for the first time verifies another hypothesis in zero-range theory which is the continuity of a three-body short-range parameter across the pole of the Feshbach resonance [96]. As discussed in 3.2.3, these zero-range universal ratios come from a

combined effect of 1) an enlarged universal window and 2) an especially large value of $|a_{-}^{(0)}|/r_{\mathrm{rdW}}$ that is unique to ^{39}K. The former effect is a consequence of a small effective range parameter r_e in a two-channel effective field theory [15]. As to the absolute locations of the three-body observables, we demonstrate in ^{39}K that two-body van der Waals potentials alone can describe the three-body physics in the intermediate coupling strength regime if hyperfine interactions are properly incorporated.

	Observables for $a<0$			Observables for $a>0$				Efimov's ratios		
Model	$a_-^{(0)}/a_0$	$\eta_-^{(0)}$	$a_*^{(1)}/a_0$	$\eta_*^{(1)}$	$a_+^{(0)}/a_0$	$\eta_+^{(0)}$	$a_p^{(0)}$	$a_*^{(1)}/\lvert a_-^{(0)}\rvert$	$a_+^{(0)}/\lvert a_-^{(0)}\rvert$	$a_p^{(0)}/\lvert a_-^{(0)}\rvert$
zero-range EFT [53]				–				1.06522	0.209914	1
sc vdW [97]	−626(9)	–	215	–	91	–	–	0.34	0.14	–
mc vdW [18] [69]	−846(19)	0.21(1)								
Experimental	−908(11)	0.25(1)	884(14)	0.28(2)	246(6)	0.20(2)	876(28)	0.97(2)	0.271(7)	0.96(3)

Table 6.1: Summary of three-body observables characterizing the Efimov spectrum in ^{39}K across the Feshbach resonance at 33.58 G. The locations of the three-body observables and their ratios are compared to theoretical models of various layers of complexity.

6.2 Future Directions

If one contrasts the summary figures Fig. 3.12 and Fig. 3.14, the three-body observables are noticeably not as well sampled for $a > 0$ as in the $a < 0$ region. This relatively less-explored region opens up a lot of opportunities for future few-body physics studies in both homonuclear and heteronuclear systems. Interplay between atoms and Feshbach molecules as well as between two Feshbach molecules in this region present technical challenges in quantum state preparation and control of noise.

Feshbach resonances with intermediate and small coupling strengths provide another interesting direction. In [18], we demonstrate a tri-atomic resonance in ^{39}K that deviates from van der Waals universality. This observed trend seems to agree with a two-channel field theory in which three-body observables are predicted to be linked with $s_{\rm res}$ (or equivalently the two-body scattering effective range r_e) [15, 24]. Nevertheless, two independent groups have reported that in ^{7}Li, which also features an intermediate $s_{\rm res}$, the tri-atomic resonances $|a_-^{(0)}| \simeq 9\, r_{\rm vdW}$ are in perfect agreement with van der Waals universality [98, 99]. This brings up the question of what other elements are contributing to three-body physics in addition to the effective range. A three-body multi-channel calculation may shed light on this interesting case. For sufficiently narrow Feshbach resonances with $s_{\rm res} \ll 1$, it has been proposed that a novel kind of universality exists in which the three-body observables are related to the Feshbach resonance range parameter r^* [100]. Such narrow resonances can be found in species such as ^{23}Na and ^{87}Rb. It will also be enlightening to see if the multi-channel calculations based on van der Waals potentials can still do a good job in this regime.

Last but not least, ongoing cold atom projects in microgravity environment provide a promising and novel tool to unveil the few-body dynamics near the pole of the Feshbach resonance. Explorations on this regime have been inhibited by the finite density and temperature effects for the experiments on earth. And a large magnetic field gradient is usually needed to levitate the cloud in a shallow trap [101]. As I am concluding my thesis, tremendous progress has been made in gener-

ating atom samples at record-breaking low temperatures in space station. There is vision that one could make use of these low-temperature and low-density samples to make accurate observations of the first excited Efimov tri-atomic resonance and locate $a_{-}^{(1)}$.

Bibliography

[1] Michael E. Fisher. Renormalization group theory: Its basis and formulation in statistical physics. Rev. Mod. Phys., 70:653–681, Apr 1998.

[2] Kenneth G. Wilson. The renormalization group and critical phenomena. Rev. Mod. Phys., 55:583–600, Jul 1983.

[3] Jun John Sakurai. Modern quantum mechanics; rev. ed. Addison-Wesley, Reading, MA, 1994.

[4] Private communications with Paul S. Julienne.

[5] George A. Baker Jr. The MBX challenge competition: a neutron matter model. Int. J. Mod. Phys. B, 15:1314–1320, 1999.

[6] Tin-Lun Ho. Universal thermodynamics of degenerate quantum gases in the unitarity limit. Phys. Rev. Lett., 92:090402, Mar 2004.

[7] P. Makotyn, C. E. Klauss, D. L. Goldberger, E. A. Cornell, and D. S. Jin. Universal dynamics of a degenerate unitary bose gas. Nature Physics, 10(2):116–119, 2014.

[8] John Corson. Dynamics of Quenched Ultracold Quantum Gases. PhD thesis, Boulder, CO, 2016-07 2016.

[9] V. Efimov. Low-energy properties of three resonantly interacting particles. Sov. J. Nucl. Phys, 29(4):1058–1069, 1979.

[10] L. H. Thomas. The interaction between a neutron and a proton and the structure of H^3. Phys. Rev., 47:903–909, Jun 1935.

[11] José P D'Incao, Chris H Greene, and B D Esry. The short-range three-body phase and other issues impacting the observation of efimov physics in ultracold quantum gases. Journal of Physics B: Atomic, Molecular and Optical Physics, 42(4):044016, feb 2009.

[12] M. Berninger, A. Zenesini, B. Huang, W. Harm, H.-C. Nägerl, F. Ferlaino, R. Grimm, P. S. Julienne, and J. M. Hutson. Universality of the three-body parameter for Efimov states in ultracold cesium. Phys. Rev. Lett., 107:120401, Sep 2011.

[13] Jia Wang, J. P. D'Incao, B. D. Esry, and Chris H. Greene. Origin of the three-body parameter universality in Efimov physics. Phys. Rev. Lett., 108:263001, Jun 2012.

[14] C. Chin. Universal scaling of Efimov resonance positions in cold atom systems. arXiv:1111.1484, 2011.

[15] R. Schmidt, S.P. Rath, and W. Zwerger. Efimov physics beyond universality. The European Physical Journal B, 85(11):386, Nov 2012.

[16] José P. D'Incao, J. Wang, Brett Esry, and Chris Greene. The universality of the Efimov three-body parameter. Few-Body Systems, 54, Nov 2012.

[17] Yujun Wang and Paul S. Julienne. Universal van der Waals physics for three cold atoms near Feshbach resonances. Nature Physics, 10:768, Aug 2014.

[18] Roman Chapurin, Xin Xie, Michael J. Van de Graaff, Jared S. Popowski, José P. D'Incao, Paul S. Julienne, Jun Ye, and Eric A. Cornell. Precision test of the limits to universality in few-body physics. Phys. Rev. Lett., 123:233402, Dec 2019.

[19] B. M. Axilrod and E. Teller. Interaction of the van der Waals type between three atoms. J. Chem. Phys., 11:299, Jun 1943.

[20] William D. Phillips. Nobel lecture: Laser cooling and trapping of neutral atoms. Rev. Mod. Phys., 70:721–741, Jul 1998.

[21] Harold J. Metcalf and Peter van der Straten. Laser Cooling and Trapping. Springer-Verlag, New York, 1999.

[22] N. F. Mott and Harrie Stewart Wilson Massey. The theory of atomic collisions. 1949.

[23] John L. Bohn, James P. Burke, Chris H. Greene, H. Wang, P. L. Gould, and W. C. Stwalley. Collisional properties of ultracold potassium: Consequences for degenerate bose and fermi gases. Phys. Rev. A, 59:3660–3664, May 1999.

[24] Christian Langmack, Richard Schmidt, and Wilhelm Zwerger. Efimov states near a Feshbach resonance and the limits of van der Waals universality at finite background scattering length. Phys. Rev. A, 97:033623, Mar 2018.

[25] E. Nielsen, D.V. Fedorov, A.S. Jensen, and E. Garrido. The three-body problem with short-range interactions. Physics Reports, 347(5):373 – 459, 2001.

[26] Rabin Paudel. Probing local quantities in a strongly interacting Fermi gas and the construction of an ultracold Fermi gas apparatus. PhD thesis, Boulder, CO, 2017-05 2017.

[27] Roman Chapurin. Precise Measurements of Few-Body Physics in Ultracold ^{39}K Bose Gas. PhD thesis, Boulder, 2019-06 2019.

[28] G. Salomon, L. Fouché, P. Wang, A. Aspect, P. Bouyer, and T. Bourdel. Gray-molasses cooling of ^{39}K to a high phase-space density. EPL (Europhysics Letters), 104(6):63002, Dec 2013.

[29] G. Salomon, L. Fouché, S. Lepoutre, A. Aspect, and T. Bourdel. All-optical cooling of ^{39}K to Bose-Einstein condensation. Phys. Rev. A, 90:033405, Sep 2014.

[30] Dipankar Nath, R Kollengode Easwaran, G. Rajalakshmi, and C. S. Unnikrishnan. Quantum-interference-enhanced deep sub-Doppler cooling of ^{39}K atoms in gray molasses. Phys. Rev. A, 88:053407, Nov 2013.

[31] M. Gröbner, P. Weinmann, F. Meinert, K. Lauber, E. Kirilov, and H.-C. Nägerl. A new quantum gas apparatus for ultracold mixtures of K and Cs and KCs ground-state molecules. Journal of Modern Optics, 63(18):1829–1839, 2016.

[32] Jacob Covey. Enhanced optical and electric manipulation of a quantum gas of KRb molecules. PhD thesis, Boulder, 2017-07 2017.

[33] L. De Sarlo, P. Maioli, G. Barontini, J. Catani, F. Minardi, and M. Inguscio. Collisional properties of sympathetically cooled ^{39}K. Phys. Rev. A, 75:022715, Feb 2007.

[34] Robert L. D. Campbell, Robert P. Smith, Naaman Tammuz, Scott Beattie, Stuart Moulder, and Zoran Hadzibabic. Efficient production of large ^{39}K Bose-Einstein condensates. Phys. Rev. A, 82:063611, Dec 2010.

[35] S. J. M. Kuppens, K. L. Corwin, K. W. Miller, T. E. Chupp, and C. E. Wieman. Loading an optical dipole trap. Phys. Rev. A, 62:013406, Jun 2000.

[36] Nicolas Schlosser, Georges Reymond, Igor Protsenko, and Philippe Grangier. Sub-poissonian loading of single atoms in a microscopic dipole trap. Nature, 411(6841):1024–1027, 2001.

[37] T. Grünzweig, A. Hilliard, M. McGovern, and M. F. Andersen. Near-deterministic preparation of a single atom in an optical microtrap. Nature Physics, 6(12):951–954, 2010.

[38] Bruce H. Karnopp. Introduction to Dynamics. Addison-Wesley, Reading, MA, 1974.

[39] L. Richter, H. Mandelberg, M. Kruger, and P. McGrath. Linewidth determination from self-heterodyne measurements with subcoherence delay times. IEEE Journal of Quantum Electronics, 22(11):2070–2074, 1986.

[40] Hanne Ludvigsen, Mika Tossavainen, and Matti Kaivola. Laser linewidth measurements using self-homodyne detection with short delay. Optics Communications, 155(1):180 – 186, 1998.

[41] L. B. Mercer. 1/f frequency noise effects on self-heterodyne linewidth measurements. Journal of Lightwave Technology, 9(4):485–493, 1991.

[42] G. Reinaudi, T. Lahaye, Z. Wang, and D. Guéry-Odelin. Strong saturation absorption imaging of dense clouds of ultracold atoms. Opt. Lett., 32(21):3143–3145, Nov 2007.

[43] D Genkina, L M Aycock, B K Stuhl, H-I Lu, R A Williams, and I B Spielman. Feshbach enhanceds-wave scattering of fermions: direct observation with optimized absorption imaging. New Journal of Physics, 18(1):013001, Dec 2015.

[44] Joseph W Goodman. Introduction to Fourier optics. Roberts & Co. Publishers, Englewood, CO, 2005.

[45] Chen-Lung Hung and Cheng Chin. *In Situ* Imaging of Atomic Quantum Gases, chapter Chapter 6, pages 101–120.

[46] Max Born and Emil Wolf. Principles of Optics: Electromagnetic Theory of Propagation, Interference and Diffraction of Light (7th Edition). Cambridge University Press, 7th edition, 1999.

[47] Ryuta Yamamoto, Jun Kobayashi, Kohei Kato, Takuma Kuno, Yuto Sakura, and Yoshiro Takahashi. Site-resolved imaging of single atoms with a Faraday quantum gas microscope. Phys. Rev. A, 96:033610, Sep 2017.

[48] S. Kadlecek, J. Sebby, R. Newell, and T. G. Walker. Nondestructive spatial heterodyne imaging of cold atoms. Opt. Lett., 26(3):137–139, Feb 2001.

[49] Erin Marshall Seroka, Ana Valdés Curiel, Dimitrios Trypogeorgos, Nathan Lundblad, and Ian B. Spielman. Repeated measurements with minimally destructive partial-transfer absorption imaging. Opt. Express, 27(25):36611–36624, Dec 2019.

[50] Eric Braaten and H.-W. Hammer. Universality in few-body systems with large scattering length. Physics Reports, 428(5):259 – 390, 2006.

[51] Francesca Ferlaino and Rudolf Grimm. Forty years of efimov physics: How a bizarre prediction turned into a hot topic. Physics, 3(9), 2010.

[52] Pascal Naidon and Shimpei Endo. Efimov physics: a review. Reports on Progress in Physics, 80(5):056001, Mar 2017.

[53] José P D'Incao. Few-body physics in resonantly interacting ultracold quantum gases. Journal of Physics B: Atomic, Molecular and Optical Physics, 51(4):043001, Jan 2018.

[54] Cheng Chin, Rudolf Grimm, Paul Julienne, and Eite Tiesinga. Feshbach resonances in ultracold gases. Rev. Mod. Phys., 82(2):1225, 2010.

[55] Richard Schmidt. From few- to many-body physics with ultracold atoms. PhD thesis, München, 2013.

[56] Private communications with Wilhelm Zwerger.

[57] Eugene P. Wigner. Lower limit for the energy derivative of the scattering phase shift. Phys. Rev., 98:145–147, Apr 1955.

[58] H.-W. Hammer and Dean Lee. Causality and the effective range expansion. Annals of Physics, 325(10):2212 – 2233, 2010.

[59] V. N. Efimov. Weakly bound states of three resonantly interacting particles. Yadern. Fiz., 12:1080–91, Nov 1970.

[60] V. Efimov. Energy levels arising from resonant two-body forces in a three-body system. Physics Letters B, 33(8):563 – 564, 1970.

[61] Private communications with Pascal Naidon.

[62] B. D. Esry, Chris H. Greene, and James P. Burke. Recombination of three atoms in the ultracold limit. Phys. Rev. Lett., 83:1751–1754, Aug 1999.

[63] T. Kraemer, M. Mark, P. Waldburger, J. G. Danzl, C. Chin, B. Engeser, A. D. Lange, K. Pilch, A. Jaakkola, H.-C. Nägerl, and R. Grimm. Evidence for Efimov quantum states in an ultracold gas of caesium atoms. Nature, 440:315, Mar 2006.

[64] P. F. Bedaque, H.-W. Hammer, and U. van Kolck. The three-boson system with short-range interactions. Nuclear Physics A, 646(4):444 – 466, 1999.

[65] Ludwig W. Bruch and Katuro Sawada. Inequality relating the ground-state energies of two and three bosons. Phys. Rev. Lett., 30:25–27, Jan 1973.

[66] K. Helfrich, H.-W. Hammer, and D. S. Petrov. Three-body problem in heteronuclear mixtures with resonant interspecies interaction. Phys. Rev. A, 81:042715, Apr 2010.

[67] Private communications with Richard Schmidt.

[68] Frederick H. Mies, Carl J. Williams, Paul S. Julienne, and Morris Krauss. Estimating bounds on collisional relaxation rates of spin-polarized ^{87}Rb atoms at ultracold temperatures. Journal of research of the National Institute of Standards and Technology, 101(4):521–535, 1996.

[69] Xin Xie *et al*, in preparation.

[70] Thorsten Köhler, Eite Tiesinga, and Paul S. Julienne. Spontaneous dissociation of long-range Feshbach molecules. Phys. Rev. Lett., 94:020402, Jan 2005.

[71] C. Strauss, T. Takekoshi, F. Lang, K. Winkler, R. Grimm, J. Hecker Denschlag, and E. Tiemann. Hyperfine, rotational, and vibrational structure of the $a^3\Sigma_u^+$ state of $^{87}Rb_2$. Phys. Rev. A, 82:052514, Nov 2010.

[72] S. Knoop, F. Ferlaino, M. Mark, M. Berninger, H. Schöbel, H.-C. Nägerl, and R. Grimm. Observation of an Efimov-like trimer resonance in ultracold atom-dimer scattering. Nature Physics, 5:227, Feb 2009.

[73] A. Zenesini, B. Huang, M. Berninger, H.-C. Nägerl, F. Ferlaino, and R. Grimm. Resonant atom-dimer collisions in cesium: Testing universality at positive scattering lengths. Phys. Rev. A, 90:022704, Aug 2014.

[74] K. Helfrich and H.-W. Hammer. Resonant atom-dimer relaxation in ultracold atoms. EPL (Europhysics Letters), 86(5):53003, Jun 2009.

[75] K. Kato, Yujun Wang, J. Kobayashi, P. S. Julienne, and S. Inouye. Isotopic shift of atom-dimer efimov resonances in K-Rb mixtures: Critical effect of multichannel Feshbach physics. Phys. Rev. Lett., 118:163401, Apr 2017.

[76] Private communications with Dmitry Petrov.

[77] Benno Rem, Andrew Grier, Igor Ferrier-Barbut, U Eismann, Tim Langen, N Navon, Lev Khaykovich, F Werner, D Petrov, F Chevy, and C. Salomon. Lifetime of the bose gas with resonant interactions. Phys. Rev. Lett., 110:163202, Apr 2013.

[78] Eric Braaten and H.-W. Hammer. Enhanced dimer relaxation in an atomic and molecular Bose-Einstein condensate. Phys. Rev. A, 70:042706, Oct 2004.

[79] Cheng Chin, Andrew Kerman, Vladan Vuletic, and Steven Chu. Sensitive detection of cold cesium molecules formed on Feshbach resonances. Phys. Rev. Lett., 90:033201, Feb 2003.

[80] Cheng Chin and Rudolf Grimm. Thermal equilibrium and efficient evaporation of an ultracold atom-molecule mixture. Physical Review A, 69:33612, Mar 2004.

[81] Jens Herbig, Tobias Kraemer, Michael Mark, Tino Weber, Cheng Chin, Hanns-Christoph Nägerl, and Rudolf Grimm. Preparation of a pure molecular quantum gas. Science (New York, N.Y.), 301:1510–3, Oct 2003.

[82] José P. D'Incao, Javier von Stecher, and Chris Greene. Universal four-boson states in ultracold molecular gases: Resonant Effects in dimer-dimer collisions. Phys. Rev. Lett., 103:033004, Jul 2009.

[83] Sébastien Laurent, Xavier Leyronas, and Frédéric Chevy. Momentum distribution of a dilute unitary bose gas with three-body losses. Phys. Rev. Lett., 113:220601, Nov 2014.

[84] P. O. Fedichev, M. W. Reynolds, and G. V. Shlyapnikov. Three-body recombination of ultracold atoms to a weakly bound s level. Phys. Rev. Lett., 77:2921–2924, Sep 1996.

[85] Benno Rem. The Road to the Unitary Bose Gas. PhD thesis, Paris, 2013-12.

[86] Eric Braaten, H.-W. Hammer, Daekyoung Kang, and Lucas Platter. Three-body recombination of identical bosons with a large positive scattering length at nonzero temperature. Phys. Rev. A, 78:043605, Oct 2008.

[87] Christian Langmack, D. Hudson Smith, and Eric Braaten. Avalanche mechanism for the enhanced loss of ultracold atoms. Phys. Rev. A, 87:023620, Feb 2013.

[88] Private communications with Daekyoung Kang.

[89] J. P. D'Incao, H. Suno, and B. D. Esry. Limits on universality in ultracold three-boson recombination. Phys. Rev. Lett., 93:123201, Sep 2004.

[90] M. Zaccanti, B. Deissler, C. D'Errico, M. Fattori, M. Jona-Lasinio, S. Müller, G. Roati, M. Inguscio, and G. Modugno. Observation of an Efimov spectrum in an atomic system. Nature Physics, 5:586, Jul 2009.

[91] Scott E. Pollack, Daniel Dries, and Randall G. Hulet. Universality in three- and four-body bound states of ultracold atoms. Science, 326(5960):1683–1685, 2009.

[92] Olga Machtey, Zav Shotan, Noam Gross, and Lev Khaykovich. Association of Efimov trimers from a three-atom continuum. Phys. Rev. Lett., 108:210406, May 2012.

[93] Olga Machtey, David A. Kessler, and Lev Khaykovich. Universal dimer in a collisionally opaque medium: Experimental observables and Efimov resonances. Phys. Rev. Lett., 108:130403, Mar 2012.

[94] Christian Langmack, D. Hudson Smith, and Eric Braaten. Avalanche mechanism for atom loss near an atom-dimer Efimov resonance. Phys. Rev. A, 86:022718, Aug 2012.

[95] Christian Langmack, D. Hudson Smith, and Eric Braaten. Atom loss resonances in a Bose-Einstein condensate. Phys. Rev. Lett., 111:023003, Jul 2013.

[96] Eric Braaten and H Hammer. Three-body recombination into deep bound states in a bose gas with large scattering length. Phys. Rev. Lett., 87:160407, Oct 2001.

[97] Paul M. A. Mestrom, Jia Wang, Chris H. Greene, and José P. D'Incao. Efimov–van der Waals universality for ultracold atoms with positive scattering lengths. Phys. Rev. A, 95:032707, Mar 2017.

[98] P. Dyke, S. E. Pollack, and R. G. Hulet. Finite-range corrections near a Feshbach resonance and their role in the Efimov effect. Phys. Rev. A, 88:023625, Aug 2013.

[99] Noam Gross, Zav Shotan, Servaas Kokkelmans, and Lev Khaykovich. Nuclear-spin-independent short-range three-body physics in ultracold atoms. Phys. Rev. Lett., 105:103203, Sep 2010.

[100] D. S. Petrov. Three-boson problem near a narrow Feshbach resonance. Phys. Rev. Lett., 93:143201, Sep 2004.

[101] Bo Huang, Leonid A. Sidorenkov, Rudolf Grimm, and Jeremy M. Hutson. Observation of the second triatomic resonance in Efimov's scenario. Phys. Rev. Lett., 112:190401, May 2014.

[102] T. Mukaiyama, J. R. Abo-Shaeer, K. Xu, J. K. Chin, and W. Ketterle. Dissociation and decay of ultracold sodium molecules. Phys. Rev. Lett., 92:180402, May 2004.

[103] Peter Staanum, Stephan D. Kraft, Jörg Lange, Roland Wester, and Matthias Weidemüller. Experimental investigation of ultracold atom-molecule collisions. Phys. Rev. Lett., 96:023201, Jan 2006.

[104] N. Zahzam, T. Vogt, M. Mudrich, D. Comparat, and P. Pillet. Atom-molecule collisions in an optically trapped gas. Phys. Rev. Lett., 96:023202, Jan 2006.

[105] N. Syassen, T. Volz, S. Teichmann, S. Dürr, and G. Rempe. Collisional decay of ^{87}Rb Feshbach molecules at 1005.8 G. Phys. Rev. A, 74:062706, Dec 2006.

[106] F. Ferlaino, S. Knoop, M. Mark, M. Berninger, H. Schöbel, H.-C. Nägerl, and R. Grimm. Collisions between tunable halo dimers: Exploring an elementary four-body process with identical bosons. Phys. Rev. Lett., 101:023201, Jul 2008.

[107] Shuta Nakajima, Munekazu Horikoshi, Takashi Mukaiyama, Pascal Naidon, and Masahito Ueda. Nonuniversal Efimov atom-dimer resonances in a three-component mixture of ^{6}Li. Phys. Rev. Lett., 105:023201, Jul 2010.

[108] T. Lompe, T. B. Ottenstein, F. Serwane, K. Viering, A. N. Wenz, G. Zürn, and S. Jochim. Atom-dimer scattering in a three-component fermi gas. Phys. Rev. Lett., 105:103201, Sep 2010.

[109] Ruth S. Bloom, Ming-Guang Hu, Tyler D. Cumby, and Deborah S. Jin. Tests of universal three-body physics in an ultracold bose-fermi mixture. Phys. Rev. Lett., 111:105301, Sep 2013.

[110] Ming-Guang Hu, Ruth S. Bloom, Deborah S. Jin, and Jonathan M. Goldwin. Avalanche-mechanism loss at an atom-molecule efimov resonance. Phys. Rev. A, 90:013619, Jul 2014.

[111] S Knoop, F Ferlaino, M Berninger, M Mark, H-C Nägerl, and R Grimm. Observation of an Efimov resonance in an ultracold mixture of atoms and weakly bound dimers. Journal of Physics: Conference Series, 194(1):012064, Nov 2009.

[112] Eric Braaten and H.-W. Hammer. Resonant dimer relaxation in cold atoms with a large scattering length. Phys. Rev. A, 75:052710, May 2007.

[113] S Thompson, E Hodby, and C. Wieman. Spontaneous dissociation of ^{85}Rb feshbach molecules. Phys. Rev. Lett., 94:020401, Feb 2005.

[114] K. Helfrich and H. Hammer. On the Efimov effect in higher partial waves. Journal of Physics B: Atomic, Molecular and Optical Physics, 44, Jul 2011.

[115] Eric Braaten and H.-W. Hammer. Efimov physics in cold atoms. Annals of Physics, 322(1):120 – 163, 2007. January Special Issue 2007.

[116] Tino Weber, Jens Herbig, Michael Mark, Hanns-Christoph Nägerl, and Rudolf Grimm. Three-body recombination at large scattering lengths in an ultracold atomic gas. Phys. Rev. Lett., 91:123201, Sep 2003.

[117] Chris H. Greene, B.D. Esry, and H. Suno. A revised formula for 3-body recombination that cannot exceed the unitarity limit. Nuclear Physics A, 737:119 – 124, 2004.

[118] Sanjukta Roy, Manuele Landini, Andreas Trenkwalder, Giulia Semeghini, Giacomo Spagnolli, Andrea Simoni, Marco Fattori, Massimo Inguscio, and Giovanni Modugno. Test of the universality of the three-body Efimov parameter at narrow Feshbach resonances. Phys. Rev. Lett., 111(5):053202, 2013.

[119] Noam Gross, Zav Shotan, Servaas Kokkelmans, and Lev Khaykovich. Observation of universality in ultracold ^{7}Li three-body recombination. Phys. Rev. Lett., 103:163202, Oct 2009.

[120] R. J. Wild, P. Makotyn, J. M. Pino, E. A. Cornell, and D. S. Jin. Measurements of Tan's contact in an atomic Bose-Einstein condensate. Phys. Rev. Lett., 108:145305, Apr 2012.

[121] L. J. Wacker, N. B. Jørgensen, K. T. Skalmstang, M. G. Skou, A. G. Volosniev, and J. J. Arlt. Temperature dependence of an Efimov resonance in ^{39}K. Phys. Rev. A, 98:052706, Nov 2018.

[122] G. Barontini, C. Weber, F. Rabatti, J. Catani, G. Thalhammer, M. Inguscio, and F. Minardi. Observation of heteronuclear atomic Efimov resonances. Phys. Rev. Lett., 103:043201, Jul 2009.

[123] Jacob Johansen, BJ DeSalvo, Krutik Patel, and Cheng Chin. Testing universality of Efimov physics across broad and narrow Feshbach resonances. Nature Physics, 13(8):731, 2017.

[124] Pascal Naidon, Shimpei Endo, and Masahito Ueda. Microscopic origin and universality classes of the Efimov three-body parameter. Phys. Rev. Lett., 112:105301, Mar 2014.

[125] P. Giannakeas and Chris Greene. Van der Waals universality in homonuclear atom-dimer elastic collisions. Few-Body Systems, 58, Dec 2016.

[126] Mark D. Lee, Thorsten Köhler, and Paul S. Julienne. Excited Thomas-Efimov levels in ultracold gases. Phys. Rev. A, 76:012720, Jul 2007.

[127] Alexander O. Gogolin, Christophe Mora, and Reinhold Egger. Analytical solution of the bosonic three-body problem. Phys. Rev. Lett., 100:140404, Apr 2008.

Appendix A

Algorithms: Absorption Imaging Simulation

A.1 Absorption Imaging Simulation

```
%% constants
h = 6.6260755e-34; hbar = h/(2*pi);
c = 299792458; amu = 1.6605402e-27;
um = 1e-6; nm = 1e-9; MHz = 1e6; us = 1e-6;
Gamma = (2*pi)*6.035*MHz; lambda = 766.701*nm; %D2 line
m39 = 39*amu; sigma0 = 3*lambda^2/(2*pi);

%% experiment parameters
% intensities are in unit of Isat, Isat is in unit of count
% delta is in unit of Gamma
I0_list = logspace( log10(1e-2),log10(3),15 );
rho_pk = 2.3e17; size = 10*um; pulse = 40*us;

%% stationary atom model
kr = 2*pi/lambda; vr = hbar*kr/m39;
N_photons = Gamma/(2*kr*vr); %=173 to shift by half a linewidth
dz = size/1e3; dt = pulse/1e3;
t_step = round(pulse/dt);
```

```
rho = rho_pk* exp( - [-size*5:dz:size*5].^2 / (2*size^2) );
n_step = length(rho);
Int = zeros(n_step, t_step); delta = zeros(n_step, t_step);
OD_simu1_list = [];

for i = 1:length(I0_list)
I0 = I0_list(i); Hf = 0;
Int(1,:) = I0; delta(:,1) = 0;
for t = 1:t_step
for n = 1:n_step
A = sigma0*rho(n)*dz;
B = kr*vr*dt/(2*sigma0*rho(n)*dz);
Int(n+1, t) = Int(n, t) - A* Int(n, t)./( 1 + 4*delta(n, t).^2 + Int(n, t) );
delta(n, t+1) = delta(n, t) + B* ( Int(n, t) - Int(n+1, t) );
end
Hf = Hf + Int(n_step+1, t)*dt;
end
OD_simu1 = -log( abs(Hf-I0*dt) / abs(I0*(t_step-1)*dt) )
OD_simu1_list = [ OD_simu1_list OD_simu1 ];
end

%% moving atom model
i = 1; I0 = I0_list(i);

kr = 2*pi/lambda; vr = hbar*kr/m39;
dz = size/1e2;
rho = rho_pk* exp( - [-size*5:dz:size*5].^2 / (2*size^2) );
```

```
n_step = length(rho);

z_frt = []; z_mid = []; z_bck = [];

OD_simu2_list = [];


for k = 1:length(pulse_list)

pulse = pulse_list(k)*us;

dt = pulse/1e3;

t_step = round(pulse/dt);

Int = zeros(n_step, t_step); delta = zeros(n_step, t_step);

z = zeros(n_step, 1);

z_cumu = [-size*2:dz:size*8]';

Hf = 0; Int(1,:) = I0; delta(:,1) = 0;

for t = 1:t_step

for n = 1:n_step

A = sigma0*rho(n)*dz;

B = kr*vr*dt/(2*A);

Int(n+1, t) = Int(n, t) - A* Int(n, t)./( 1 + 4*delta(n, t).^2 + Int(n, t) );

delta(n, t+1) = delta(n, t) + B* ( Int(n, t) - Int(n+1, t) );

z(n) = dt*Gamma* delta(n, t+1)/kr/2;

end

z_cumu = z_cumu + z;

[z_cumu, z_order] = sort(z_cumu); rho = rho(z_order);

Hf = Hf + Int(n_step+1, t)*dt;

end

OD_simu2 = -log( (Hf-I0*dt) / (I0*(t_step-1)*dt) );

OD_simu2_list = [ OD_simu2_list OD_simu2 ];

z_frt = [z_frt z_cumu(ceil(end/5))];
```

```
z_mid = [z_mid z_cumu(ceil(end/2))];

z_bck = [z_bck z_cumu(ceil(end*4/5))];

end
```

A.2 OD Correction as Function of I/I_{sat}

```
%% experiment input parameters

% intensities are in unit of Isat, Isat is in unit of count

% delta is in unit of Gamma

I0_list = 0.1;

rho_pk = linspace( 2.3e17/32,2.3e17,50 );

size = 10*um; pulse = 40*us;


%% stationary atom model

kr = 2*pi/lambda; vr = hbar*kr/m39;

N_photons = Gamma/(2*kr*vr);

dz = size/1e3; dt = pulse/1e3;

t_step = round(pulse/dt);

OD_corr_list = []; OD_phys_list = [];


for j = 1:length(rho_pk)

rho = rho_pk(j)* exp( - [-size*5:dz:size*5].^2 / (2*size^2) );

n_step = length(rho);

Int = zeros(n_step, t_step); delta = zeros(n_step, t_step);

I0 = I0_list; Hf = 0;

Int(1,:) = I0; delta(:,1) = 0;

for t = 1:t_step

for n = 1:n_step
```

```
A = sigma0*rho(n)*dz;

B = kr*vr*dt/(2*sigma0*rho(n)*dz);

Int(n+1, t) = Int(n, t) - A* Int(n, t)./( 1 + 4*delta(n, t).^2 + Int(n, t) );

delta(n, t+1) = delta(n, t) + B* ( Int(n, t) - Int(n+1, t) );

end

Hf = Hf + Int(n_step+1, t)*dt;

end

OD_simu1 = -log( (Hf-I0*dt) / (I0*(t_step-1)*dt) )

OD_phys = sigma0*sum(rho(:))*dz;

OD_correction = OD_simu1./OD_phys;

OD_corr_list = [OD_corr_list OD_correction];

OD_phys_list = [OD_phys_list OD_phys];

end
```

A.3 Fit Function for I_{sat}

```
x0 = [ 0.9 1237*2 ]; %initial guesses

pulse = 200;

%% method I

% modified Beer's law

[x1,resnorm,residual,exitflag,output,Lmda,Jmat] = ...

lsqcurvefit(@(x1,Int_list) OD_analytic(x1,Int_list), x0, Int_list, OD_list);

r21 = 1 - resnorm/sum((OD_list-mean(OD_list)).^2);

ci1 = nlparci(x1,residual,'jacobian',Jmat); %confidence interval

fit_err1 = abs(ci1(:,2) - ci1(:,1))/1.96/2;


function OD_meas = OD_analytic(x, Int_list)

%x(1) = OD_phys; x(2) = Isat
```

```
OD_meas = x(1) - Int_list/x(2) + lambertw( exp(Int_list/x(2) - x(1)) ...
.*Int_list/x(2));
end


%% method II
% correct for recoil induced detuning
[x2,resnorm,residual,exitflag,output] = ...
lsqcurvefit(@(x2,Int_list) OD_simu1(x2,Int_list,pulse), x0, Int_list, OD_list);
r22 = 1 - resnorm/sum((OD_list-mean(OD_list)).^2);
ci2 = nlparci(x1,residual,'jacobian',Jmat); %confidence interval
fit_err2 = abs(ci2(:,2) - ci2(:,1))/1.96/2;
```

Appendix B

Algorithms: Analysis of Optical Aberrations

B.1 PSF and MTF for an Ideal Pupil

```
%% experiment parameter

diameter0 = 26.15e-3; radius0 = diameter0/2;

f1 = 31.03e-3; f2 = 1500e-3;

mag = f2/f1; px_img = 16e-6; px_obj = px_img/mag;

NA = 0.384; lambda = 767e-9; Abbe_f = 2*NA/lambda;


%% put the pupil on a grid

dim = 5e3; pupil = zeros(dim,dim);

[d1,d2] = size(pupil);

x = -(d1-1)/2:(d1-1)/2; y = -(d2-1)/2:(d2-1)/2;

[Y,X] = meshgrid(y,x);

r = round(sqrt(Y.^2+X.^2));

theta = atan2(Y,X);

scal = 1e2; radius = dim/scal; pupil(r<=radius) = 1;


%% get the units right

pupil_unit = radius0/radius;

PSF_unit = (2*pi/dim)*radius/(2*pi*NA/lambda);
```

```
MTF_unit = (2*pi/dim)/PSF_unit;


%% PSF and MTF for ideal pupil
PSF = ifftshift(fft2(fftshift(pupil))); PSF = abs(PSF);
PSF = PSF.^2/max(max(PSF.^2));
% modulus squared for fluorescence
PSF = ifftshift(fft2(fftshift(pupil))); PSF = real(PSF);
PSF = PSF/max(max(PSF));
% real part for absorption
MTF = ifftshift(fft2(fftshift(PSF))); MTF = MTF/max(max(MTF));
```

B.2 Determination of Zernike Polynomial Coefficients

```
%% fitting parameters
pk = 0.9575; xc = 0.96; yc = 1.18; NA = 0.384; offset = 0.024;
S0 = -0.0978; alpha1 = -0.0065; alpha2 = 0.0008; beta = 0.0027;
delta1 = 0.0053; delta2 = 0.0136; epsilon1 = -0.0021; epsilon2 = -0.0008;
% these initial guesses are also the fitting results
x0 = [ pk, xc, yc, NA, offset, S0, alpha1, alpha2, beta, delta1, delta2, ...
epsilon1, epsilon2 ]; % initial guess parameters
x0fix = [ 0, 1, 1, 1, 0, 0, 0, 0, 0, 0, 0, 0, 0 ];


%% cost function
[x_free,resnorm,residual,exitflag,OptmInfo,Lmda,Jmat] = ...
lsqnonlin(@(x) abs( PSFZernike(interlace(x0,x,x0fix),xdata) - OD_trimmed ),...
x0(~x0fix),lb,ub);
x = interlace(x0, x_free, x0fix);
```

```
%% fitting function
function F = PSFZernike(x, xdata)

pupil2 = pupil.*...
exp( 2*pi*1i* ( x(6)*sqrt(5)*( 6*(r/radius).^4 -6*(r/radius).^2 + 1 ) ...
% spherical
+ x(7)*sqrt(6)*(r/radius).^2.*cos(2*theta) + x(8)*sqrt(6)*(r/radius).^2...
.*sin(2*theta) ...
% astigmatism
+ x(9)*sqrt(3)*( 2*(r/radius).^2 - 1 ) ... % defocus
+ gamma1*2*(r/radius).*sin(theta) + gamma2*2*(r/radius).*cos(theta) ... % tilts
+ x(10)*sqrt(8)*(3*(r/radius).^3 - 2*(r/radius)).*sin(theta) ...
+ x(11)*sqrt(8)*(3*(r/radius).^3 - 2*(r/radius)).*cos(theta) ...
% coma
+ x(12)*sqrt(8)*(r/radius).^3.*sin(3*theta) ...
+ x(13)*sqrt(8)*(r/radius).^3.*cos(3*theta) ));
% trefoil

PSF2 = ifftshift(fft2(fftshift(pupil2))); PSF2 = abs(PSF2);
PSF2 = x(1)*PSF2.^2/max(max(PSF2.^2)) + x(5);

F = interp2( Y1, X1, PSF2, ( xdata(:,:,1) + x(2) )*px/PSF_unit, ...
( xdata(:,:,2) + x(3) )*px/PSF_unit, 'spline' ); % interpolation

end

%% auxiliary function
```

```
function a = interlace(a, x, fix)

a(~fix) = x;

end
```

Appendix C

Algorithms: Finite-Temperature Effects in Atom-Dimer Relaxation

C.1 Parametrization of Atom-Dimer Scattering Amplitude

```
%% Definitions
nK = 1e-9; cm = 0.01; s = 1; ms = 0.001;


amu = 1.660539040*10^-27; %NIST
m = 38.9637064864*amu; %NIST
h = 6.626070040*10^-34; %NIST
a0 = 0.52917721067*10^-10; %NIST
kB = 1.38064852*10^-23; %NIST
hbar = h/(2*pi); kHz = 1e3;
s0 = 1.00624;


a = a1*a0; a_star = a_star1*a0;
kd = 2./(sqrt(3)*a);


%% AD scattering amplitude f_AD(k,theta)
c1 = @(a,k) -0.22 + 0.39*k.^2.*a.^2 - 0.17*k.^4.*a.^4;
c2 = @(a,k) 0.32 + 0.82*k.^2.*a.^2 - 0.14*k.^4.*a.^4;
phi = @(a,k) 2.64 - 0.83*k.^2.*a.^2 + 0.23*k.^4.*a.^4;
```

```
f_AD_para = @(a,k,a_star,eta) ...
c1(a,k) + c2(a,k).* cot( s0*( log(0.19*a) - log(a_star) ) + 1i*eta + phi(a,k) );
f_AD = @(a,k,a_star,eta) ...
( f_AD_para(a,k,a_star,eta) ./a - 1i.*k ).^(-1); %eqn(5)

sigma_ela = @(a,k,a_star,eta) 4*pi*abs( f_AD(a,k,a_star,eta) ).^2; %eqn(2)
sigma_tot = @(a,k,a_star,eta) 4*pi*imag( f_AD(a,k,a_star,eta) )./k; %eqn(3)
g = @(a,k,a_star,eta) ..
3*hbar.*k/(2*m) .*( sigma_tot(a,k,a_star,eta) - sigma_ela(a,k,a_star,eta) );
%eqn(11)

k_rel_integrand = @(a,k,a_star,eta,T) ..
k.^2 .* exp( - 3*hbar^2*k.^2 / (4*m*kB*T) ) .* g(a,k,a_star,eta); %eqn(13)
prefactor = @(ampl,T) ..
ampl* 4/sqrt(pi) *hbar^3 ./ (m*kB*T).^(3/2); %use Boltzmann distribution

%% Integral
beta_out = [];
for index = 1:length(a1)
k_rel = logspace(log10(kd(index)/1e6),log10(kd(index)),1e3);
beta_out_scal(index) = ...
prefactor(ampl,T) .* trapz(k_rel, k_rel_integrand(a(index),k_rel,a_star,eta,T));
beta_out = [beta_out beta_out_scal(index)];
end
```

C.2 Atom-Dimer Chemical Equilibrium: a Toy Model

```
%% Ebind function

rvdW = 64.49; %in unit of a0

abar = 0.955978*rvdW;

Eb = @(as) hbar^2 ./( ma*( (as - abar)*a0 ).^2 );

lambda = @(temp) h* ( 2*pi*ma*kB *temp ).^(-1/2);


%% AD chemical equilibrium (Saha-Boltzmann type, in a box)

PSD = @(na, temp) na.*lambda(temp).^3;

nd = @(na, temp, as) 2^(3/2)* na.^2 .*lambda(temp).^3 .*exp( Eb(as)./(kB*temp) );


%% number and energy conservation

alist = logspace( log10(5e2), log10(8e3), 2 ); sol0 = [];

%initial guesses

for j = 1:length(alist)

syms naf1

solg0 = vpasolve( nai1 == 2*nd( naf1, Ti1, alist(j)) + naf1 );

j = j+1;

solg1(j) = solg0(2);

end

solg = double(solg1);


%solve coupled equations

for i = 1:length(alist)

syms naf1 Tf1

sol0 = vpasolve( [ nai1 == 2*nd( naf1, Tf1, alist(i)) + naf1, ...
```

```
nai1* (3/2)*kB*Ti1 == ...
nd( naf1, Tf1, alist(i) )*( (3/2)*kB*Tf1-Eb(alist(i)) )+naf1*(3/2)*kB*Tf1 ],...
[naf1, Tf1], [ solg(i), Ti1 ]);

sol1(1,i) = sol0.Tf1;
sol1(2,i) = sol0.naf1;
sol1(3,i) = nd( sol0.naf1, sol0.Tf1, alist(i) );
i = i+1;
end

sol = double(sol1);
templist = sol(1,:);
nalist = sol(2,:);
ndlist = sol(3,:);
```

C.3 Fit Function for Dimer-Dimer Collision Rate Constant

```
% all N's are density
% dNa/dt/Na =
% - beta*Nd          % A-D inelastic collisions to form deep dimers
% - 2*delta'*(Na)(Nd)  % ignore this for early decay time
% + 2*delta*(Nd)^2/Na;  % D-D collisional dissociation, assume K2+K2=4K

% dNd/dt/Nd =
% - alpha               % 1-body decay due to spin relaxation
% - gamma*Nd       % D-D inelastic collisions to form deep dimers
% - beta*Na          % ignore this for early decay time
```

```
% - delta*Nd       % D-D collisional dissociation, assume K2+K2=4K
% + delta'*(Na)^2;     % ignore this for early decay time


function y = AtomNumbODEmulti(A,tspan,B)
% A(1) = beta, A(2) = delta;
y0 = A(3);
[t,y] = ode45(@DifEq, tspan, y0);
function dy = DifEq(t, y)
ydot = zeros(1,1);
ydot = - A(1)*y.*double_expo(B,t) + 2*A(2)*double_expo(B,t).^2;
dy = ydot;
end
end


function y = DimerNumbODEmulti(B,tspan)
% B(1) = alpha, B(2) = gamma, B(3) = delta;
y0 = B(4);
[t,y] = ode45(@DifEq, tspan, y0);
function dy = DifEq(t, y)
ydot = zeros(1,1);
ydot = - y/B(1) - B(2)*y.^2 - B(3)*y.^2;
dy = ydot;
end
end
```

Appendix D

Algorithms: Finite-Temperature Effects in Three-Body Recombination

D.1 L_3 Fitting Protocol I

```
%% sorting and statistics

%sort by timing

[t_list0, t_sort0] = sort(t_list0); %get sorted indices

N_list0 = N_list0(t_sort0); %sort N

T_list0 = T_list0(t_sort0); %sort T

%do stats for each wait time

[t_list, ix, iy] = unique(t_list0); %get unique timings (non-repetitive)

N_list1 = [t_list, accumarray(iy, N_list0, [], @mean)]; %N mean

N_std1 = [t_list, accumarray(iy, N_list0, [], @std)]; %N std

T_list1 = [t_list, accumarray(iy, T_list0, [], @mean)]; %T mean

T_std1 = [t_list, accumarray(iy, T_list0, [], @std)]; %T std

%final lists generated from stats

N_list = N_list1(:,2); %N mean list

N_std = N_std1(:,2);

T_list = T_list1(:,2); %T mean list, T = ( Tz + 2*Tx )/3

T_std = T_std1(:,2);

%regulate

max_bound_inds = t_list(:) < t_max;
```

```
t_list = t_list(max_bound_inds);

N_list = N_list(max_bound_inds);

T_list = T_list(max_bound_inds);

min_bound_inds = t_list(:) > t_min;

t_list = t_list(min_bound_inds);

N_list = N_list(min_bound_inds);

T_list = T_list(min_bound_inds);


%% temperature fit function

x0 = [ 0.15 0.04 -1 ]; %initial fit parameter guesses

[x,Rsdnrm,Rsd,ExFlg,OptmInfo,Lmda,Jmat] = ...

lsqnonlin(@(x)(polyx(x,t_list)-T_list),x0);


function Temp = polyx(x, t_list)

% 2nd-order/quadratic polynomial: (poly fit works better for short t hold range)

% Temp = x(1) + x(2)*t_list + x(3)*t_list.^2;

% or use exponential: (expo fit works better for long t hold range)

Temp = x(1) + x(2).*exp(t_list./x(3));

end


%% number fit function

[Nmax, Imax] = max(N_list); %get maximum N index

N0_guess = N_list(Imax); %guess initial N = maximum N

B0 = [ 0.0117 (2*K2)*cm^3/(T2V0*nK^(3/2)) ...

(0.1*1.5e-26*cm^6/(T2V*nK^3)) N0_guess ]; %initial guess values

fix = [ 1 1 0 0 ]; %fix fitting parameters

[B_free,Rsdnrm,Rsd,ExFlg,OptmInfo,Lmda,Jmat] = lsqcurvefit(@(B,t_list) ...
```

```
NumbODE3(interlace(B0,B,fix),t_list,T_para),B0(~fix),t_list,N_list,[],[]);
B = interlace(B0, B_free, fix); %defined in Appx A.2
r2 = 1 - Rsdnrm/sum((N_list-mean(N_list)).^2); %r-squared
ci = nlparci(B_free,Rsd,'jacobian',Jmat); %confidence interval of the fitting
fit_err_free = abs(ci(:,2) - ci(:,1))/1.96/2;
fit_err = interlace([0 0 0 0], fit_err_free, fix);


function y = NumbODE3(B,tspan,para)
% dN/dt = -K3 <n^2> N - K2 <n> N - alpha N
% <n^2> = Int(n^3 dxdydz); <n^3> = Int(n^4 dxdydz)
%dN/dt = - B(1)*N - B(3)*N^3/T^3 - B(2)*N^2/T^(3/2);
y0 = B(4); uK2nK = 1e3;
[t,y] = ode45(@DifEq, tspan, y0);
function dy = DifEq(t, y)
ydot = zeros(1,1);
ydot = - B(1)*y - B(3)*y^3./((polyx(para,t)*uK2nK).^3) - B(2)*y^2./ ...
((polyx(para,t)*uK2nK).^(3/2));
dy = ydot;
end
end


%% get the statistics
% time-averaged density and temperature and collision rate
t_grid = linspace( t_list(1), t_list(end), 1e3 );
dt = ( t_list(end) - t_list(1) )/1e3;
N_grid = NumbODE3(B,t_grid,T_para); N_grid = N_grid';
Temp_grid = polyx(T_para, t_grid);
```

```
T_sum = sum( Temp_grid *dt ); %average temperature from summation
T_std = std( T_list*1e3 );
T_init = polyx(T_para, 0) *1e3; % extrapolate to 0
T_final = T_list(end) *1e3;
T_avg = T_sum /(t_list(end) - t_list(1)) *1e3; %average temperature in nK
T_output = [ T_init, T_avg, T_std ];


den2_sum = sum( (N_grid.^2 ./ (Temp_grid*uK).^3 )*dt );
den2_avg = den2_sum / ( t_list(end) - t_list(1) ) / T2V * (cm^6); % <n^2>
den_pk_avg = sqrt( den2_avg * sqrt(27) ); %peak density
den_avg_avg = den_pk_avg / (2*sqrt(2)); %average density <n>
n_avg_init = ...
(N_list(1).*w.^3.*(m39./(2.*pi.*kB.*T_list(1).*uK)).^(3/2))*cm^3/(2^(3/2));
den_combo = [ den_pk_avg, den_avg_avg, den2_avg ];


n_avg_list = ...
(N_grid.*w.^3.*(m39./(2.*pi.*kB.*Temp_grid.*uK)).^(3/2))*cm^3/(2^(3/2));
col_rate_list = ...
n_avg_list./cm^3.*8.*pi.*a.^2.*sqrt((16.*kB.*Temp_grid.*uK)./(pi.*m39));
col_rate_init = ...
n_avg_init./cm^3.*8.*pi.*a.^2.*sqrt((16.*kB.*T_list(1).*uK)./(pi.*m39));
col_rate_avg = sum(col_rate_list *dt) /(t_list(end) - t_list(1));
col_rate_combo = [col_rate_init, col_rate_avg ];
```

D.2 L_3 Fitting Protocol II (Simultaneous Fit)

```
%% number fit function
```

```
%two conditions are put in two cells
[Nmax1, Imax1] = max(N_list{1}); [Nmax2, Imax2] = max(N_list{2});
N0_guess1 = N_list{1}(Imax1); N0_guess2 = N_list{2}(Imax2);
B0 = [ 0.5*(0.0117+0.0159) (2*K2)*cm^3/(T2V0*nK^(3/2)) ...
(0.1*1.5e-26*cm^6/(T2V*nK^3)) N0_guess1 N0_guess2 ]; %initial guess values
fix = [ 1 0 0 0 0 ]; %fix fitting parameters
fun_cell=@(B,t_list) [NumbODE3_simu1(interlace(B0,B,fix),t_list{1},T_para{1});...
NumbODE3_simu2(interlace(B0,B,fix),t_list{2},T_para{2}) ];
NN = vertcat( N_list{:} );
[B_free,Rsdnrm,Rsd,ExFlg,OptmInfo,Lmda,Jmat] = ...
lsqcurvefit(fun_cell,B0(~fix),t_list,NN,[(2*K2)*cm^3/(T2V0*nK^(3/2)) 0 0 0],[]);
B = interlace(B0, B_free, fix); %defined in Appx A.2
```

D.3 S-Matrix Formalism

```
%% fitting program
B0 = [ 900, 0.20, 230*nK, 1 ]; % guess parameters, a+, eta, T, ampl
fix = [ 0, 1, 1, 0 ];
options=optimset('TolFun',1e-60,'TolX',1e-50,'MaxFunEvals',2000,'MaxIter',2000);
lb = [ 800, 0 ]; ub = [ 1100, 2 ];
[B_free,Rsdnrm,Rsd,ExFlg,OptmInfo,Lmda,Jmat] = ...
lsqnonlin(@(B) abs((1./L3_std)...
.*(L3_function_pos_a_for_fit(interlace(B0,B,fix),a_list)
-L3_list)),B0(~fix),lb,ub,options); %cost function
B = interlace(B0, B_free, fix);
r2 = 1 - Rsdnrm/sum((L3_list-mean(L3_list)).^2); %r-squared
ci = nlparci(B_free,Rsd,'jacobian',Jmat); %confidence interval of the fitting
fit_err_free = abs(ci(:,2) - ci(:,1))/1.96/2;
```

```
fit_err = interlace([0 0 0 0], fit_err_free, fix); %defined in Appx A.2

%% fitting function
function [L3out_finiteT_all] = L3_function_pos_a_for_fit_final(B, a1)
a_plus = B(1); eta = B(2); T = B(3); ampl = B(4);

complex_s11 = s11_abs .* exp( 1i*s11_arg );
complex_s12 = s12_abs .* exp( 1i*s12_arg );
complex_s22 = s22_abs .* exp( 1i*s22_arg );
L3s_T0 = L3_function_pos_a_zero_T_shallow(a_plus, eta, a1, ampl);
L3s_out2 = L3_function_pos_a_shallow(a_plus, eta, a1, T, ampl, ka, ...
complex_s11, complex_s12, complex_s22);
L3d_T0 = L3_function_pos_a_zero_T_deep(a_plus, eta, a1, ampl);
L3d_out2 = L3_function_pos_a_deep(a_plus, eta, a1, T, ampl, ka, ...
complex_s11, complex_s12, complex_s22);

ka_cut = 0.4; %about 30 points removed
L3s_out2 = L3s_out2( ka(:)>=ka_cut, : ); L3d_out2 = L3d_out2( ka(:)>=ka_cut,: );
ka = ka( ka(:)>=ka_cut );
%concatenate
ka = [0; ka];
L3s_out2 = [L3s_T0; L3s_out2]; L3d_out2 = [L3d_T0; L3d_out2];

%interpolate
ka_interp = logspace(log10(1e-2),log10(1e1),1e4)';
L3s_interp2 = interp2(a1, ka, L3s_out2, a1, ka_interp, 'spline');
L3d_interp2 = interp2(a1, ka, L3d_out2, a1, ka_interp, 'spline');
```

```
%integrate
x = ka_interp; a = a1*a0;
expo = exp( - hbar^2.*(x./a).^2 /m/ (kB*T) );

L3s_integrand = 2*hbar^7/m^4 .* (x.^5 ./ a.^2) .* expo .* ( L3s_interp2 );
L3d_integrand = 2*hbar^7/m^4 .* (x.^5 ./ a.^2) .* expo .* ( L3d_interp2 );
L3sout = ampl /6/ ( 2*(kB*T)^3 ) .* trapz(x,L3s_integrand);
L3dout = ampl /6/ ( 2*(kB*T)^3 ) .* trapz(x,L3d_integrand);

% J>0 terms
[ka_out, KJ_out] = L3_function_pos_a_nonzero_J;
expoJ1 = exp( - hbar^2.*(ka_out(:,1)./a).^2 /m/ (kB*T) );
L3J_integrand1 = 2*hbar^7/m^4 .* (ka_out(:,1).^5 ./ a.^2) .* expoJ1 .*KJ_out(:,1);
L3Jout1 = ampl /6/ ( 2*(kB*T)^3 ) .* trapz(ka_out(:,1),L3J_integrand1);
expoJ2 = exp( - hbar^2.*(ka_out(:,2)./a).^2 /m/ (kB*T) );
L3J_integrand2 = 2*hbar^7/m^4 .* (ka_out(:,2).^5 ./ a.^2) .* expoJ2 .*KJ_out(:,2);
L3Jout2 = ampl /6/ ( 2*(kB*T)^3 ) .* trapz(ka_out(:,2),L3J_integrand2);

expoJ3 = exp( - hbar^2.*(ka_out(:,3)./a).^2 /m/ (kB*T) );
L3J_integrand3 = 2*hbar^7/m^4 .* (ka_out(:,3).^5 ./ a.^2) .* expoJ3 .*KJ_out(:,3);
L3Jout3 = ampl /6/ ( 2*(kB*T)^3 ) .* trapz(ka_out(:,3),L3J_integrand3);
expoJ4 = exp( - hbar^2.*(ka_out(:,4)./a).^2 /m/ (kB*T) );
L3J_integrand4 = 2*hbar^7/m^4 .* (ka_out(:,4).^5 ./ a.^2) .* expoJ4 .*KJ_out(:,4);
L3Jout4 = ampl /6/ ( 2*(kB*T)^3 ) .* trapz(ka_out(:,4),L3J_integrand4);

expoJ5 = exp( - hbar^2.*(ka_out(:,5)./a).^2 /m/ (kB*T) );
L3J_integrand5 = 2*hbar^7/m^4 .* (ka_out(:,5).^5 ./ a.^2) .* expoJ5 .*KJ_out(:,5);
```

```
L3Jout5 = ampl /6/ ( 2*(kB*T)^3 ) .* trapz(ka_out(:,5),L3J_integrand5);

expoJ6 = exp( - hbar^2.*(ka_out(:,6)./a).^2 /m/ (kB*T) );

L3J_integrand6 = 2*hbar^7/m^4 .* (ka_out(:,6).^5 ./ a.^2) .* expoJ6 .*KJ_out(:,6);

L3Jout6 = ampl /6/ ( 2*(kB*T)^3 ) .* trapz(ka_out(:,6),L3J_integrand6);


L3out_finiteT = L3sout + L3dout +...

(L3Jout1 + L3Jout2 + L3Jout3 + L3Jout4 + L3Jout5 + L3Jout6)*0;


[Lmax,index] = max(L3out_finiteT);

%interpolate to unitary value where s_ij lose accuracy

if index < length(a1)

L3out_finiteT_truc = L3out_finiteT(1:index);

L3out_finiteT_cat = [L3out_finiteT_truc, L3max];

a_truc = a1(1:index);

a_cat = [a_truc,a1(end)];

L3out_finiteT_all = interp1(a_cat,L3out_finiteT_cat,a1,'PCHIP');

else

L3out_finiteT_all = L3out_finiteT;

end


L3out_finiteT_all = 3*(cm^6/s)^(-1)*L3out_finiteT_all;

%3 is the number of atoms lost

end


%% sub-functions (zero-T)

function [ L3out ] = L3_function_pos_a_zero_T_shallow(a_plus, eta, a1, ampl)

L3_shallow = 768*pi^2*(4*pi-3*sqrt(3)) *( sin( theta ).^2 + sinh(eta).^2 ) ...
```

```
./ ( sinh( pi*s0 + eta )^2 + cos( theta ).^2 );
L3out = L3_shallow;
end

function [ L3out ] = L3_function_pos_a_zero_T_deep(a_plus, eta, a1, ampl)
L3_deep = (3/2)*128*pi^2*(4*pi-3*sqrt(3)) ./ sinh(pi*s0).^2 .* ...
sinh(2*pi*s0) .* sinh(2*eta) ./ ( sinh(pi*s0 + eta)^2 + cos( theta ).^2 );
L3out = L3_deep;
end

%% sub-functions (finite-T)
%eq3 of PRA 78,043605 (2008)
function [ L3out ] = L3_function_pos_a_shallow(a_plus, eta, a1, T, ampl, ka, ...
complex_s11, complex_s12, complex_s22)
x = ka; %change of variables. s11(ka) = s11(x)
L3_shallow = ...
1 - abs( complex_s22 + complex_s12.^2 .* exp( 2*1i*theta - 2*eta ) ...
./ ( 1 - complex_s11 .* exp( 2*1i*theta - 2*eta )) ).^2 - ( 1 - exp(-4*eta) ) ...
.* abs(complex_s12).^2 ./ abs( 1 - complex_s11 .* exp( 2*1i*theta - 2*eta ) ).^2;
L3out = 144*sqrt(3)*pi^2 ./ (x.^4) .*L3_shallow;
end

function [ L3out ] = L3_function_pos_a_deep(a_plus, eta, a1, T, ampl, ka, ...
complex_s11, complex_s12, complex_s22)
theta = s0*log(a1./a_plus);
%theta =  pi/2 + theta; %for fitting recombination maxima
x = ka;
```

```
L3_deep = ...
( 1 - exp(-4*eta) ) .* ( 1 - abs(complex_s11).^2 - abs(complex_s12).^2 ) ...
./ abs( 1 - complex_s11 .* exp( 2*1i*theta - 2*eta ) ).^2;
L3out = 144*sqrt(3)*pi^2 ./ (x.^4) .*L3_deep;
end
```

Appendix E

Data and Fits: Three-Body Recombination at Finite Temperatures

E.1 Extract $a_+^{(0)}$ from 460 nK Data

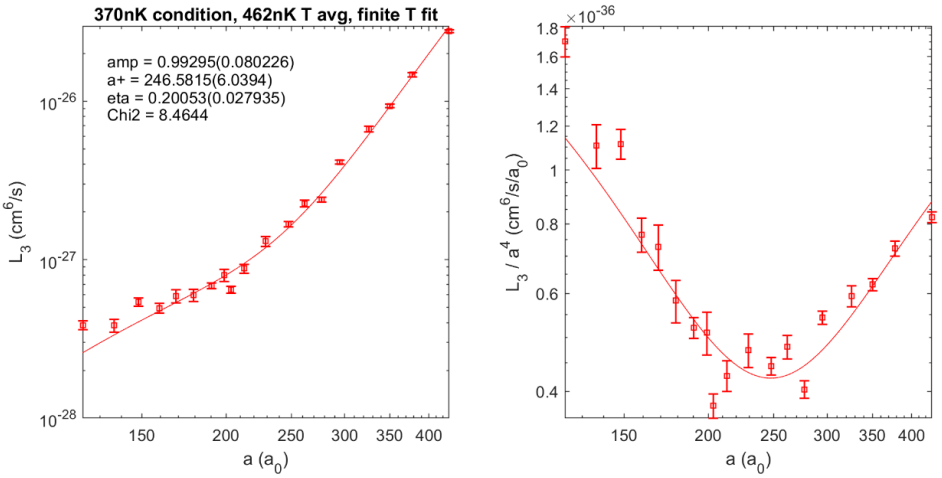

Figure E.1: Finite-temperature fit for recombination minimum, 460 nK condition, $J = 0$. The fitting results are consistent with zero-temperature fit within errors.

E.2 Extract $a_p^{(0)}$ from 410 nK and 230 nK Data

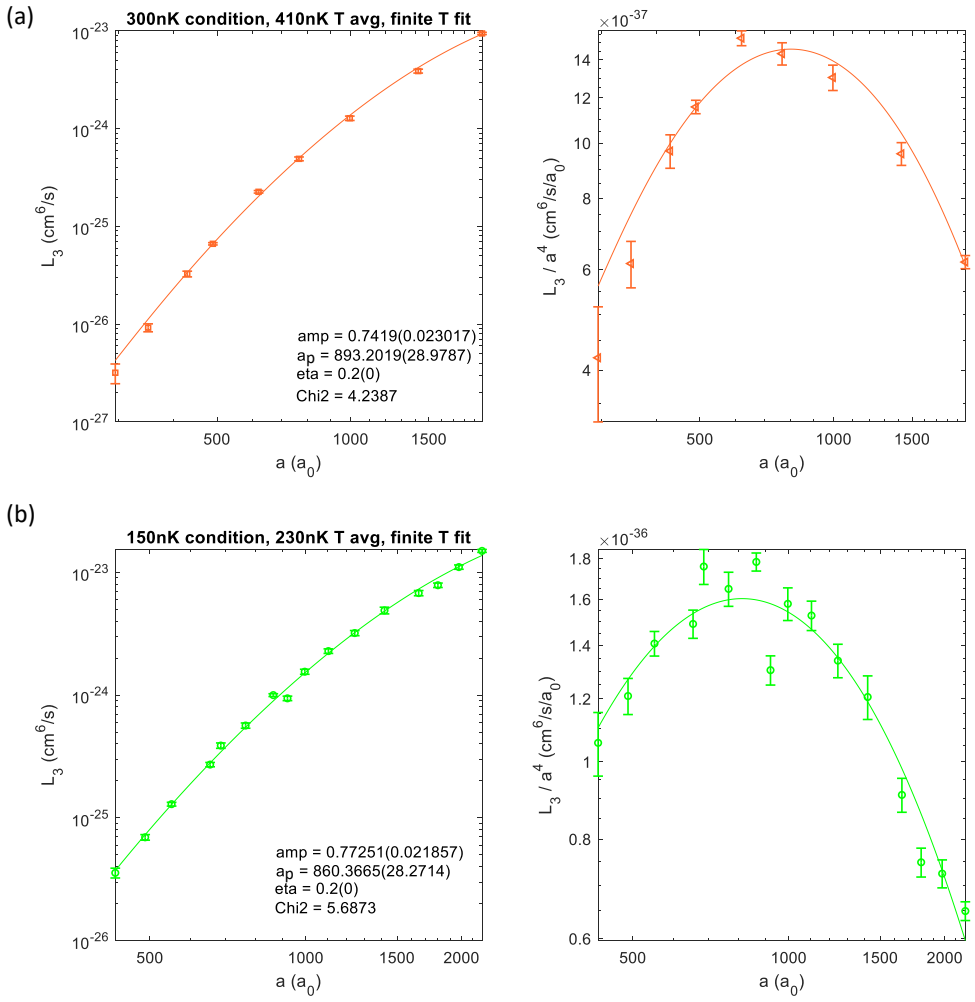

Figure E.2: Finite-temperature fit for recombination maximum, 410 nK and 230 nK conditions, $J = 0$. We fix η to be 0.2 in this fit.

E.3 Exploration of $a_+^{(1)}$

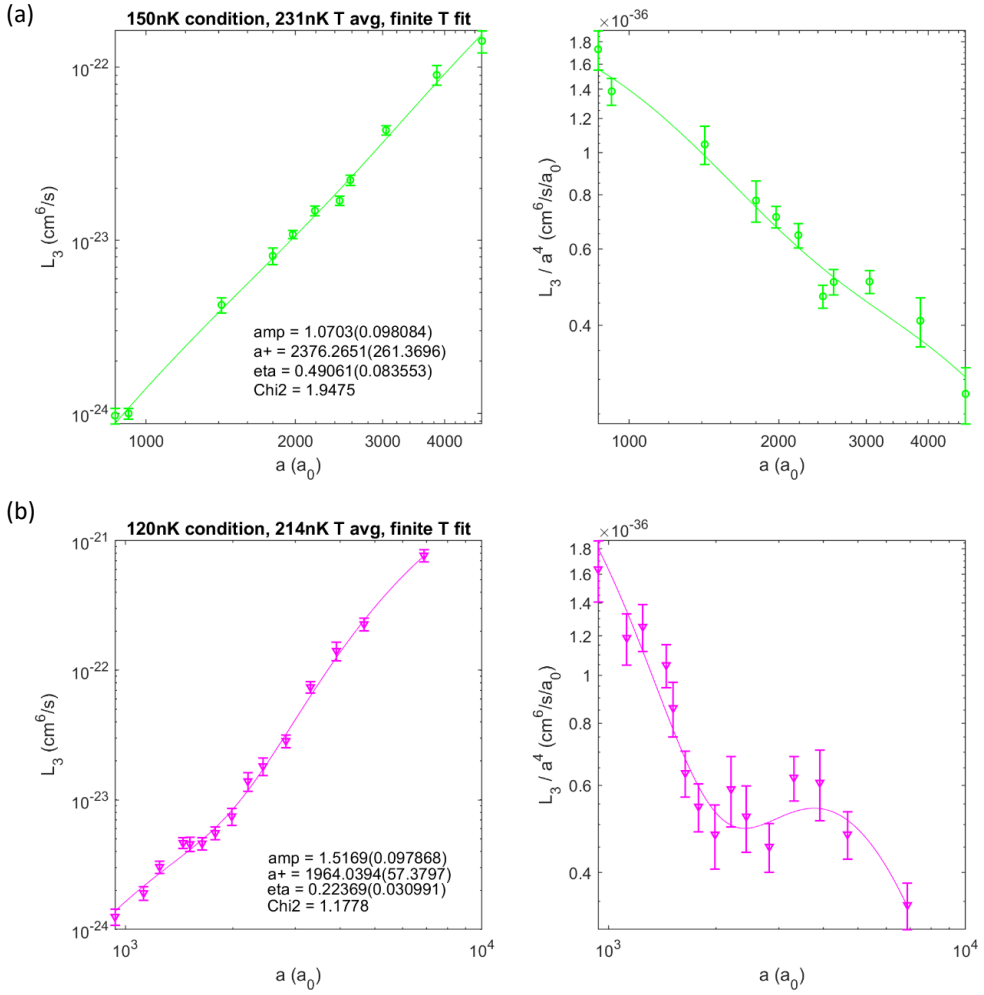

Figure E.3: Finite-temperature fit for recombination minimum, 230 nK and 210 nK condition, $J = 0$.

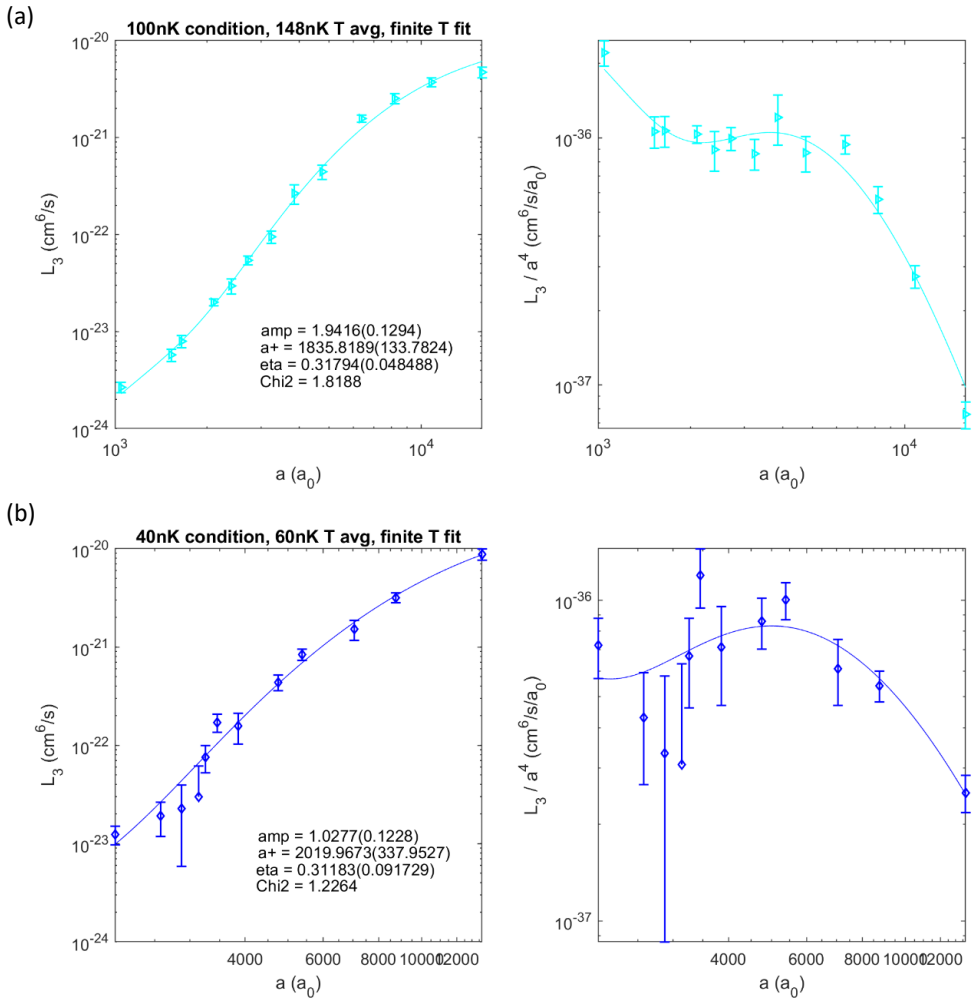

Figure E.4: Finite-temperature fit for recombination minimum, 150 nK and 60 nK condition, $J = 0$.